Theses and Dissertations

2016

Detection and Analysis of Molecular Interactions with Backscattering Interferometry

Gabrielle Lee Haddad-Weiser
Lehigh University

Follow this and additional works at: http://preserve.lehigh.edu/etd

Part of the Chemistry Commons

Detection and Analysis of Molecular Interactions with Backscattering Interferometry

by

Gabrielle Lee Haddad-Weiser

A Dissertation

Presented to the Graduate and Research Committee

of Lehigh University

in Candidacy for the Degree of

Doctor of Philosophy

in

Chemistry

Lehigh University

August 2, 2016

Approved and recommended for acceptance as a dissertation in partial fulfillment of the requirements for the degree of Doctor of Philosophy

Gabrielle Lee Haddad-Weiser
Detection and Analysis of Molecular Interactions with Backscattering Interferometry

August 2, 2016
—————————————————

Defense Date

—————————————————
Dissertation Director
Dr. Robert A. Flowers II

—————————————————

Approved Date

Committee Members:

—————————————————

Dr. K. Jebrell Glover

—————————————————

Dr. Damien Thevenin

—————————————————

Dr. Bryan Berger

—————————————————

extra fortune cookies during those late night writing sessions. And finally, thank you to my amazing and ever-supportive family and especially to my awesomely wonderful husband, Philip Weiser. Your constant support especially means the world to me, and I would not have been able to complete this dissertation without you by my side. Now it's your turn to write yours! Thank you for always being my rock, offering support, listening to me vent, and sneaking candy into my purse.

TABLE OF CONTENTS

List of Figures

List of Tables

List of Abbreviations

15C5	15-crown-5
18C6	18-crown-6
A	Adenine
ACh	Acetylcholine
AChE	Acetylcholinesterase
AChEI	acetylcholinesterase inhibitor
AD	Alzheimer's disease
ATCh	Acetylthiocholine
Aβ	Beta amyloid
BChE	Butyrylcholinesterase
bp	Base pair
BSI	Backscattering Interferometry
C	Cytosine
CaM	Calmodulin
CaN	Calcineurin
CCD	Charge-coupled device
CD	Circular dichroism
ChAT	Choline acetyltransferase
Cy3	Cyanine-3
DMSO	Dimethyl sulfoxide
DNA	Deoxyribonucleic acid
DNPTU	Dinitrophenyl thiourea
DNPU	Dinitrophenyl urea
DPTU	Diphenyl thiourea
DPU	Diphenyl urea
dsDNA	Double-stranded DNA
DTNB	Dithionitrobenzoic acid
FFT	Fast Fourier transform
FITC	Fluorescein isothiocyanate
FLIM	Fluorescence lifetime imaging microscopy
FRAP	Fluorescence recovery after photobleaching
FreeSRF	Free-solution response function
FRET	Fluorescence resonance energy transfer
G	Guanine
GPCR	G-protein coupled receptors
HBOC	Hereditary breast and ovarian cancer
ISE	Ion selective electrode

ITC	Isothermal titration calorimetry
LIGO	Laser Interferometer Gravitational-Wave Observatory
LOD	Limit of detection
M13	Myosin light chain kinase peptide
MB	Molecular beacon
MeCN	Acetonitrile
MeOH	Methanol
MEPTES	3-mercaptopropyltriethoxysilane
MIBD	Micro-interferometric backscatter detector
mRec	Myristoylated recoverin
NMR	Nuclear Magnetic Resonance
PAS	Peripheral anionic site
PBS	Phosphate-buffered saline
PCR	Polymerase chain reaction
PDB	Protein databank
R_{gyr}	Radius of gyration
RI	Refractive index
RIU	Refractive index units
RNA	Ribonucleic acid
RU	Resonance units
SAR	Structure-activity relationship
SASA	Solvent accessible surface area
SEM	Standard error of the mean
SNP	Single nucleotide polymorphism
SPR	Surface Plasmon Resonance
ssDNA	Single-stranded DNA
T	Thymine
Tfp	Trifluoperazine fluoride
TMAB	Tetramethylammonium benzoate
UV	Ultraviolet
Vm	Valinomycin
XMEA	X-linked myopathy with excessive autophagy

Abstract

Back-scattering Interferometry (BSI) is an analytical technique that measures changes in refractive index (RI) as two species interact in solution. A high-contrast interference fringe pattern is generated, and the fringes shift spatially as molecular interactions such as binding occur. Experiments can be performed label-free in free solution, eliminating the potential perturbations that can arise with surface immobilization or fluorescent labeling. The source of this signal change derives from intrinsic property changes as a new species, the complex, is formed in solution, particularly changes in conformation and solvation. Recently an expression for the source of this signal, the Free Solution Response Function (FreeSRF) was developed in an effort to more fully describe and quantify it.[1] A binding curve is generated from the data, from which dissociation constants can be determined for a measure of binding affinity. The work in this dissertation covers three different types of binding systems analyzed with BSI.

First, a series of known and novel inhibitors of acetylcholinesterase (AChE) were screened, the former to benchmark the technique and the latter to evaluate potential anti-Alzheimer's disease (AD) agents. By comparing K_D results from BSI to IC_{50} values obtained using Ellman's assay,[2] insight into the inhibition mechanism for each inhibitor could be obtained based on the Cheng-Prusoff relationship.[3] Specifically, BSI K_D values that were equal to Ellman IC_{50} indicated the inhibitor was acting via noncompetitive inhibition, while inhibitors with $K_D < IC_{50}$ acted as competitive or mixed inhibitors. These results make BSI an especially good technique for evaluating potential anti-AD agents that act as noncompetitive inhibitors and target the peripheral site of the enzyme,

where beta amyloids are known to aggregate and accelerate plaque formation.[4] Additionally, using a high-affinity inhibitor, BW284c51, we showed that BSI is capable of detecting less than 23,000 AChE molecules at the lowest limit, a level that matches or exceeds detection limits of other techniques.[5,6]

Next, we evaluated BSI's ability to distinguish between several 20-base pair DNA oligomers: a perfect complement and a sequence containing a SNP. The SNP-containing sequences had either a mismatch or a deleted base located in the middle of the sequence or five base pairs from the 3'-end. By comparing the BSI K_D values of each duplex and comparing those to melting transition temperatures obtained from hyperchromicity experiments, we confirmed our hypothesis that the complement duplex was significantly more stable than any of the duplexes containing a SNP, having a K_D ca. 18-130% lower than the SNP duplexes. Additionally, SNPs located in the middle of the sequence were more destabilizing than the same SNP located closer to the end of the sequence, and when comparing two different SNPs at the same location, the A/G mismatch was more destabilizing than the T deletion. The complement duplex also had at least a 35% larger signal compared to the SNP duplexes. SNP research is an important field for personalized medicine and disease diagnostics, and this work showed BSI could play a role in advancing those fields.

Lastly, BSI was used to detect selection ion recognition of 18-crown-6 and three ionophores to potassium. These small molecules in nonaqueous media were expected to produce a much smaller signal compared to the large biochemical systems typically studied with BSI due to a lack of major conformation and solvation changes as seen with protein binding or DNA hybridization. Experiments with ITC benchmarked the BSI

results. The goal was to quantify the smallest possible signal BSI could detect and evaluate the FreeSRF expression for nonaqueous, small molecule systems. Formation of potassium complexes with potassium ionophores I and II generated signals more than an order of magnitude smaller than complement DNA hybridization. Potassium ionophore I, also known as valinomycin, folds into a "tennis ball seam" conformation upon binding with potassium while potassium ionophore II forms a "closed clamshell" structure; these complexes generated a signal over 30% larger than that of the potassium-18C6 complex, which undergoes only a minor shift in conformation from a S_6 or C_i structure to D_{3d} upon complexation.[7,8] Conversely, Na^+ with 18C6 experiments generated no readable signal above the noise, highlighting BSI's ability to selectively detect ion recognition.

Interesting observations into the direction of the signal were also made, particularly with ionophore III, which features a dodecyl tail in the middle of the linker between the two 15C5 ends and caused the signal to reverse direction as potassium was added. Signal direction is thought to be related to hydrodynamic radius, which this hydrocarbon tail would significantly alter as the ionophore forms the "closed clamshell" complex. Other experiments show BSI has potential to examine the stoichiometry of binding systems, and decomplexation, rather than complexation, of the ionophore I-potassium complex in water.

BSI offers many advantages compared to other techniques, including its ability to run experiments label-free and in free solution, its small sample size (with a probe volume of just 7.52 nL), and high sensitivity even in small-molecule systems with very minor conformational changes. These experiments show it has potential for many uses, from diagnostics, drug screening, and metal ion detection. As research into the signal

3

origin and FreeSRF evaluation progress, it will continue to be a valuable refractive index

detector for various chemical fields.

References

1.   Bornhop, D. J., Kammer, M. N., Kussrow, A., Flowers, R. A. & Meiler, J. Origin and prediction of free-solution interaction studies performed label-free. *Proc. Natl. Acad. Sci. U. S. A.* **113,** E1595–604 (2016).

2.   Ellman, G. L. Tissue sulfhydryl groups. *Arch. Biochem. Biophys.* **82,** 70–77 (1959).

3.   Cheng, Y. & Prusoff, W. H. Relationship between the inhibition constant (KI) and the concentration of inhibitor which causes 50 per cent inhibition (I50) of an enzymatic reaction. *Biochem. Pharmacol.* **22,** 3099–3108 (1973).

4.   Inestrosa, N. C. *et al.* Acetylcholinesterase accelerates assembly of amyloid-β-peptides into Alzheimer's fibrils: Possible role of the peripheral site of the enzyme. *Neuron* **16,** 881–891 (1996).

5.   Peng, L. *et al.* A fluorescence 'turn-on' ensemble for acetylcholinesterase activity assay and inhibitor screening. *Org. Lett.* **11,** 4014–4017 (2009).

6.   Sabelle, S. *et al.* Design and synthesis of chemiluminescent probes for the detection of cholinesterase activity. *J. Am. Chem. Soc.* **124,** 4874–4880 (2002).

7.   Al-Jallal, N. A., Al-Kahtani, A. A. & El-Azhary, A. A. Conformational Study of the Structure of Free 18-Crown-6. *J. Phys. Chem. A* **109,** 3694–3703 (2005).

8.   Seiler, P., Dobler, M. & Dunitz, J. D. Potassium thiocyanate complex of 1,4,7,10,13,16-hexaoxacyclooctadecane. *Acta Crystallogr. Sect. B Struct. Crystallogr. Cryst. Chem.* **30,** 2744–2745 (1974).

Chapter 1: Introduction

1.1   Introduction and the study of molecular interactions

Chemical interactions are ubiquitous in life, and a wide variety of assays exist to study just a small portion of these reactions, interactions, and functions. Analytical techniques have allowed for significant discoveries and progress in biochemical, medicinal, and chemical fields and have grown increasingly sensitive and powerful over the past few decades. Both inter- and intramolecular forces, including hydrogen bonds and London dispersion, are responsible for inducing changes to chemical systems, from simple hydrogen bonds in water to the complex interactions in protein folding. Measurements of these systems are obtained by a variety of techniques, each with specific advantages, but occasionally disadvantages as well.

1.1.1 Analytical techniques for measuring chemical interactions

The understanding of chemical interactions, particularly binding interactions, is vitally important for a variety of chemical fields, from mechanistic studies to drug discovery. Analytical techniques designed for measuring such interactions can typically be divided into three categories: 1) fluorescent techniques, 2) surface-immobilized techniques, and 3) free-solution techniques. Each has a unique set of strengths and drawbacks.

Fluorescence assays, where a fluorescent probe is the source of a signal, are commonly used for many biochemical systems both *in vitro* and *in vivo*. They make use of a fluorophore's ability to emit a photon of light upon excitation of electrons. There are several techniques and methods used to image and measure fluorescence, including

fluorescence resonance energy transfer (FRET), which measures energy transfer between two fluorophores based on their distances from each other; fluorescence recovery after photobleaching (FRAP), which allows for a measure of diffusion through cells; and fluorescence lifetime imaging microscopy (FLIM), which measures fluorescence based on its lifetime rather than intensity like most other methods.[1] Fluorescence characteristics that must be considered for experiments include the quantum yield, a measure of brightness or the ratio of photos emitted to absorbed; fluorescence lifetime, which determines how long an electron exists in the excited state; anisotrophy, a measure of the orientation of the fluorophore's transition dipoles, which must be aligned to the polarization of the excitation light; and any possible quenching or photobleaching, or decreasing or interruption of fluorescence.

Early fluorescence studies starting with fluorescence microscopes date back over 100 years, but early instruments suffered from inadequate light sources. Fluorescence assays today produce some of the lowest detection limits available with high sensitivity in straightforward assays, including at the single-molecule level for a variety of biochemical targets.[2,3] The main disadvantages of these assays are the requirement of lengthy procedures to label, and the risk of interfering with the target's natural binding affinity or mechanism.[4]

Surface immobilized techniques, such as surface plasmon resonance (SPR), require tethering one analyte to a surface for measurements, and have the advantage of performing experiments in real-time and label-free. In SPR, a glass chip with a metal (usually gold) film is used as the surface. Analytes are tethered to the metal film, and their ligands are introduced in solution through a flow channel. Polarized light is directed

onto the glass chip with a prism. As light strikes the surface of the chip at a certain incidence angle, an evanescent wave is generated which interacts with the electrons in the metal layer to generate the plasmons (movements, or oscillations, of electron density), reducing the intensity of the reflected light. The resonance angle can be measured based on where the lower-intensity light is detected, and this angle is based on the refractive index of the channel solution. When analytes bound to the surface of the metal interact and bind with the analytes flowed through the system, the refractive index at the surface changes, so the angle at which the incident light generates plasmons changes, and the intensity of light increases at the initial angle. Binding kinetics can be determined from experiments.[5]

Many biochemical systems have been examined with SPR, including DNA, RNA, proteins, lipids, cells, and potential drug candidates.[5] A schematic of SPR is shown in Figure 1.1. Like fluorescence techniques, sample preparation (namely surface immobilization) can perturb natural binding affinity, particularly for interactions occurring near the surface, as will be discussed in Section 1.3.[6]
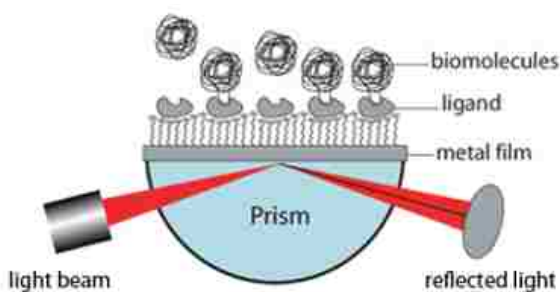
Figure 1.1. Schematic of SPR. As binding occurs at the surface, the dark spot of the reflected light shifts.[7]

Free-solution techniques such as nuclear magnetic resonance (NMR) or isothermal titration calorimetry (ITC) require no additional labeling or surface

preparation. ITC is a free-solution thermodynamic technique which measures heat released or absorbed against a reference cell, as one species is titrated into another, by measuring the power required to maintain an equal temperature between the cells. This technique is often used with biochemical systems, and one of its main advantages is its ability to provide a complete thermodynamic profile with one experiment, including stoichiometry (n), binding association (K_a), and enthalpy and entropy changes (ΔH and ΔS, respectively). Repeat experiments at different temperatures allow for the binding heat capacity, ΔC_p, to be calculated.[8]

To ensure proper reference and temperature matching, the reference cell must contain the same, degassed solvent or buffer as the analytes in the sample cell and syringe. Large background heats of dilutions must occasionally be accounted for, though these are usually negligible. An approximation of the concentration ranges to use is based on the K_a of the complex formed; the product of the K_a and concentration C of analyte in sample cell is equal to the Wiseman Constant, which should be less than 200. The syringe concentration should be at least seven times higher, or 7n for stoichiometries where n > 1, to ensure adequate saturation of the binding isotherm. Figure 1.2 shows a diagram of the instrument.
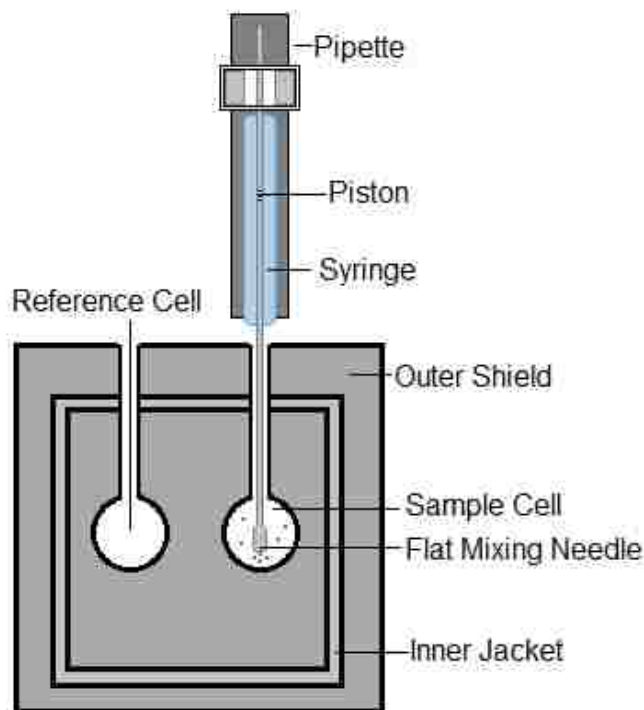
Figure 1.2. Schematic of ITC. The inner jacket and outer shield help control the temperature. The syringe injects analyte into the sample cell while the mixing needle spins at a constant rate to ensure equilibration.

These techniques' main disadvantage is that typically higher concentrations and volumes are required compared to other methods, on the order of several mLs and millimolar concentration as opposed to nanomolar or micromolar. These conditions can be especially disadvantageous since high concentrations can lead to analyte aggregation in some systems. Automated versions of ITC with significantly scaled-down volumes are in development, with the main challenge being their sensitivity.[8]

1.1.2 Interferometry as an analytical technique

Interferometry was first developed in the 1800's with Young's double-slit experiment. In this experiment, he observed the way light behaves when it is directed through two pin holes to form two separate waves, which interact constructively and

deconstructively.[9]   It also was the first experiment to demonstrate light's wave-like behavior.

Constructive Interference
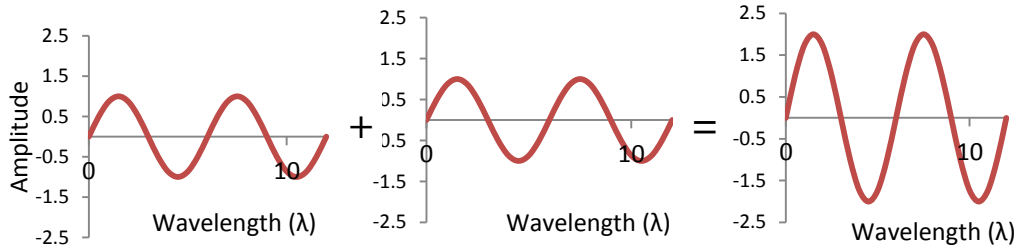
Destructive Interference
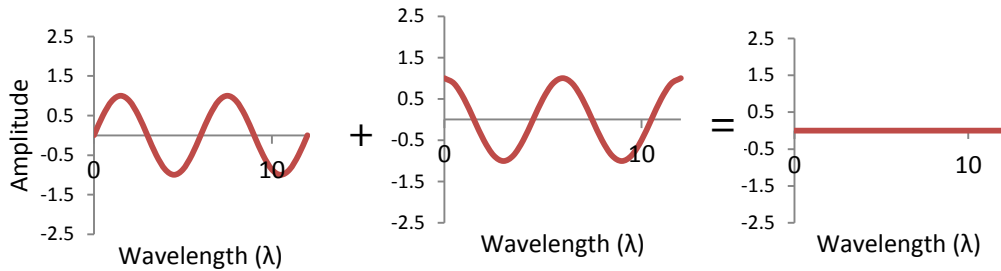
Figure 1.3 Constructive and destructive interference.

In constructive interference, two waves with identical amplitude, frequency, and phase combine to create a wave with twice the amplitude. Conversely, with destructive interference, the waves have the same amplitude and frequency, but opposite phases, so when combined they cancel each other out. These two phenomenon are shown in Figure 1.3 as a combination of sine and cosine waves. A schematic of Young's interferometer is depicted in Figure 1.4.

11
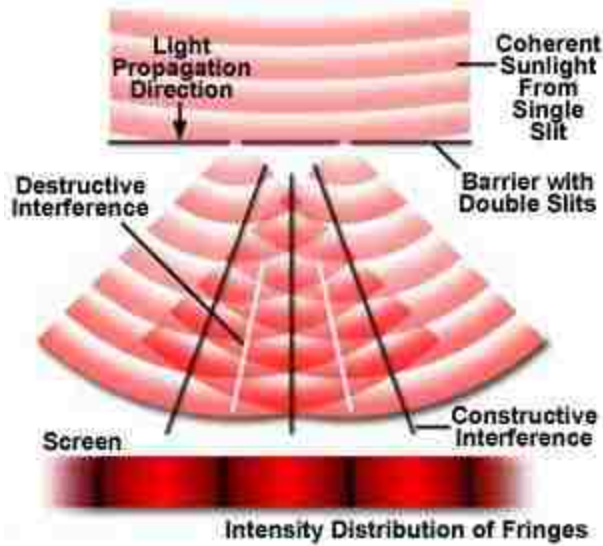
Figure 1.4. Young's double-slit experiment generating an interference fringe pattern.[10]

A combination of constructive and deconstructive interference of light results in an interference fringe pattern, where each 'fringe' is a bright spot, generated by constructive interference, separated by dark spots resulting from destructive interference. Thus, interferometry is the study of waves (usually light/electromagnetic) and the materials with which the waves interact.

While Young's double-slit experiment generated a fringe pattern based on light diffraction, interference fringe patterns can also be generated by light refraction, based on differences in the refractive index (RI) of materials being examined. The refractive index (η) is the ratio of the speed of light in a vacuum (c) to the speed of light through a given material, such as water or glass (v). Instruments that measure interferometry are known as interferometers, and several different types exist for different analytical purposes both within chemical fields and beyond, from seismology to astronomy.

One of the earliest interferometers, which dates to the late 1800's, is the Michelson Interferometer. It uses a single light source, a beamsplitter or half-silvered

mirror, and two mirrors to direct the split beams back to the beamsplitter, where they are recombined. The interference pattern resulting from their recombination is directed onto a detector. Another interferometer, most often used to measure the RI of gases, was the Rayleigh interferometer. In this design, a collimated light source was split into two beams, with each directed through cells or tubes, one of which contained the target gas. The beams were then recombined using a lens, and their interference fringe pattern could then be analyzed. One drawback to this simple design, however, is the high magnification needed to observe the fringes. Another example is the Mach-Zehnder interferometer, which also dates back to the 1890's and uses two beamsplitters and two mirrors to divide and recombine the light. It was typically used to study heat transfer, fluids, and plasmas.[11] Figure 1.5 depicts the basic set-up for these examples of interferometers.
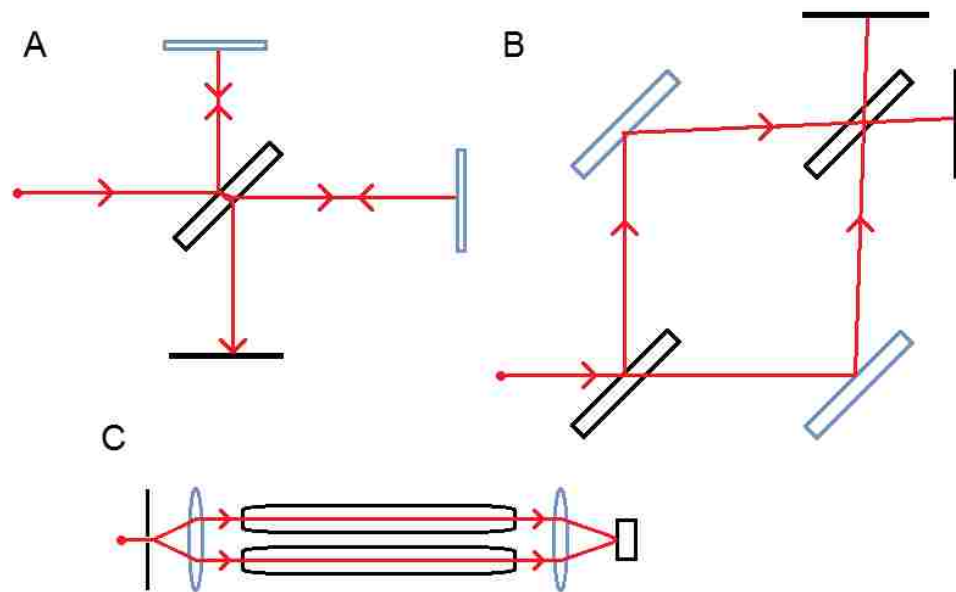
Figure 1.5. Schematics of interferometers, with the mirrors or lenses in blue and the red line representing the path of the light beams. A) Michelson Interferometer with one screen, B) Mach-Zehnder Interferometer with two detectors, and C) Rayleigh Interferometer, where one of the tubes would be filled with gas/gas mixture for analysis.

13

Interferometers have been used to make a variety of measurements at both the micro and macro scale, including measuring the radii of celestial objects,[12] evaluating the quality of lenses or mirrors,[13] imaging ocean currents,[14,15] and biosensing. A type of Mach-Zehnder interferometer was used as a biosensor beginning in 1993, and had the advantage of minimizing temperature-related drift due to the two pathways containing a reference and a sample that could be measured simultaneously.[16] Most recently at the macro scale, a modified Michelson Interferometer at the Laser Interferometer Gravitational-Wave Observatory (LIGO) confirmed the existence of gravitational waves predicted in Einstein's theory of general relativity.[17]

1.2 Backscattering Interferometry as an analytical tool

1.2.1 Development of the backscattering interferometer

BSI began as a refractive index detector for liquid chromatography separations in the late 1990s, and evolved to fit a growing need for highly sensitive, miniaturized platforms. Initially known as micro-interferometric backscatter detection (MIBD), it was shown by Darryl Bornhop to be a universal detector capable of measuring changes in refractive indices at small volumes, with a probe volume of ca. 1.2 nL, and high sensitivity, with a detection limit refractive index change of ca. 10^{-7} RIU. A 1999 study reported it was able to detect four different solutes (NaCl, phenol, toluene, and ethylbenzene) in a mixture at ppm levels.[18] This precursor used a capillary mounted on a stage rather than a chip, where the monochromatic laser light could impinge perpendicular to the capillary to generate the backscattered interference fringe pattern, as

shown by the diagram in Figure 1.6. Alignment of the setup was tedious, and only one or

two fringes' intensities and positions could be measured at a time by the detector.
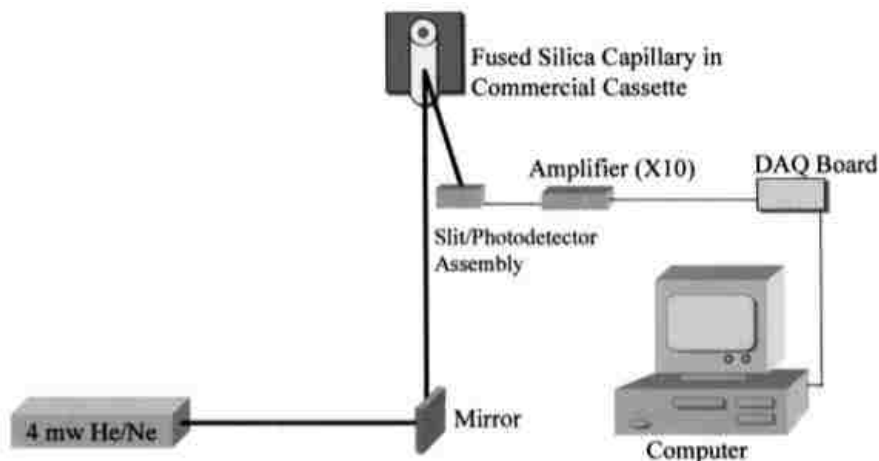
Figure 1.6. Schematic of MIBD setup.[18]

By 2000, the Bornhop group had developed a chip-scale version of the

backscatter detector that was used with capillary electrophoresis, which provided

detection limits of 10^{-6} RIU for solutions.[19] The etched channels in a glass chip allow for

a multipass optical configuration, which allows for the light to pass through the sample

several times and increases the effective path length to lower the detection limit, as

shown in the optical ray trace in Figure 1.7.
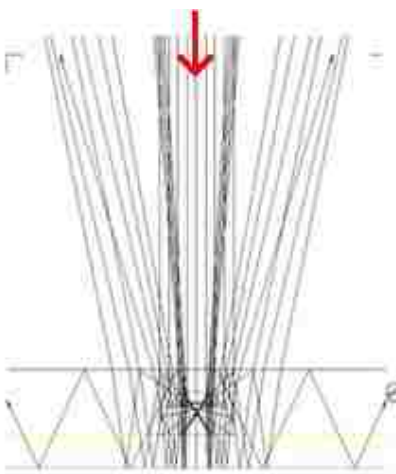
Figure 1.7. Optical ray trace showing the laser light entering the chip and passing
through multiple times before exiting.[20]

15

The instrument used in this thesis is shown in Figure 1.8. The microfluidic chip containing the analytes is secured to a translational stage for proper alignment. A helium neon (HeNe) laser is directed via fiber optic couple to a mirror above the stage, aligned so the light impinges the chip perpendicularly. The light interacts with the analytes in the chip's channel and is backscattered by the mirror to a charge-coupled device (CCD) detector. A density filter prevents the intensity of the light from overpowering the detector. Since RI is temperature dependent, with a particularly high $d\eta/dT$ for liquids (1 x 10^{-4} °C in H_2O), the stage is temperature-controlled via a peltier device, thermistor, and aluminum heat sink. In most experiments, the stage is heated to 25 °C. Solutions are injected via pipette into one well of the channel, and vacuumed out the opposite well prior to introduction of the next sample.
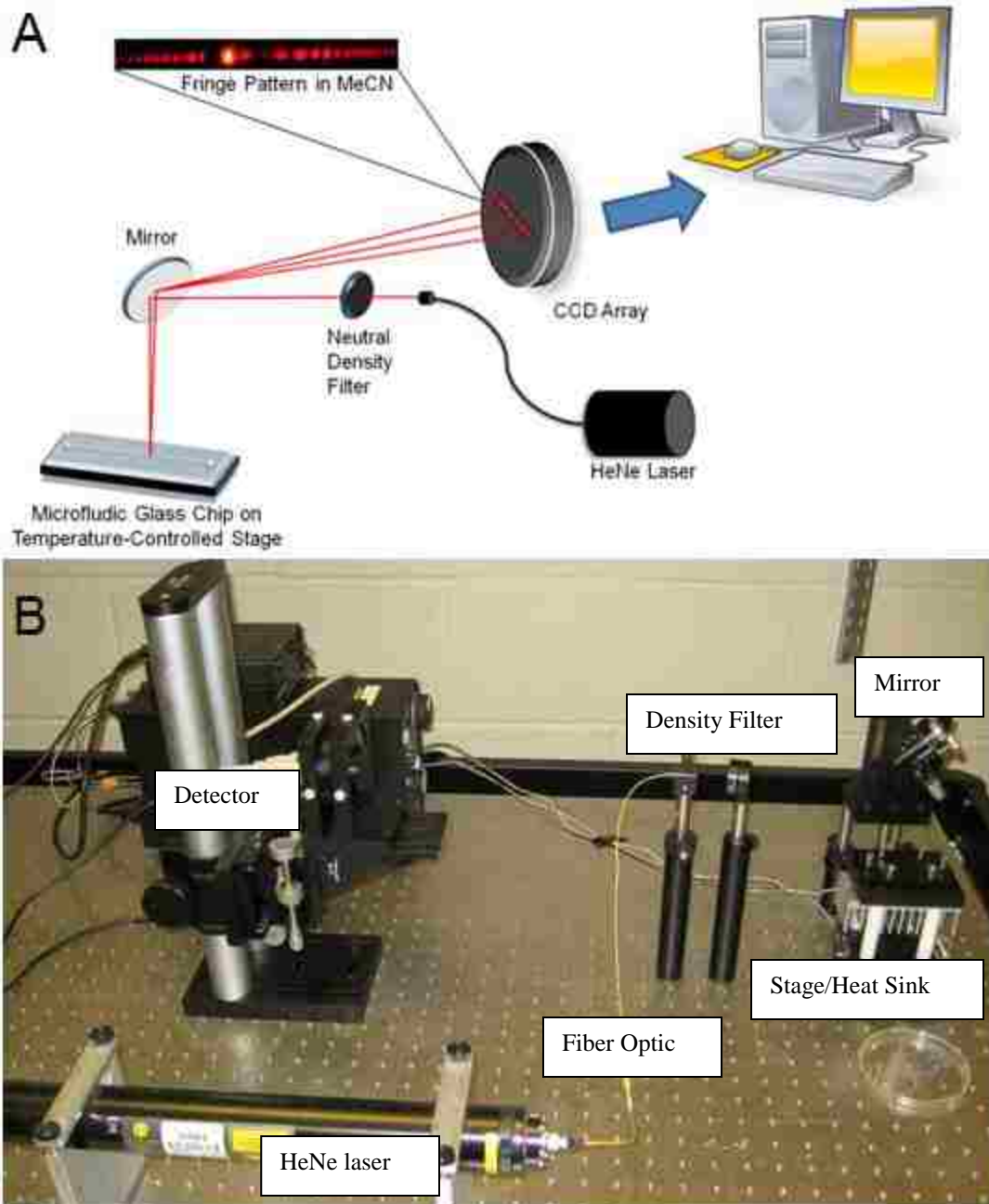
Figure 1.8. A) Schematic of BSI with a sample fringe pattern as seen on the detector.[21] B) Photo of BSI setup.

1.2.2 Microfluidic glass chip

Analytes (receptor and ligand) are injected into channels within a borosilicate glass chip ($\eta = 1.52$) for analysis with BSI. The chip contains three parallel, semicircular

channels etched into the glass which feature hydrophilic walls when untreated. Surface

treatments, typically silanization, can be used to functionalize the channel walls and

render them hydrophobic. Silanization is usually necessary for charged biological

systems, including two of the studies featured in this thesis.

Initially, the channels in the chips were 90 µm wide, and the probe volume, that

is, the volume of solution within the channel hit with the laser light, was ca. 360 pL.

Presently, the chips now feature wider channels, with a 210 µm width, and a 7.52 nL

probe volume. Figure 1.9 depicts how the probe volume is determined. The wider width

and larger probe volume allows for more signal generation due to the increased volume

of analytes being interrogated by the laser light at a given time. It also helps decrease

clogs in the channels due to a build-up of residues from repeated use, particularly with

the silanization solutions (one of which is a saturated potassium hydroxide (KOH)

solution in methanol, which tends to evaporate readily at the small volumes used for the

procedures).
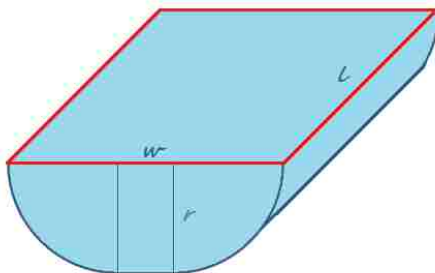
Figure 1.9. Probe volume of the semi-circular channels within the microfluidic chip, where $r = 100$ µm, $w = 10$ µm, and $l = 450$ µm (the diameter of the laser beam).

The chips generally last for two to three years before wear can be seen along the

channels under a microscope for unsilanized chips, and for chips that are frequently

functionalized this lifetime is considerably shorter, on the order of about a year. They are

cleaned by rinsing with water and sonication for short periods of time (usually 30 min). Clogs can usually be cleared by short soaks with concentrated nitric acid; more severe clogs or build-up along the walls may require a dilute piranha solution (H_2SO_4 and H_2O_2) or a dilute Contrad 20 solution soak for 1-2 min. Clogs in the channels are best avoided by frequent rinsing, and avoiding evaporation during procedures that require longer soaking in solutions.

1.2.3 Data acquisition

Real-time measurements are obtained by the computer with a fast Fourier transform (FFT) analysis of the fringes that appear on the CCD detector. Typically six fringes are analyzed by the detector. Fringe selection is vital; the fringes must be a certain distance away from the centroid, and have high contrast, Gaussian or sigmoidal shape, and low noise. Background light must also be avoided, so experiments are done in the dark. Figure 1.10 compares a good fringe pattern to a few examples of poor fringe patterns.
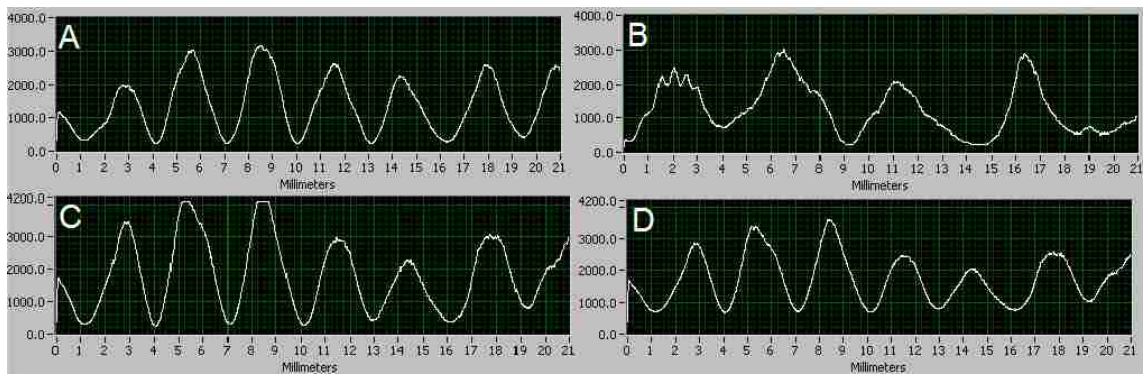
Figure 1.10. A) A good fringe pattern, with high-contrast, Gaussian-shaped peaks of similar size and shape. B) A poor fringe pattern, with noisy peaks of inconsistent sizes. C) A fringe pattern with an intensity that's maxing out the detector due to too high an integration time. D) A fringe pattern that is affected by background light.

Proper alignment of the components (laser, mirror, chip, and detector) is also essential for successful experiments. Parallel rays of the laser beam should evenly

impinge the channel perpendicularly, so that the fringes (bright spots) on either side of the centroid have equal intensities. Additionally, examination of the optical ray trace (Figure 1.5) reveals that not all fringes originate from the same spot on the chip; some are nearer to the surface or edge of the channel, thus these would report a weaker free-solution signal compared to those originating from the central part of the channel (where most of the energy, or rays, would be directed). The FFT of the fringes in the desired region (typically around fringes 6-14 from the centroid) generates a nearly single spatial frequency; a pure single frequency is not obtained due to signal mixing from the rays that interrogate portions of the solution nearer the surface or edges. This measured frequency remains constant as the fringes shift spatially upon RI changes, and the LabView software used for data collection displays both the fringes and the FFT in real time, as shown in Figure 1.11.
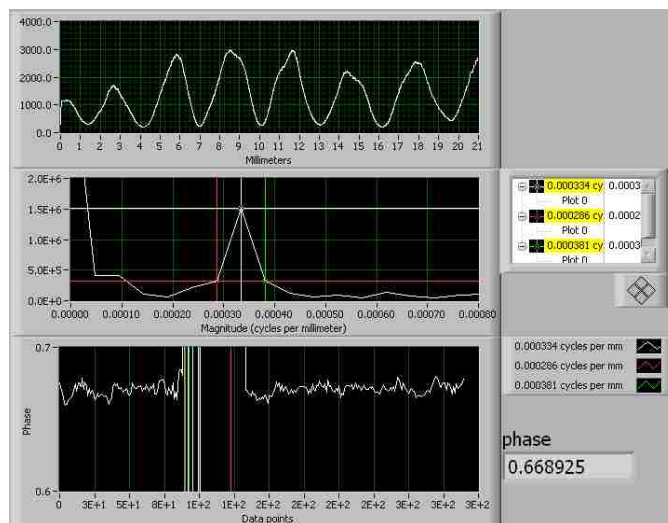
Figure 1.11. Data collection screen, with the fringes (top), FFT with a large, nearly-single frequency peak (middle), and phase collection (bottom).

To ensure that the signal being measured is a result of only the desired interaction, and not concentration-dependent effects, or background or buffer interactions, reference

solutions must be made to match with each sample binding solution, where the only difference between the reference and sample is the presence of the receptor. These can then be subtracted from the signal during data analysis. Similarly, surface interactions must be minimized, so silanization or other functionalization of the channel walls may be necessary. Repeated injections of buffer after each trial check the signal's return to the established baseline to ensure that surface adsorption is not causing a spurious signal. Keeping these factors in mind when designing experiments, it is possible to measure binding even in complex media such as serum.[22]

1.2.4 BSI Calibration and limits of detection

The BSI is calibrated with a series of glycerol solutions in water at increasing concentrations. The signal of each sample is plotted versus the concentration. A linear $d\eta/dC$ relationship is observed, as depicted in Figure 1.12, and a minimum of three trials are performed in order to determine the standard deviation of the signal.
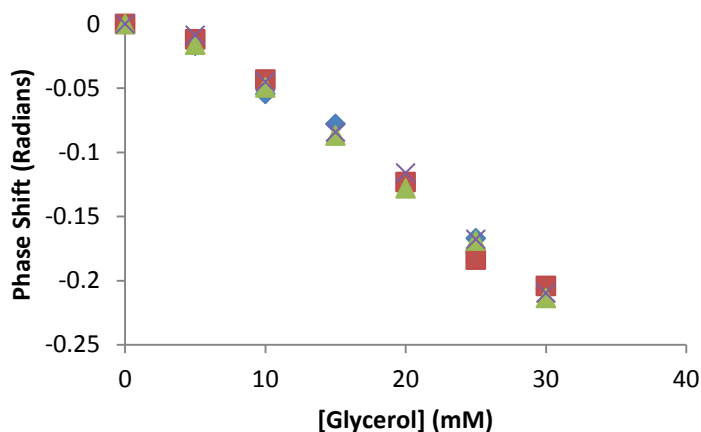
Figure 1.12. BSI signal versus glycerol concentration calibration curve.

To ensure a high level of confidence in the detection limit, 3σ statistics is used. The detection limit of the instrument can then be calculated in terms of either refractive index units (RIU, η) or concentration (C) in mM with Equations 1 and 2:

$$LOD_\eta = \frac{3\sigma}{|m|} \cdot \frac{d\eta}{dC_{gly}}$$
(1)

$$LOD_{C_{gly}} = \frac{3\sigma}{|m|}$$
(2)

where LOD is the limit of detection, σ is the standard deviation, m is the slope of the signal vs concentration line, and $d\eta/dC_{gly}$ is the change of RI with a change of glycerol concentration, a given value that can be found in references such as the CRC Handbook.[23] When calibrating the BSI, acceptable target values for the limit of detection (LOD) in RIU is on the order of 10^{-6} RIU, and in concentration of glycerol is < 2.0 mM. Additionally, because the instrument is exposed, environmental conditions can disrupt measurements, so stable room temperature, pressure, and humidity are vital.

1.2.5 Data analysis

The binding of two species essentially creates an entirely new, unique species with a new, unique RI, which causes a significant signal change. Specifically, changes in conformation, solvation, polarizability, etc contribute to the signal changes, the details of which will be discussed in Section 1.4. The two species are referred to as a receptor and a ligand. A dissociation constant (K_D) can be calculated from steady-state, or endpoint, assays by holding the receptor at a constant concentration in a series of samples while increasing the concentration of the ligand towards saturation. Equation 3 shows how the K_D is calculated from an end-point BSI experiment when plotting signal versus concentration of ligand, where x is the concentration of ligand and y is the phase shift.

Since B_{max} has units of the y-axis at maximum binding, it is the maximum phase shift of the product upon reaching its maximal concentration.

$$y = \frac{B_{max}*X}{K_D+X} \tag{3}$$

$$[R \cdot L]_\infty = \frac{[R]_0 \cdot [L]_0}{[L]_0 + K_D} \tag{4}$$

The law of mass action (eq 4) states that the rate of a reaction is proportional to the product of the masses of the reactants, in other words, for a reaction mixture at equilibrium (such as BSI endpoint experiments), the ratio between the concentration of the reactants and concentration of the products remains constant. Here $[R \bullet L]_\infty$ is the concentration of the product complex at infinite time (equilibrium), $[R]_0$ is the initial concentration of receptor, $[L]_0$ is the initial concentration of the ligand, and K_D is the dissociation constant. The K_D of a system is the inverse of the association constant, K_a, determined with instruments such as ITC. This allows for a comparison of BSI results to other techniques, and also means that a lower K_D is indicative of a stronger affinity in a given system with the same receptor and various ligands.

When designing BSI experiments, it is important to work in concentration ranges that generate a measurable phase shift from the product formed while avoiding concentrations that are too high that the $d\eta/dC$ of the product is above the noise level. A general rule of thumb for determining acceptable ranges are receptor concentrations of approximately $K_D/10$, and ligand ranges spanning at least two to five times higher in order to reach saturation. If the K_D is unknown, ranges may be approximated by running a $d\eta/dC$ experiment, similar to the glycerol calibration, of serially diluted samples of product.

23

1.3 Previous BSI experiments

1.3.1 Protein binding with various ligands

Various protein binding interactions have been studied with BSI in the past decade. A good example is Calmodulin (CaM), a calcium-selective messenger protein, with several ligands.[24] Upon binding with four Ca^{2+} ions, CaM undergoes a significant conformational change, as depicted in Figure 1.13A. The binding curve produced from free solution BSI experiments of CaM with Ca^{2+} is shown in Figure 1.13B. It was hypothesized that the significant conformational change of the protein was the main source of the large signal.

A

B
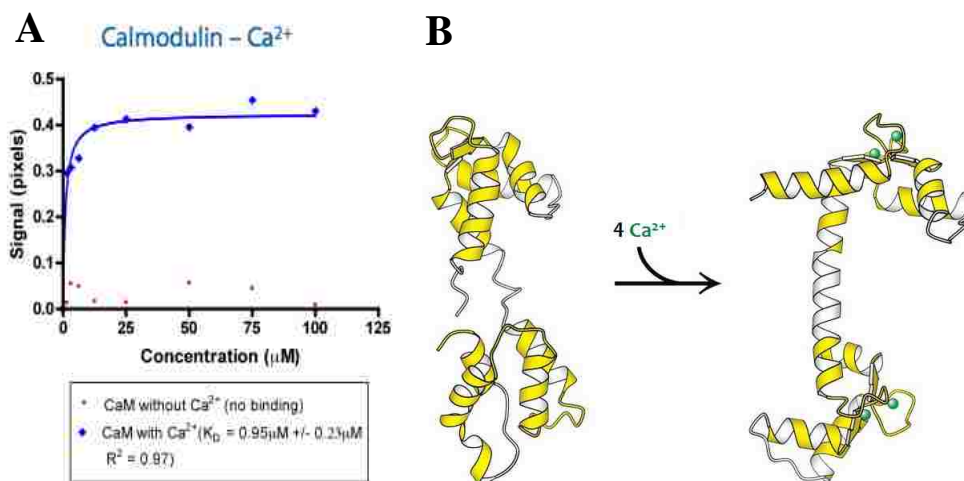
Figure 1.13. A) BSI binding curve of CaM with Ca^{2+}.[25] B) Conformational change that occurs in CaM when four calcium ions are bound.[26]

CaM undergoes another conformational change when its Ca-bound form interacts with another ligand. There are a wide range of potential targets, and the ligands included in this study were trifluoperazine fluoride (Tfp), a small molecule; a 17-residue peptide known as myosin light chain kinase peptide (M13); and the protein calcineurin (CaN). Each ligand resulted in a measurable binding curve and calculated K_D values. Binding curves and a representative conformational change are shown in Figure 1.14.
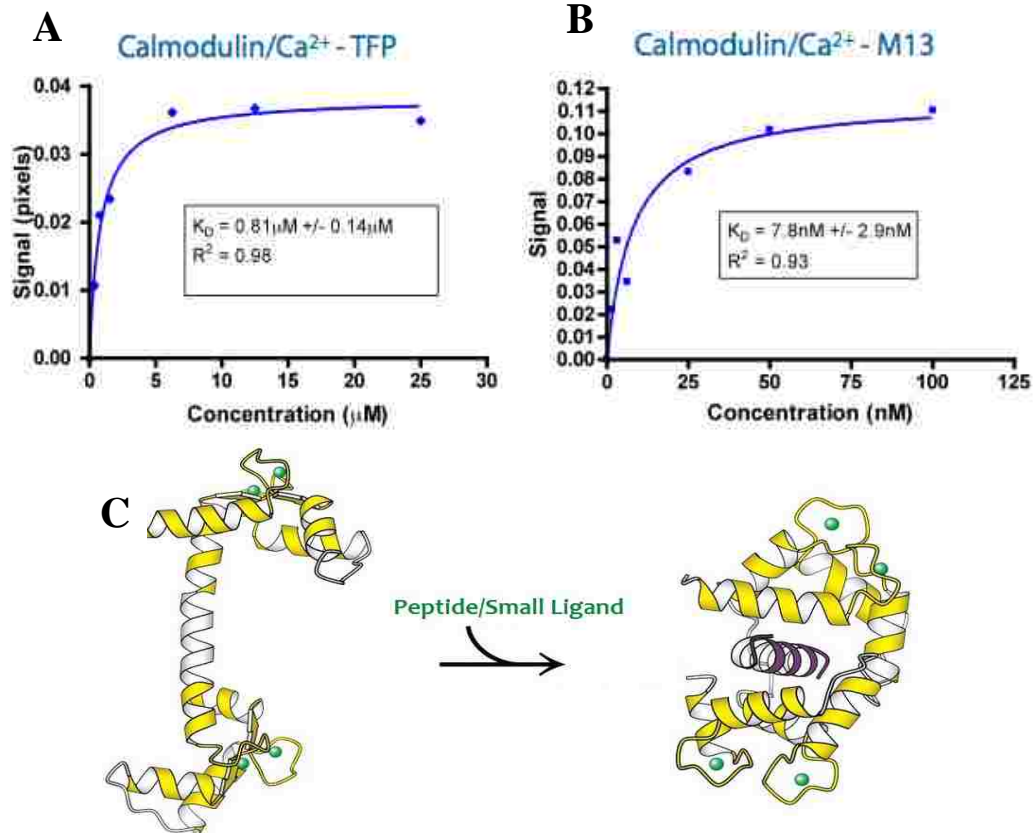
Figure 1.14. A) BSI binding curve of CaM/Ca^{2+} with small molecule Tfp. B) BSI binding curve of CaM/Ca^{2+} with M13 peptide.[25] C) Conformational change that occurs when CaM/Ca^{2+} binds with a small peptide or ligand.[26]

1.3.2 A direct comparison of free-solution and surface-tethered interactions

When designing analytical assays for biochemical systems, ideal conditions would be physiologically relevant in terms of temperature, concentration, and the form of the analytes. Many analytical techniques rely on fluorescence labeling or surface tethering of one analyte. While these actions provide a way to obtain a desirable signal, several studies have shown that they can also impact binding affinity. Several studies involving fluorescently-labeled DNA showed that, depending on the structure or sequence of a DNA strand, the fluorophore could stabilize its hybridization to a

complementary strand or alter the equilibrium by changing the thermodynamics of the system.[27,28]

Surface immobilization can also have an effect on binding, particularly if the binding interaction occurs close to the surface due to changes in the chemical environment as well as steric effects. For example, this was shown to have a significant impact on DNA hybridization as a consequence of the charged phosphate backbone.[29] Melting studies, kinetic assays, and other techniques were developed in an attempt to quantify the amount of perturbation caused by immobilization, but no technique prior to BSI was able to yield a direct comparison to untethered measurements at physiological conditions. BSI experiments are typically designed to be conducted in free solution, but the ability of the channels in the glass chip to be chemically modified means that it is also possible to tether the receptor to the surface and obtain binding data from surface-immobilized experiments. Additionally, BSI can also be used to measure binding affinity differences between fluorescence-labeled and unlabeled duplexes.

The BSI studies used 30-base pair DNA oligonucleotides: a probe strand (P_s) was used as the receptor in each experiment, and five different binding strands served as the ligand: 1) an unlabeled complement, 2) a fluorescein isothiocyanate (FITC)-labeled complement, 3) a cyanine-3 (Cy3)-labeled complement, 4) a terminal CA/AC mismatch, and 5) an internal AG/GT mismatch. Two adjacent mismatched base pairs were also expected to have a significant impact on binding affinity. The effect of various types of polymorphisms was expanded in a later study discussed in Chapter 3. ITC and UV-hyperchromicity experiments were used to benchmark BSI results. Fluorescence imaging

was used to confirm that surface-tethered DNA strands were not removed when the binding strand was rinsed away with buffer.[6]

Each of the hybridization experiments were carried out in both free-solution and surface immobilized with BSI. For the surface immobilized experiments, in addition to the silanization modification necessary for charged biomolecules, the P_s was tethered to the microfluidic chip by an ExtrAvidin-biotin interaction. ExtrAvidin, a modified version of the protein Avidin, was chemically linked to the silanized walls, and the P_s was labeled with biotin, a small molecule with very high, specific affinity for ExtrAvidin. With BSI, surface immobilized, fluorescence-labeled, and free solution-label free DNA hybridization could be measured at the same, physiologically-relevant conditions, and the K_D values determined from each binding curve provided a direct comparison to binding affinity for the first time. The results of these experiments are shown in Table 1.1.[6]

Table 1.1. K_D results of free-solution and surface-immobilized BSI experiments.[6]

DNA Strand	Free-Solution BSI K_D (nM)	Surface-Immobilized BSI K_D (nM)
Unlabeled	27.4 ± 4.7	66.1 ± 8.4
Cy3-labeled	19.6 ± 5.8	41.7 ± 6.3
FITC-labeled	17.4 ± 2.9	45.6 ± 7.7
Terminal Mismatch	28.9 ± 2.4	60.7 ± 7.9
Internal Mismatch	110.4 ± 11.6	132.5 ± 16.6

When comparing the K_D's of each binding strand in free solution vs. surface-immobilized strands, a clear trend can be seen. The P_s immobilized to the chip perturbs binding (increases K_D) by ca. 50% in all cases except for the internal mismatch, which

was already significantly destabilized compared to the complement. When comparing

the K_D's of the unlabeled complement to the FITC- and Cy3-labeled versions, the trend

observed is a modest decrease in K_D, or a stabilization of the duplex. The results from

this study were the first instance that the effects from fluorescence tagging or surface

immobilization could be quantified and directly compared to the unlabeled, free-solution

experiment using the same instrument and conditions, and demonstrated BSI's unique

ability to allow for these direct comparisons. Others have demonstrated this ability with

BSI, as well.[30]

1.4. Origin of the BSI signal

Refractive index has a well-established response to changes in concentration and

temperature, yet there are nearly a decade's worth of reports of BSI measuring protein

folding, or interactions with small molecules or ions in free solution, where a readable

signal is generated with little to no mass change. Experiments are frequently designed

where the individual ligands or receptors do not produce a $d\eta/dC$ signal that is readable

above the noise level of the instrument separately, but upon binding produce a

significantly larger, measurable signal. Therefore changes in the bulk RI of the solution,

arising from conformational, solvation, and polarization changes, have been attributed to

the BSI signal obtained during binding events, but a more precise explanation or

quantification of these effects had been unavailable until very recently. Using a training

set of systems tested on BSI over the years and computed structural information from

sources such as the protein databank (PDB), an expression known as the Free Solution

Response Function (FreeSRF) was developed by Bornhop and coworkers to describe the

source of the signal in free solution BSI experiments.[31] They first compared the

28

technique to another technique that measures changes in RI that were typically attributed to dη/dC changes, SPR.

1.4.1. SPR signals are more than a mass-weighted response

Sota and coworkers were the first to question the idea of RI changes being solely related to dη/dC effects with SPR, and reported a signal attributed to conformational changes of tethered dihydrofolate reductase induced by acid denaturization.[32] Beginning in 2000, other groups reported RI signal changes resulting from conformational changes with SPR, as well. Gestwicki and coworkers identified small-molecule induced conformational changes on proteins where a negative ΔRI correlated with a decrease in the protein's hydrodynamic radius, and a positive ΔRI resulted from an increase in hydrodynamic radius. Specifically, they noted a signal resulting from calcium binding to tissue transglutaminase of ca. 1000 resonance units (RU), which they attributed to a significant change in hydrodynamic radius. Taking into account just the added mass of the calcium ion, in comparison, would only result in an increase of 28 RU.[33] Similarly, they reported a net negative ΔRI resulting from small molecule binding to a protein, which would be expected to give a positive ΔRI when only considering the mass-related, incremental responses.[33]

Despite the evidence, several later reports attributed these observations to anomalies or improperly prepared samples,[34–36] but more studies supporting the argument that conformational changes produce free-solution signals continued to emerge. Koch and coworkers noted SPR signals from Ca^{2+} binding to myristoylated recoverin (mRec) much higher than expected when only considering the minor mass changes. Using NMR, they identified that unbound mRec had a 'tense' (T), or compact, conformation, whereas

calcium-bound mRec had 'released' (R) conformation that was much more extended and open. Changing from T to R results in an increase in the radius of gyration (R_{gyr}) and solvent-accessible surface area (SASA), and thus the hydration shell is altered, which they postulated alters the overall RI of the solution.[37,38]

In all of these cases, the signal could be observed despite the background surface interactions arising from mass changes on the surface. With BSI and the availability to measure changes in RI in free-solution, it was possible to reduce these competing signals and begin developing the hypothesis, and then a model, that free-solution binding events can be detected based on changes in conformation and solvation.

1.4.2. The Free-Solution Response Function

The calmodulin system studied by the Bornhop lab and discussed in Section 1.3.1 was the first system examined in order to determine a model to describe the free-solution BSI signal. Structural information from the PDB of bound and unbound CaM was used to estimate the SASA and R_{gyr} and relate them to the signal phase change. The investigation then expanded to a "training set" of other binding partners to develop the Free-Solution Response Function (FreeSRF), an expression that mirror's Beer's Law, shown in Equation 3.

$$\rho = \chi \beta C \tag{3}$$

Here, ρ is the phase shift, or FreeSRF signal, in radians, χ is the molar refractometry of the product (bound [ligand-receptor] complex) in RIU/M, β is the instrument response function in radians/RIU, and C is the product concentration in M. The molar refractometry, χ, is an intrinsic property of the species, mirroring the molar absorptivity of Beer's Law. It accounts for properties such as molecular dipole moment,

the dielectric constant, and other parameters that may be altered as a consequence of a binding interaction. Experimental values (χ_{exp}) may be calculated for a given species based on BSI experiments. To do so, C must be determined from the mass balance equation, and β must be determined for the specific instrument on which the experiment is conducted.

The mass balance equation relates the K_D of a binding system to the concentration of free receptor [R], ligand [L], and bound complex ([RL]) as shown below:

$$K_D = \frac{[R][L]}{[RL]}$$

(4)

Total amounts of receptor and ligand can be defined as follows:

$$[R]_{tot} = [R]_{free} + [RL] \tag{5}$$

$$[L]_{tot} = [L]_{free} + [RL] \tag{6}$$

Therefore the equation for K_D can be rewritten as follows:

$$K_D = \frac{([R]_{tot} - [RL])([L]_{tot} - [RL])}{[RL]}$$

(7)

This equation can be rearranged to a quadratic to make it possible to solve for [RL] by using the quadratic equation (which yields two possible answers, only one of which is physically relevant). This allows for the total concentration of bound product to be determined at each point on the binding curve.

$$[RL] = \frac{([R]_{tot} + [L]_{tot} + K_D) \pm \sqrt{([R]_{tot} + [L]_{tot} + K_D)^2 - 4[R]_{tot}[L]_{tot}}}{2}$$

(8)

31

In order to determine β for a given BSI instrument, glycerol $d\eta/dC$ calibration data are used to obtain the slope of the phase shift vs. concentration of glycerol relationship. This is expressed in radians/mM. β is expressed in radians/RIU, so a conversion factor in RIU/mM for the $d\eta/dC$ of glycerol is used (obtained from the CRC).[23]. For the BSI instrument used for this research, β is calculated as follows:

$$\beta = \frac{-0.009978 \ \frac{\text{radians}}{\text{mM}}}{1.04863 \ \times \ 10^{-5} \ \frac{\text{RIU}}{\text{mM}}} = -957.6 \ \frac{\text{radians}}{\text{RIU}}$$

(9)

Since ρ values at the lower concentrations of an end-point assay will have more error due to reduced signal-to-noise ratio (S/N), experimental χ values should be determined with ρ_{Bmax}, which is simply where $\rho = B_{\text{max}}$ from the one-site binding equation of the BSI data used to determine the K_D. At the maximum signal, the concentration of newly-formed product is approaching that of the receptor concentration; the mass-balance equation shows that adding increasingly higher concentrations of ligand does not produce a linear increase in product concentration.

From the experimentally determined χ values, an expression for modeled χ values was developed that included terms for the changes in solvent-accessible surface area (ΔSASA) and radius of gyration (ΔR_{gyr}) from unbound to bound species, in angstroms squared and angstroms, respectively, as shown in equation 10.

$$\chi_{\text{model}} = A(\Delta\text{SASA}) + B(ave\text{SASA}) + C(\Delta R_{gyr}) + D(ave R_{gyr}) + E \quad (10)$$

The aveSASA and aveR$_{\text{gyr}}$ is the average of those values based on the number of available structures (e.g. from PDB), and A, B, C, D, and E are fitting coefficients. R_{gyr}

can be calculated from the following expression (11), where r is the position and m is the mass of each atom.

$$R_{gyr} = \sqrt{\frac{\sum_{k=1}^{N} m_k \, (r_k - r_{mean})^2}{\sum_{k=1}^{N} m_k}}$$

(11)

Bornhop and coworkers used computational programs (such as Chimera) to determine these parameters for several ligand-receptor pairs of which BSI data was already available. They then used regression analyses to determine the coefficients A-E. This allowed for a comparison of experimental and computationally-determined results.

1.4.3. Evaluating the fit of the FreeSRF models

In order to evaluate the FreeSRF calculations, a training set of a variety of binding partners was used to compare experimental and modeled χ and ρ values. This training set included a variety of types of receptors, including proteins (Calmodulin, Carbonic Anhydrase II, etc) and antibodies (IL-2 Antibody), and their ligands, including peptides (calcineurin), small molecules (glucose, mannose), and metal ions (Ca^{2+}). Comparisons of experimental and modeled χ values from a variety of receptor-ligand binding pairs in the training set resulted in a decent fit which was further improved by dividing the data sets of binding pairs into "large" and "small." This division was based on the magnitude of the signal, or FreeSRF (ρ_{exp}), and χ (generally <100 RIU/M or >>100 RIU/M). Table 1.2 lists a few of the receptors and ligands, and a comparison of their experimental and modeled χ values.

Table 1.2. Comparison of χ_{exp} and χ_{model} to evaluate the FreeSRF expression. Training set systems are divided into large and small models based on the experimental χ. Some receptors are in both large and small models depending on their binding ligand.[31]

Large Model					Small Model				
Receptor	Ligand	χ_{exp} (RIU/M)	χ_{model} (RIU/M)	% Error	Receptor	Ligand	χ_{exp} (RIU/M)	χ_{model} (RIU/M)	% Error
IL-2 Ab	Interleukin-2	827,964	823,965	0.5	CaM	TFP	75.2	73.6	2.2
Basigin	Rh5	215,777	212,174	1.7	CAII	Sulpiride	62	60.2	2.9
CAII	Acetazolamide	-57,291	-42,419	26.0	Con A	Glucose	2.6	4.6	78.1
CaM	Calcineurin	46,087	37,389	18.9	Rec	Ca2+	78	78.1	0.1

The results of the Bornhop group's training set show an overall good correlation and low to moderate percent error between χ_{exp} and χ_{model}. Additionally, the model was also able to predict the sign of the signal.

The initial training set used to evaluate FreeSRF was acquired first by experimental data over several years and instruments by the Bornhop group, and then modeled using the FreeSRF expression and the bound complexes' ΔSASA and ΔR_{gyr}. Next, they sought to use the model to obtain calculated χ and ρ values of two binding systems, and then prepare BSI experiments to test the validity. The two systems were recoverin with Ca^{2+}, a protein-ion binding system, and carbonic anhydrase II with dansylamide, an enzyme-inhibitor system. Figure 1.15 shows binding curves obtained from BSI experiments, and from calculating ρ using χ_{model} at each concentration of ligand used in the experiments. The results correlated well, with a percent difference for χ_{model} of 0.13% for the recoverin-calcium system, and 18.0% for the carbonic anhydrase-dansylamide system.
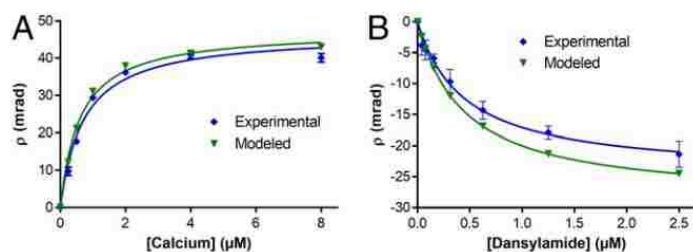
Figure 1.15. Experimental (blue) and modeled (green) binding curves for (A) recoverin-Ca^{2+} and (B) carbonic anhydrase II-dansylamide.[31]

These initial results indicate that FreeSRF works as a model to describe the source of the signal in BSI, but the Bornhop group acknowledge that more refined expressions for FreeSRF can still be developed. The arbitrarily-assigned 'large' and 'small' model sets could be further expanded, for example with longer, narrower-shaped molecules (e.g. nucleic acids) rather than more globular-shaped molecules (e.g. proteins). Small molecule hydrogen-bonding systems have been examined with BSI,[39] but could also be used to refine the FreeSRF expression. Additional parameters could be included to account for more electronic changes, for example in instances of oxidation and reduction. The development and refinement of the FreeSRF expression and new BSI experiments will continue to help advance fields of biosensing and molecular detection.

1.5. Overview of Doctoral Research

Several different biochemical and chemical systems were designed to demonstrate BSI's versatility, to develop experiments that could be expanded for screening other systems or ligands, and to examine the source of the signal and evaluate the FreeSRF expression, particularly in nonaqueous media. All were performed in free solution. Chapter 2 describes a study using BSI to measure the affinities of Acetylcholinesterase (AChE) and several known and novel inhibitors, and to evaluate their potential as anti-

Alzheimer's Disease agents; we hypothesized that values would correlate well with IC_{50} values obtained from colorimetric assays and thus highlight the relative ease of BSI experiments to use for screening instead. Five commercially available inhibitors: galantamine, edrophonium, propidium, physostigmine, and BW284c51 were studied in order to benchmark the inhibitory K_D values determined with BSI. Next six novel inhibitors prepared by the Heindel Lab were studied, and the BSI results were compared to IC_{50} values determined via Ellman's assay.[40] Comparison of both techniques' results gave valuable insight into the inhibition mechanisms. This is especially useful for screening for potential anti-Alzheimer's disease agents that have affinity for the allosteric site of the enzyme.

Chapter 3 discusses experiments designed to test our hypothesis that BSI could distinguish between a complementary DNA duplex and ones containing different single nucleotide polymorphisms (SNPs). This work was expanded from initial experiments with 30-base pair oligonucleotides and two adjacent mismatched SNPs. Here, 20-base pair oligomers were used to be more consistent with other techniques used to study SNPs, and six duplexes were studied with a constant probe strand: a perfect complement, a nonbinding nonsense strand, and two each of a deletion and mismatch SNP at different locations within the sequence (centrally-located, or four base pairs from the 3' end). Melting transition temperatures obtained with CD were used to benchmark the BSI results. In addition to basing results on the K_D values determined and how they compared with the melting temperatures obtained via CD, we also noted interesting observations concerning the magnitude of the signal, namely that the complementary duplex produced a much higher phase shift compared to the SNP-containing duplexes.

The next project (Chapter 4) examined a series of small organic molecules acting as ion-recognition systems, or ionophores, in nonaqueous solvent (acetonitrile, MeCN). The goal was to observe their interactions via BSI to gain insight into FreeSRF and the source of the BSI signal, particularly from the effects of solvation in nonaqueous media, and in systems that do not undergo a significant conformational change typical in many biochemical systems. Systems studied include four potassium-selective ionophores, 18-crown-6, potassium ionophore I (also known as Valinomycin), potassium ionophore II, and potassium ionophore III. Ionophore II and III's motion as each 'captures' a potassium ion mimics that of some larger, biomolecular recognition systems; as a result, both this conformational change and any solvation changes within the system were expected to have an effect on the BSI signal.

18-Crown-6 binding to potassium produced a smaller signal compared to the other ionophores. BSI results of potassium binding with 18C6, ionophore I, and ionophore II yielded binding curves in the negative direction. Potassium Ionophore III is structurally similar to the ionophore II, with one notable exception being a dodecyl chain in the middle of the linker between the two 15-crown-5 ends. This hydrocarbon tail has a significant impact on the signal and resulted in a positive saturation curve after an initial negative phase shift.

Finally, other information that can be determined with BSI experiments is discussed. The stoichiometry of a binding system can be determined even at those greater than 1:1, provided a single rise-to-max curve is generated. Decomplexation of the valinomycin-potassium complex upon addition of water is observed. Future experiments

37

are also proposed, including studies involving solvation effects, hydrogen-bonding systems, and metal ion sensing.

1.6. References

1. Ishikawa-Ankerhold, H. C., Ankerhold, R. & Drummen, G. P. C. Advanced Fluorescence Microscopy Techniques—FRAP, FLIP, FLAP, FRET and FLIM. *Molecules* **17,** 4047–4132 (2012).

2. Luo, G., Wang, M., Konigsberg, W. H. & Xie, X. S. Single-molecule and ensemble fluorescence assays for a functionally important conformational change in T7 DNA polymerase. *Proc. Natl. Acad. Sci. U. S. A.* **104,** 12610–5 (2007).

3. Cannon, B., Pan, C., Chen, L., Hadd, A. G. & Russell, R. A Dual-Mode Single-Molecule Fluorescence Assay for the Detection of Expanded CGG Repeats in Fragile X Syndrome. *Mol. Biotechnol.* **53,** 19–28 (2013).

4. Ince, R. & Narayanaswamy, R. Analysis of the performance of interferometry, surface plasmon resonance and luminescence as biosensors and chemosensors. *Anal. Chim. Acta* **569,** 1–20 (2006).

5. Nguyen, H. H., Park, J., Kang, S. & Kim, M. Surface Plasmon Resonance: A Versatile Technique for Biosensor Applications. *Sensors* **15,** 10481–10510 (2015).

6. Pesciotta, E. N., Bornhop, D. J. & Flowers, R. A. Back-scattering interferometry: A versatile platform for the study of free-solution versus surface-immobilized hybridization. *Chem. - An Asian J.* **6,** 70–73 (2011).

7. HOW DOES SURFACE PLASMON RESONANCE WORK? (2016). Available at: http://biosensingusa.com/technologies/surface-plasmon-resonance/surface-plasmon-resonance-work/. (Accessed: 28th June 2016)

8. Ghai, R., Falconer, R. J. & Collins, B. M. Applications of isothermal titration calorimetry in pure and applied research-survey of the literature from 2010. *J. Mol. Recognit.* **25,** 32–52 (2012).

9. Young, T. The Bakerian Lecture: Experiments and Calculations Relative to Physical Optics. *Philos. Trans. R. Soc. London* **94,** 1–16 (1804).

10. Darling, D. The Internet Encyclopedia of Science: Light. (2011). Available at: http://www.daviddarling.info/encyclopedia/L/light.html. (Accessed: 20th June 2012)

11. Hariharan, P. *Basics of Interferometry*. (Elsevier, 2010).

12.   Baldwin, J. E. & Haniff, C. A. The application of interferometry to optical astronomical imaging. *Philos. Trans. A. Math. Phys. Eng. Sci.* **360,** 969–86 (2002).

13.   Bruning, J. H. *et al.* Digital Wavefront Measuring Interferometer for Testing Optical Surfaces and Lenses. *Appl. Opt.* **13,** 2693 (1974).

14.   Goldstein, R. M. & Zebker, H. A. Interferometric radar measurement of ocean surface currents. *Nature* **328,** 707–709 (1987).

15.   Graber, H. C., Thompson, D. R. & Carande, R. E. Ocean surface features and currents measured with synthetic aperture radar interferometry and HF radar. *J. Geophys. Res. Ocean.* **101,** 25813–25832 (1996).

16.   Heideman, R. G., Kooyman, R. P. H. & Greve, J. Performance of a highly sensitive optical waveguide Mach-Zehnder interferometer immunosensor. *Sensors Actuators B Chem.* **10,** 209–217 (1993).

17.   Abbott, B. P. *et al.* Observation of Gravitational Waves from a Binary Black Hole Merger. *Phys. Rev. Lett.* **116,** 061102 (2016).

18.   Swinney, K. A. & Bornhop, D. J. Universal detection for capillary electrophoresis-using micro-interferometric backscatter detection. *J. Microcolumn Sep.* **11,** 596–604 (1999).

19.   Swinney, K. & Bornhop, D. J. A chip-scale universal detector for electrophoresis based on backscattering interferometry. *Analyst* **125,** 1713–1717 (2000).

20.   Kelly Swinney, Dmitry Markov, and & Bornhop*, D. J. Chip-Scale Universal Detection Based on Backscatter Interferometry. (2000).

21.   Pesciotta, E. N. Back-scattering Interferometry: A robust tool for the analysis of intermolecular interactions. (Lehigh, 2011).

22.   Kussrow, A. *et al.* The potential of backscattering interferometry as an in vitro clinical diagnostic tool for the serological diagnosis of infectious disease. *Analyst* **135,** 1535–7 (2010).

23.   *CRC Handbook of Chemistry and Physics*. (Chemical Rubber Publishing Company, 1996).

24.   Bornhop, D. J. *et al.* Free-solution, label-free molecular interactions studied by back-scattering interferometry. *Science* **317,** 1732–6 (2007).

25.   Molecular Sensing, Illuminating Biological Interactions. (2014). Available at: http://molsense.com/home-9/technology. (Accessed: 1st January 2014)

26.   Berg, J. M. *Biochemistry*. (WH Freeman, 2010).

27.   Moreira, B. G., You, Y., Behlke, M. A. & Owczarzy, R. Effects of fluorescent dyes, quenchers, and dangling ends on DNA duplex stability. *Biochem. Biophys. Res. Commun.* **327,** 473–484 (2005).

28.   Morrison, L. E. & Stols, L. M. Sensitive fluorescence-based thermodynamic and kinetic measurements of DNA hybridization in solution. *Biochemistry* **32,** 3095–104 (1993).

29.   Piunno, P. A. ., Watterson, J., Wust, C. C. & Krull, U. J. Considerations for the quantitative transduction of hybridization of immobilized DNA. *Anal. Chim. Acta* **400,** 73–89 (1999).

30.   Olmsted, I. R., Kussrow, A. & Bornhop, D. J. Comparison of free-solution and surface-immobilized molecular interactions using a single platform. *Anal. Chem.* **84,** 10817–22 (2012).

31.   Bornhop, D. J., Kammer, M. N., Kussrow, A., Flowers, R. A. & Meiler, J. Origin and prediction of free-solution interaction studies performed label-free. *Proc. Natl. Acad. Sci. U. S. A.* **113,** E1595–604 (2016).

32.   Sota, H., Hasegawa, Y. & Iwakura, M. Detection of Conformational Changes in an Immobilized Protein Using Surface Plasmon Resonance.

33.   Jason E. Gestwicki, †, Helen V. Hsieh, and & Pitner*, J. B. Using Receptor Conformational Change To Detect Low Molecular Weight Analytes by Surface Plasmon Resonance. (2001).

34.   Karlsson, R. Real-Time Competitive Kinetic Analysis of Interactions between Low-Molecular-Weight Ligands in Solution and Surface-Immobilized Receptors. *Anal. Biochem.* **221,** 142–151 (1994).

35.   Karlsson, R. *et al.* Biosensor Analysis of Drug–Target Interactions: Direct and Competitive Binding Assays for Investigation of Interactions between Thrombin and Thrombin Inhibitors. *Anal. Biochem.* **278,** 1–13 (2000).

36.   Rich, R. L. & Myszka, D. G. Survey of the year 2001 commercial optical biosensor literature. *J. Mol. Recognit.* **15,** 352–76

37.   Dell'Orco, D., Müller, M. & Koch, K.-W. Quantitative detection of conformational transitions in a calcium sensor protein by surface plasmon resonance. *Chem. Commun. (Camb).* **46,** 7316–8 (2010).

38.   Sulmann, S., Dell'Orco, D., Marino, V., Behnen, P. & Koch, K.-W. Conformational changes in calcium-sensor proteins under molecular crowding conditions. *Chemistry* **20,** 6756–62 (2014).

39.   Pesciotta, E. N., Bornhop, D. J. & Flowers, R. A. Backscattering interferometry: an alternative approach for the study of hydrogen bonding interactions in organic solvents. *Org Lett* **13,** 2654–2657 (2011).

40.   Young, S. *et al.* Peripheral site acetylcholinesterase inhibitors targeting both inflammation and cholinergic dysfunction. *Bioorg. Med. Chem. Lett.* **20,** 2987–2990 (2010).

Chapter 2

BSI as an ultrasensitive method for unperturbed detection of Acetylcholinesterase-Inhibitor interactions

2.1. Introduction

2.1.1. Acetylcholinesterase function and structure

Acetylcholinesterase (AChE) is a serine hydrolase enzyme that plays a vital role in neurotransmission, outlined in Figure 2.1. It is found in synapses of neurons and muscle cells (or other neurons), also known as a neuromuscular junction, and has one of the fastest reaction rates of animal enzymes. Its substrate is the neurotransmitter acetylcholine (ACh), which is hydrolyzed to acetate and choline at the active site of AChE to terminate signal transmission in both the peripheral and central nervous system. The hydrolyzed choline is then resynthesized to acetylcholine by choline acetyltransferase (ChAT) to continue signaling. ACh also serves as a neuromodulator within the brain to affect other functions and processes, including REM sleep.
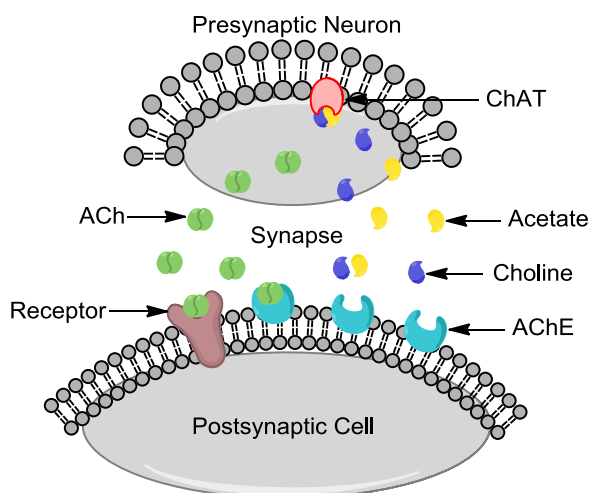
Figure 2.1. Acetylcholine's cycle as a neurotransmitter.

AChE's existence and function was first proposed over 100 years ago by Sir Henry Dale,[1] but its structure wasn't confirmed until 1991, when a form from torpedo ray fish was crystallized.[2] Electric fish like the torpedo provided a good source to study the enzyme thanks to high concentrations in the massive amounts of nerve-like structures in their electricity-generating organs.

The active site of AChE is located near the bottom of a 20 Å deep gorge, which features hydrophobic walls lined with 14 aromatic residues, and a catalytic triad of serine, histidine, and glutamate at the active site. This gorge reaches almost halfway through the enzyme. A second potential binding site, known as the peripheral anion site (PAS), is located at the top of the active site gorge. It consists of five residues: three tyrosine, one aspartic acid, and one tryptophan. Ten other acidic residues located in the surrounding area at the top of the gorge account for the overall negative charge of the region. These encompass a variety of modes for interacting with a ligand or inhibitor, including aromatic stacking and hydrogen bonds.[3]

AChE is an important therapeutic target for a variety of reasons, including disease prevention and combating chemical warfare. Toxic sulfur agents or organophosphates act as potent inhibitors of the active site and disrupt neurotransmission, causing inflammation and muscle over-stimulation due to the inhibited AChE's inability to break down ACh, which results in ACh accumulation at receptors. In neurodegenerative diseases such as Alzheimer's disease (AD), reduced ChAT activity and cholinergic neurotransmission are major factors believed to affect cognitive impairment.
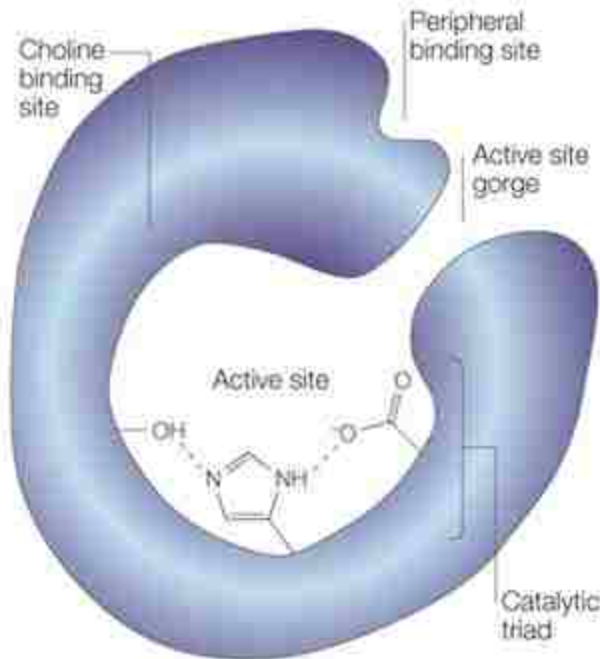
Figure 2.2. Diagram of AChE, indicating the active site in the gorge and the peripheral site near the top of the gorge.[4]

2.1.2. The Cholinergic hypothesis of Alzheimer's disease

Alzheimer's disease is a progressive neurodegenerative disease characterized by cognitive impairment and memory loss. It is the most common form of dementia in elderly people, affecting nearly 50 million people worldwide. The cholinergic hypothesis of the disease was first developed in the 1970's when the role of ACh in memory was being studied and decreased levels of ACh production in patients' brains were first observed.[5] It proposed that two of the main pathological markers of the disease, buildup of intracellular tau protein tangles and extracellular β-amyloid plaques, are a result of deficiencies in cholinergic neurotransmission. Therefore the progressive nature of the disease is due to the loss of neurons that use ACh as the main neurotransmitter in certain parts of the brain (basal forebrain) and lowered ACh

transmission in other parts (hippocampus and cerebral cortex); in order to alleviate symptoms, it would be necessary to restore ACh to higher levels seen in healthy brains.

Beta amyloid (Aβ) fibrils in extracellular regions are the precurors to the plaques observed in the brains of Alzheimer's patients. They are formed when the amyloid precursor protein (APP) is not cleaved correctly. Their formation as a cause of the disease, rather than a symptom of lowered ACh as described in the cholinergic hypothesis, was initially described as part of an "amyloid hypothesis" of AD. While the formation of plaques serving as a symptom versus a cause of the disease is still debated, the PAS of AChE has been shown to play a role in Aβ deposition.[3,6] Increased aggregation of the fibrils accelerates the formation of the plaques, and the PAS mediates and accelerates fibril aggregation by inducing beta-sheet conformational changes in the amyloids. Thus, the first AChE inhibitors (AChEIs) were designed to combat the symptoms of AD and restore cognitive functions by increasing ACh levels in the brain, i.e. inhibitors would prevent AChE from hydrolyzing ACh, while later AChEIs have been designed to also target the PAS in an attempt to block the aggregation of Aβ fibrils.[7,8]

2.1.3. Acetylcholinesterase Inhibitors

Several inhibitors of AChE exist on the market, encompassing a wide variety of inhibition mechanisms, whose functions and binding targets determine their purposes. Tacrine was the first inhibitor approved for treatment of AD in 1993, though it only ever produced modest results in restoring cognitive ability, caused potentially serious side effects including seizures and cardiovascular issues, and was discontinued in the US in 2013. It and donepezil, the second AChEI on the market, both functioned as mixed inhibitors of AChE, with slight affinity for both the active and peripheral sites of the

enzyme (donepezil was more selective and potent).[7] Since then, several other AChEIs were introduced to the market to combat the symptoms of AD. Edrophonium is a reversible competitive inhibitor that was used in the past to test for myasthenia gravis, a neuromuscular disease. The carbamates, pseudo-irreversible competitive inhibitors, including Physostigmine and derivatives Neostigmine and Rivastigmine, are cleaved and covalently modify the enzyme at the active site serine, but are slower compared to other inhibitors.[9] Galantamine is another mixed inhibitor first industrially isolated as natural product from snowdrop flowers in the 1950s. Propidium, a noncompetitive inhibitor with affinity solely for the PAS, is also used to treat Alzheimer's disease. The discovery of the role of the PAS in Aβ aggregation made noncompetitive inhibitors such as propidium desirable targets.

Structure-activity relationship (SAR) studies have determined appropriate linkers and molecule lengths for mixed inhibitors, such as BW284c51, to target both the active and peripheral site.[10] In the case of potential anti-Alzheimer's drugs, targeting of the PAS is preferred in order to prevent the deposition of the Aβ fibrils that lead to plaque formation. Thus, any drugs designed for these purposes tend to be noncompetitive inhibitors, such as propidium, or mixed inhibitors to target both the cholinergic hypothesis and amyloid hypothesis causes of the disease.

Despite the availability of these AChE inhibitors, there exists a need for improved treatment options for a variety of reasons. Typically patients taking donepezil, galantamine, or rivastigmine see improvement in cognitive abilities only temporarily, up to a year, before worsening again.[11] Additionally, many of these inhibitors were designed to target the active site, with the role of the PAS in disease progression being a more

recent discovery, so better targeting of the PAS site would be desirable, either as solely noncompetitive inhibitors, or dual-binding inhibitors with high affinity for both sites. Finally, in addition to the need for new AChE inhibitors, a rapid, straightforward method to screen potential inhibitors would provide a great advantage to AChEI research, as well.

2.1.4. Methods to determine inhibition activity

One common method for determining the effectiveness of a potential inhibitor of AChE is the use of Ellman's Assay to determine IC_{50} values, or the half maximal inhibitory concentration, for each potential inhibitor. The IC_{50} values define the concentration of the inhibitor required to inhibit 50% of the target's normal activity. Ellman's Assay is a colorimetric assay developed in 1961 to measure inhibition of AChE by quantifying the absorbance of the hydrolyzed product of Ellman's reagent, dithionitrobenzoic acid (DTNB).[12] The procedure, shown in Scheme 2.1, begins with AChE, the potential inhibitor, and acetothiocholine (ATCh), a derivative of the natural ACh substrate. Upon interaction with the enzyme, ATCh is hydrolyzed to its thiol form, which can then attack the S-S bond of DTNB. Cleavage of this bridging sulfur bond yields 2-nitro-5-thiobenzoate ion, which, in basic media, ionizes again to the dianion (TNB^{2-}) and results in a yellow solution. The reaction is stoichiometric, and the absorbance change based on the colored dianion product is measured.
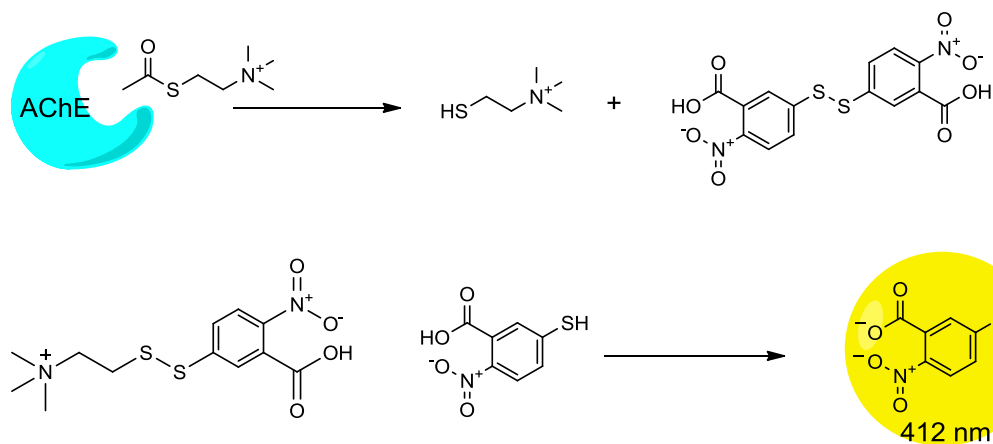
Scheme 2.1. Ellman's Assay.

This assay is an indirect measurement of substrate inhibition through determination of the absorbance of the cleaved Ellman's reagent at 412 nm. The concentration of the reagent is then determined via Beer's Law, which is related stoichiometrically to the amount of substrate hydrolyzed by the enzyme. Thus, a stronger inhibitor would result in a lower concentration of colored reagent, as less ATCh would have been initially hydrolyzed by AChE. This procedure is less effective for screening inhibitors of the PAS, and is prone to false positives in the presence of strong nucleophiles, such as oximes, which have been used as antidotes to reactivate AChE that has been inhibited by organophosphate poisoning. In these instances, the nucleophilic oxime could hydrolyze ATCh, instead of AChE hydrolyzing it, and result in an erroneously high concentration of the cleaved and colored TNB^{2-}, making a potential inhibitor seem less effective than it actually is. Sakurada and coworkers discovered this effect in 2006, decades after Ellman's Assay had been developed, when they measured reactivation of AChE with increasing amounts of pralidoxime iodide (2-PAM) via this assay, and noticed activity levels beyond the negative controls. This study stressed the

need for careful analyses in activity studies, and a major potential drawback of using indirect measurements or derivatives of natural substrates.[13]

To circumvent these false positives, other methods of AChE inhibitor measurements have been developed. Ideally, experiments would either use the natural ACh as a substrate, or require no substrate at all. Many are fluorescent or chemiluminescent assays, including dioxetane-disulfide derivatives of Ellman's Reagent,[14] cascading fluorescence 'turn-on' reactions,[15] or larger molecular probes including fullerene derivatives.[16] These typically require time-consuming and laborious procedures, but have produced some of the lowest limits of detection available, down to 0.1 fM in the case of some dioxetane chemiluminescent probes.[17]

2.1.5. BSI as a desirable platform for enzyme inhibitor screening

As discussed previously in Chapter 1, the presence of fluorophores can perturb binding, so for a true measurement of native binding strength, label-free detection methods at relevant physiological conditions are preferred. BSI appears to be a desirable platform for these types of inhibition studies, as experiments are performed label-free at low concentrations, and in free solution. The straightforward procedure and sample preparation allow the screening of a variety of different inhibitors. Additionally, for enzymes such as AChE which can cost hundreds or even thousands of dollars per mg, BSI's small sample size, with a probe volume of less than 400 pL for the original chips used in this study (7.52 nL in the present chips with wider channels), offers an advantage as well. Another advantage is that BSI measurements are a direct measurement of the inhibitor interacting with the enzyme with no substrate (ACh or ATCh) present. Thus,

experiments were designed to measure inhibition K_D values (or K_i's) of potential inhibitors of AChE via BSI.

The goal of this study was to compare and benchmark K_i's determined with BSI to 1) previously determined K_i values of known AChE inhibitors determined by a variety of fluorescent assays, and 2) previously determined IC_{50} values of novel AChE inhibitors via Ellman's assay. With these results we sought to show that inhibitor affinities determined with BSI correlated well with those determined by Ellman's assay and other methods, showing that BSI would be a more preferred approach for inhibition studies due to its many advantages, including being performed label-free, in free solution, substrate free, and at physiological conditions and low concentrations without laborious procedures. Finally, BSI experiments would allow for potential new anti-Alzheimer's agents to be discovered and screened more rapidly.

2.2. Materials and Methods

2.2.1. Instrument and chip channel preparation

The instrument (detector/computer, laser, and temperature-controller) was equilibrated at least one hour prior to experiments. The stage containing the microfluidic chip was held at a constant 25 °C.

The microfluidic chip used for these experiments contained three channels that were 90 μm in diameter. For each experiment, the channels were silanized with 3-mercaptopropyltriethoxysilane (MEPTES) to prevent nonspecific interactions with the walls (Figure 2.3). This procedure involved an initial hour soak in concentrated H_2SO_4 in order to fully clean any remaining materials or residues in the channel, followed by a half hour soak with a 10% KOH/MeOH solution, refilled every eight to ten minutes to prevent

drying and clogging. This was followed by a rinse with water and methanol. Next, an

hour-long soak of the silanizing agent, MEPTES (2% in toluene) was performed, with

refills every 15 min to prevent drying. This was again followed by toluene, methanol, and

water rinses. After all channels within the chip were used, chips were rinsed with water,

sonicated for 30-60 min, and resilanized. Clogs could be cleared by rinses with

concentrated HNO_3 (soaks with nitric acid lasted no more than 5 min), and additional

sonication and rinsing with water. The narrower channels were more prone to clogs,

typically due to precipitation from the nearly-saturated KOH/MeOH solution, than the

newer, 210 μm diameter channels used in later projects.
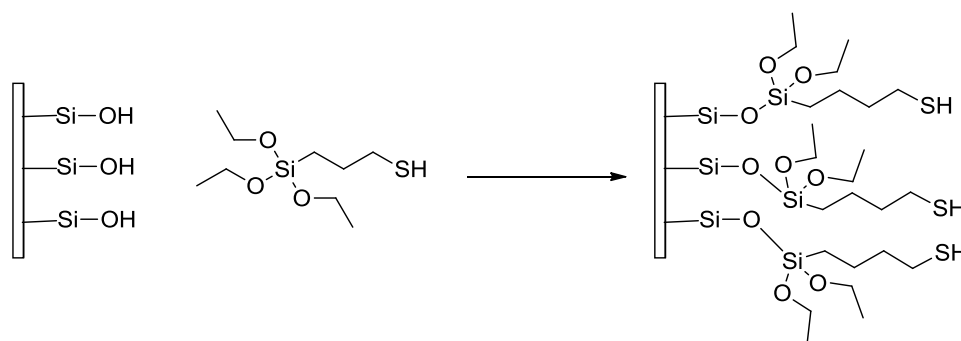
Figure 2.3. Silanization of channel walls with MEPTES to avoid nonspecific interactions
of hydrophilic analytes with the wall.
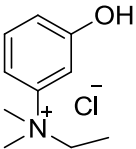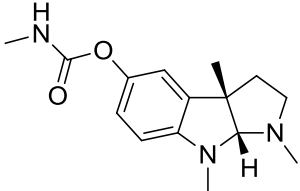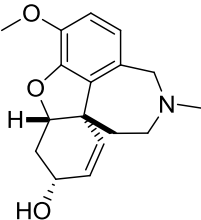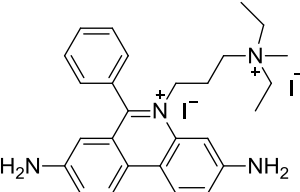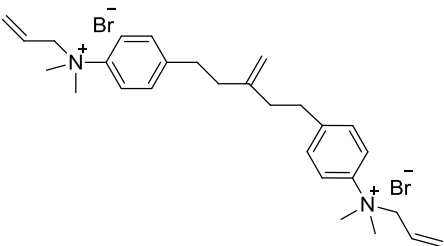
2.2.2. Preparation of samples

The Heindel research group has produced a variety of potential inhibitors of

AChE through various SAR studies.[18] While many of these have applications for anti-

inflammatory purposes, depending on their preferred targeted site and inhibition

mechanism, some were also considered suitable for potential anti-Alzheimer's agents.

Six of these novel inhibitors were the inhibitors selected for the present study.

Additionally, five known and commercially-available inhibitors were used in order to
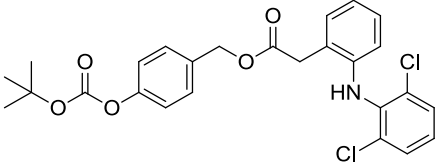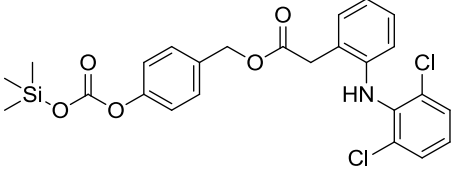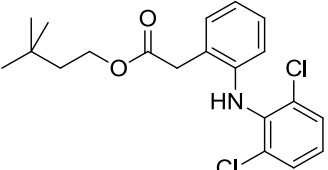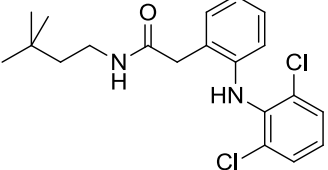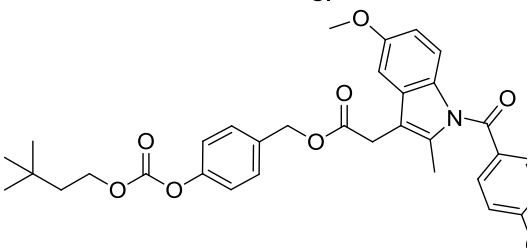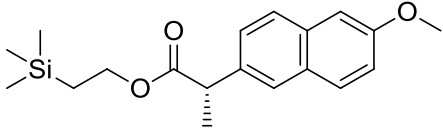
benchmark the BSI experiments. Table 2.1 lists information for the known inhibitors, and Table 2.2 lists information for the novel inhibitors. The novel inhibitors were prepared as previously described.[18] The phosphate-buffered saline (PBS), and any cosolvent, was filtered with 0.2 μm membrane filters before use. AChE, from Sigma-Aldrich, was dialyzed against PBS (3 x 300 mL) using regenerated cellulose dialysis tubing (weight cutoff 3500 Da), and portions were frozen to be stored for use as needed.

Cosolvents (10% MeOH, or 5% DMSO or 2(2-ethoxyethoxy)ethanol) were used to increase the solubility of the novel inhibitors due to their high lipophilicity. Initially concerns over using MeOH as a cosolvent due to its higher volatility influenced us to switch to the other cosolvents at lower amounts, but these experiments showed no significant improvements to errors in the experiments. Therefore MeOH as a cosolvent in PBS was used and collection times were shortened by 15-20 seconds to account for the faster evaporation time, which causes greater amounts of error and drift in the BSI signal.

Table 2.1. Known inhibitors used for BSI experiments in PBS.

Ligand	Structure	Conc. Range (μM)	[AChE] (μM)
Edrophonium		0-8.0	1.4
Physostigmine		0-2.5	0.36
Galantamine		0-5.0	0.18
Propidium		0-10.0	0.72
BW284c51		0-100 nM	72 nM

Table 2.2. Novel inhibitors used for BSI experiments in PBS:MeOH (9:1)

Ligand	Structure	Conc. Range (μM)	[AChE] (μM)
1		0-1.0	0.0072
2		0-6.0	0.36
3		0-12.0	1.4
4		0-3.0	6.9
5		0-6.0	1.4
6		0-3.0	2.5

To ensure the concentration of AChE was not too high to cause aggregation, [AChE] was held constant below 6.9 μM while increasing concentrations of the inhibitors were added to each sample. The concentrations of the inhibitors used were based on IC_{50} values determined with Ellman's method (for the novel inhibitors) or with previously published K_i's (for the known inhibitors).[19–26] Samples were allowed to equilibrate at 4 °C for at least 3 hours before use. Enzyme and ligand blanks were prepared to account for any concentration-dependent signal changes above the noise that would need to be subtracted out, however, the ligand blanks did not result in a readable signal above the noise level of the instrument. Samples were kept covered and over ice during experiments to ensure stability.

2.2.3. Data collection

Water followed by PBS buffer (or PBS:MeOH mixed solvent) were first pipetted into the channel to ensure a stable and repeatable signal. Next, blanks containing only inhibitor were run in order to subtract out any concentration-dependent signals above the noise level, however, the ligands on their own did not produce a readable signal at the concentrations used. The sample containing only buffer and AChE was the initial 'zero point,' which was subtracted from each subsequent point (samples containing enzyme and inhibitor) to normalize the binding curve to a constant baseline. After each injection, data was collected for approximately 45-60 seconds, to avoid any initial baseline disruption immediately following injection and ensure equilibration in the channel. Shorter collection times were used for samples containing a cosolvent of 10% MeOH to avoid evaporation of the sample solution in the channel, which results in spurious and drifting signals.

2.2.4. Data Analysis

Binding curves were plotted as a function of phase shift versus inhibitor concentration in Excel, and K_i values were calculated using the one-site binding hyperbola equation in GraphPad Prism and Excel. Each point in the curve was based on the average signal of each sample, with typically 5-10 trials collected over two or three days. Error bars are based on the standard deviation of each concentration point, and error in the K_i was propagated from each point.

2.3. Results & Discussion

2.3.1. Benchmarking of BSI results to previous results of known inhibitors

The known inhibitors in this study encompassed a wide range of affinities and various types of inhibition mechanisms. Edrophonium is a competitive inhibitor, propidium is a noncompetitive inhibitor, galantamine and BW284c51 are mixed inhibitors, and physostigmine is a pseudo-irreversible carbamate (mixed) inhibitor. These inhibitors each interact differently with AChE, but each resulted in a single rise-to-max binding curve increasing in the positive direction at varying magnitudes. K_i values determined using BSI correlated well with previously determined K_i's determined by a variety of techniques, summarized in Table 2.3. Each individual binding curve is represented in Figures 2.4—2.8, and each point on the curves are the result of five or more trials over two or more days.
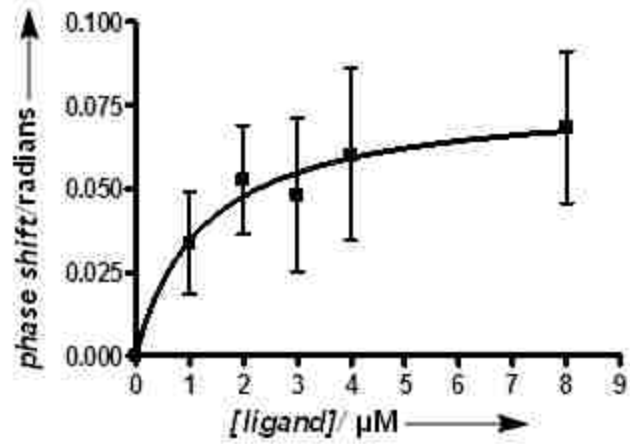
Figure 2.4. BSI binding curve of AChE (1.4 µM) with edrophonium in PBS.
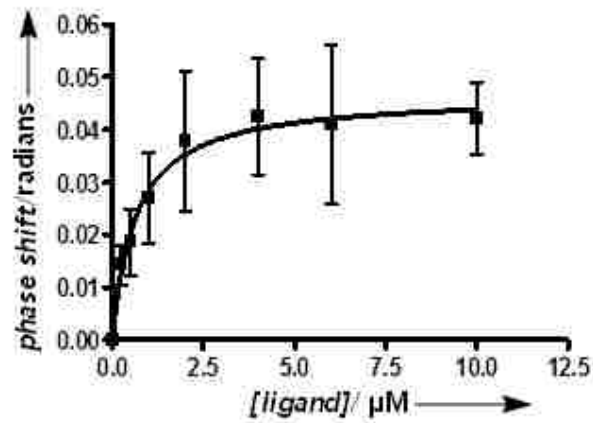
Figure 2.5. BSI binding curve of AChE (0.72 µM) with propidium in PBS.
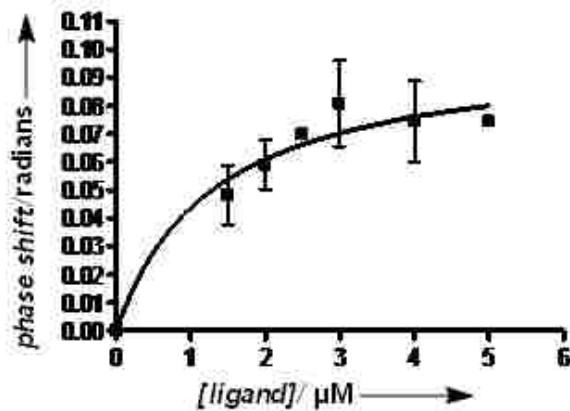
Figure 2.6. BSI binding curve of AChE (0.18 µM) and galantamine in PBS.
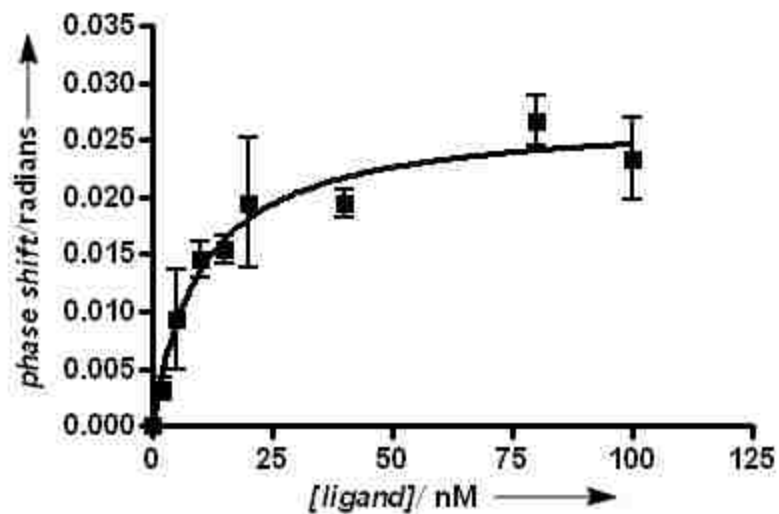
Figure 2.7. BSI binding curve of AChE (72 nM) and BW284c51 in PBS.
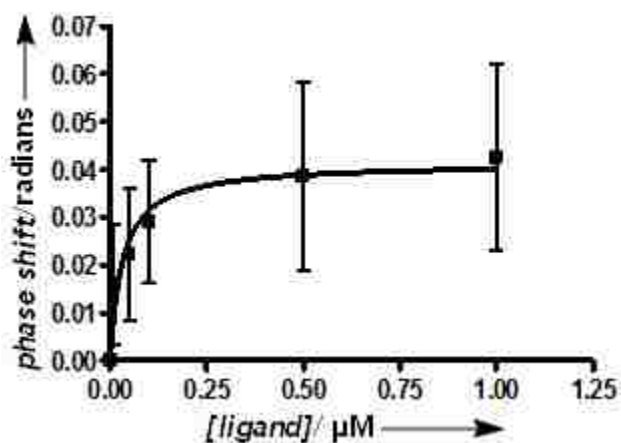
Figure 2.8. BSI binding curve of AChE (0.36 μM) and physostigmine in PBS.

Table 2.3. Comparison of BSI K_D/K_i values to literature K_D values.

Inhibitor	BSI K_D (μM)	Literature K_D (μM)	Ref.
Edrophonium	1.27 ± 0.4	1.5-3.8	[19,20]
Physostigmine	0.020 ± 0.009	0.013-0.11	[21,22]
Galantamine	1.23 ± 0.5	0.20-0.61	[23]
Propidium	0.64 ± 0.09	0.63-1.5	[19,24]
BW284c51	8.4 ± 2.0 nM	3.2-8.0 nM	[26,27]

All inhibitors produced a binding curve in the positive direction at similar magnitude, with a maximum signal, or RI shift, between 0.03-0.08 radians. The signal is believed to be a result of conformation, solvation, and polarizability changes as the inhibitor binds to the enzyme.

2.3.2. Comparison of BSI results to Ellman's assay results of novel inhibitors

As BSI experiments using novel AChE inhibitors continued, expected similar results to the known inhibitors were expected. However, comparison of the BSI K_i values of the novel inhibitors to the IC_{50} values determined via Ellman's assay showed quite different results, as summarized in Table 2.4. Figures 2.9-2.12 show the BSI binding curves for each ligand.
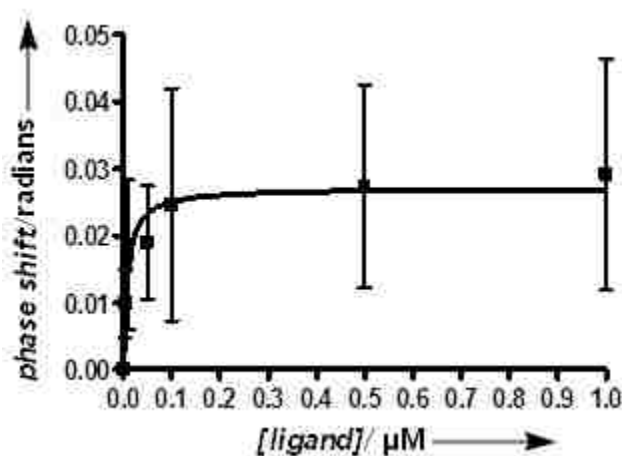
Figure 2.9. BSI binding curve of AChE (7.2 nM) and Ligand 1 in 9:1 PBS:MeOH.
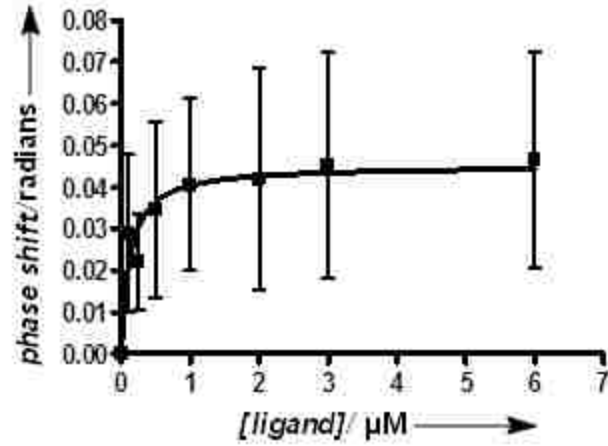
Figure 2.10. BSI binding curve of AChE (0.36 μM) and Ligand 2 in 9:1 PBS:MeOH.
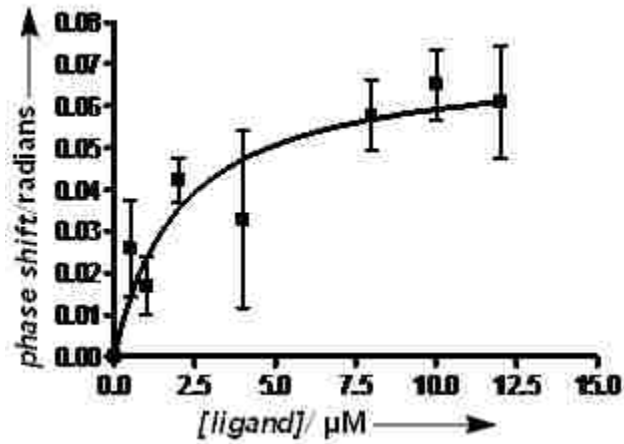
Figure 2.11. BSI binding curve of AChE (1.4 μM) and Ligand 3 in 9:1 PBS:MeOH.
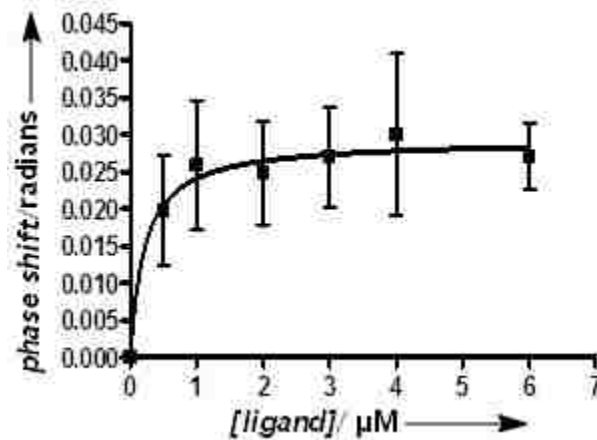
Figure 2.12. BSI binding curve of AChE (1.4 μM) and Ligand 5 in 9:1 PBS:MeOH.

61

Table 2.4. BSI K_i/K_D values compared to Ellman IC$_{50}$ values.

Ligand	BSI K_D (µM)	Ellman IC$_{50}$ (µM)[18]
1	0.11 ± 0.05	0.51 ± 0.02
2	0.21 ± 0.05	1.36 ± 0.1
3	2.18 ± 1.1	2.69 ± 0.1
4	*dual-binding*	6.34 ± 0.5
5	0.12 ± 0.04	2.29 ± 0.9
6	*dual-binding*	13.9 ± 0.3

Only one inhibitor in this study had a K_i that matched its IC$_{50}$. While differences between IC$_{50}$ and K_i determinations have been reported, these were typically due to experimental conditions when determining IC$_{50}$, such as the concentration of substrate or the temperature or pH of the assay, or for more complex inhibition mechanisms or enzymes with two substrates. In such instances, differences of up to two orders of magnitude or more have been observed.[28] On the other hand, K_i values are intrinsic properties independent of assay conditions. The differences between these novel inhibitors' IC$_{50}$ and K_i values were initially puzzling, but can be explained with the Cheng-Prusoff relationship (Scheme 2.2), which describes the differences between the systems being probed with both techniques (BSI and Ellman test).[29] It describes that, for noncompetitive or mixed inhibition pathways and a high concentration of substrate (like in conditions for the Ellman assay), the IC$_{50}$ is equal to the inhibitor's affinity for the enzyme-substrate complex, which could be denoted as a K_{ies}. With no substrate present, the affinity of the inhibitor is for the enzyme only, or a K_{ie}.

$$I + E \cdot S \rightleftharpoons I + E \cdot S \longrightarrow E + P$$

K_{ie}
BSI ([S]=0)

K_{ies}
IC$_{50}$ (high [S])

E · I   E·S·I
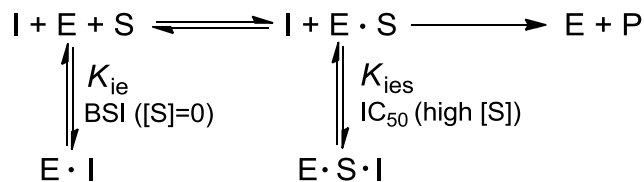
Scheme 2.2. The Cheng-Prusoff relationship describes the relationship between the BSI K_D (or in this case, K_i) and IC$_{50}$ determined via Ellman's Assay.

The Cheng-Prusoff relationship highlights that the equilibria being measured with BSI and with Ellman's assay are not the same due to the presence or absence of substrate (acetylcholine or a derivative), thus, the relationship between IC$_{50}$ and K_i can vary. In BSI experiments, with no substrate present, the dissociation constant being measured is between the enzyme and inhibitor only, and the active site is available. Conversely, with a high concentration of substrate (as in Ellman's assay), the equilibrium exists between the inhibitor and the enzyme-substrate complex, and the active site is occupied by the substrate. Whether the inhibitor behaves differently between the enzyme and the enzyme-substrate complex depends on the inhibition mechanism; since BSI experiments measure the affinity of the enzyme alone (no substrate present) and experiments using Ellman's assay measure the affinity of the enzyme-substrate complex, comparisons of these values yields insight into the inhibitors' inhibition mechanisms.

Upon reexamination of the results, it was concluded that, in instances where the K_i is equal to the IC$_{50}$ (within experimental error), as is the case with ligand 3, the inhibitor's affinity for the enzyme is the same regardless of the presence of substrate (K_{ie} = K_{ies} = K_i); this means the ligand has affinity for the peripheral site alone, and acts as a noncompetitive inhibitor. In cases where the K_i is significantly lower than the IC$_{50}$, namely ligands 1,2, and 5, it indicates that these ligands have affinity for the active site in

63

addition to any peripheral site affinity, and act either as competitive or mixed inhibitors, with affinity for both sites. In the BSI system with no substrate present, they are able to bind to the active site, and have a greater affinity overall to the enzyme, resulting in a lower K_i value. These differences between IC_{50} and K_i can also be described mathematically from the Michaelis-Menton equation (1) based on the type of inhibition.

$$V_0 = \frac{V_{max}[S]}{K_m+[S]} \tag{1}$$

In the Michaelis-Menton equation, V_0 is the velocity of the enzyme-substrate interactions, V_{max} is the maximum velocity, $[S]$ is the concentration of substrate, and K_m is the Michaelis constant. A competitive inhibitor has affinity solely for the active site, i.e. the enzyme and not the enzyme-substrate complex. Competitive inhibition alters the kinetics of the enzyme-substrate complex by increasing the apparent K_m of the system, which decreases the velocity, as shown in Equation 2.

$$V_I = \frac{V_{max}[S]}{K_m+(1+\frac{[I]}{K_i})+[S]} \tag{2}$$

Here, V_I is the velocity with inhibitor present at a concentration $[I]$, and K_i is the inhibitory dissociation constant. When $[I] = IC_{50}$, the velocity is half of V_0, and Cheng and Prusoff demonstrated how the above equation can be rearranged to Equation 3 to show the relationship between the IC_{50} and K_i of a given enzyme-competitive inhibitor system.[29]

$$IC_{50} = K_i(1 + \frac{[S]}{K_m}) \tag{3}$$

For noncompetitive inhibition, V_{max} is reduced but K_m does not change, so the Michaelis-Menton equation takes into account the apparent V_{max} as shown in Equation 4.

64

The inhibitor has the same affinity for both the enzyme itself and the enzyme-substrate complex ($K_{ie} = K_{ies} = K_i$)

$$V_I = \frac{V_{max}[S]}{K_m\left(1+\frac{IC_{50}}{K_i}\right)+[S](1+\frac{IC_{50}}{K_i})}$$

(4)

When $[I] = IC_{50}$, $V_0 = 2V_I$, and the equation can be simplified to $IC_{50} = K_i$.[29]

The results from comparing BSI K_i values to the IC_{50} values make it possible to distinguish between a true noncompetitive inhibitor and competitive or mixed inhibitors, but not necessarily between a competitive inhibitor and a mixed inhibitor. The two remaining ligands featured different results that may also yield some insight into their affinity for AChE.
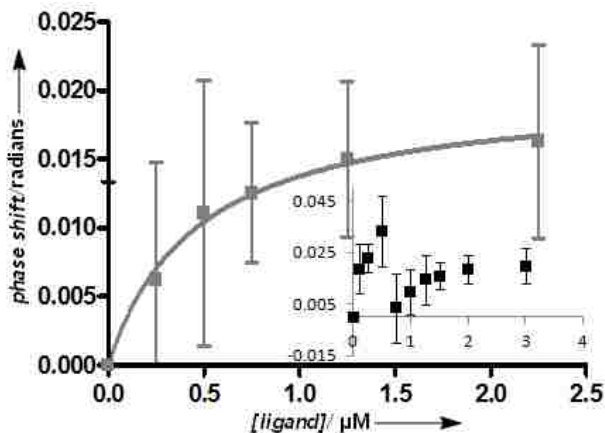
Figure 2.13. BSI binding curve of AChE (6.9 µM) and Ligand 4 in 9:1 PBS:MeOH; the inset shows the two separate binding events, and the larger plot shows the fit to an isolated second binding event.
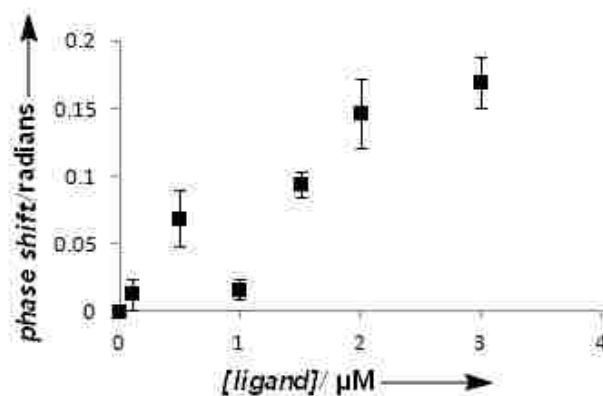
Figure 2.14. BSI binding curve of AChE (2.5 µM) and Ligand 6 in 9:1 PBS:MeOH, featuring two separate rise-to-max events.

In the case of the remaining two ligands (4 and 6), two separate rise-to-max binding curves were observed upon increasing inhibitor concentration, where the signal increased up to a certain point then reversed back near the initial starting phase baseline, before continuing to increase as what appeared to be a second binding event. These binding curves are shown in Figures 2.13 and 2.14. It was difficult to calculate a K_i for these ligands (For Ligand 4, zeroing the second binding curve and treating it as an isolated event yields a K_i of 0.97 ± 0.57 µM), but these results give interesting insights into the inhibitors' behavior nonetheless. It seems these inhibitors can also act as a type of mixed inhibitor, with affinity for both the active and peripheral site, and subsequent binding induces changes to the system that register as a different change in signal for the BSI. In the case of AChE, this could be a result of solvent molecules being expelled from the active site gorge and a subsequent conformational change to allow for the inhibitors to access both sites.[30–32]

BSI provides valuable insight into inhibition mechanisms when directly compared with results obtained via the Ellman method. The Cheng-Prusoff equation highlights the

relationship between the enzyme and the enzyme-substrate complex with a given inhibitor, as well as the differences in the equilibria being measured by each technique. Specifically, BSI is able to distinguish between mixed or competitive inhibition mechanisms and true noncompetitive binding. This is vitally important for potential Alzehimer's disease inhibitor research, as AChE inhibitors designed as anti-Alzheimer's agents would preferentially target the PAS in a noncompetitive manner. Competitive inhibitors, such as edrophonium, which selectively target the active site, showed no signs of suppressing the enzyme-induced Aβ aggregation. Most mixed inhibitors provide only moderate results at best, typically less than 30% suppression.[10,33] On the other hand, propidium, one of the true PAS-specific inhibitors, can suppress aggregation by up to 82%.[33] In addition to identifying inhibitors capable of targeting the PAS in order to prevent Aβ aggregation, BSI would also make it easier to screen subsequent inhibitors to act as potent mixed inhibitors that also target the active site to restore cholinergic activity.

2.3.3. Determination of the limit of detection

We next sought to determine the limit of detection when using BSI to detect inhibition of AChE. In order to measure this, we used the known inhibitor BW284c51, which had the highest affinity (lowest K_i) for AChE of the inhibitors used in this study. At the lowest limit with a readable signal, concentrations of 100 pM of enzyme could be detected. When taking the probe volume of the instrument into account, which for the channels used was about 360 pL, this equates to an astonishing limit of 23,000 molecules. This limit meets or exceeds a variety of techniques' limits of detection, all of which require complex probes or fluorophores,[15,17,34,35] while still being a result of a label-free and free-solution technique that avoids these costly procedures.

2.4. Conclusions

The results presented in this chapter demonstrate the many advantages BSI offers for analyzing enzyme-inhibitor interactions, including 1) low-volume and low-concentration samples, yielding more cost-effective experiments with less waste, 2) free-solution and label-free experiments that provide a LOD comparable to more complex fluorescent, colorimetric, and electrochemical techniques, 3) the ability to directly measure the K_i of enzyme inhibition systems and thus avoid false positive signals, and 4) the ability to gain insight into the types of inhibition mechanism by which an inhibitor operates, which is accomplished by comparing the BSI results to data obtained using systems that examine the enzyme-substrate complex, such as Ellman's assay. The technique is not without its drawbacks, however. When designing experiments with novel inhibitors or receptors, where less information on the characterization and interactions of the system is available, care must be taken to avoid too high concentrations, as this could cause either aggregation of the substances, or result in product complex concentrations where the mass-dependent RI changes overshadow the signal changes from the actual binding event. Additionally, cosolvents may be necessary for ligand solubility, but greater amounts of more volatile solvents increase the likelihood of solution evaporation in the channel. Solvent selection is also dependent on its index of refraction, which must not be too close to that of the microfluidic chip to ensure quality high-contrast fringes are generated.

The main advantage highlighted in this specific study is the ability to gain insight into an inhibitor's mechanism of action by comparing the BSI results to other techniques' results. This is especially important for potential anti-Alzheimer's agents, where

noncompetitive inhibitors are necessary to be most effective. BSI's small sample size can continue to aid in this field of research, where, for instance, it may be possible to further analyze inhibitor affinity for each site individually by using modified versions of the enzyme to 'shut down' one site, and specifically measure binding to the other. In a similar vein, studies with Butyrylcholinesterase (BChE), a similar enzyme but which lacks the peripheral site, could be performed with near-identical procedures to test inhibitor affinity for the active site separate from the PAS. The small sample sizes would allow for cost-effective amounts of both native and modified forms of the enzymes to be prepared.

Finally the procedures used for this study could also be applied to other enzyme inhibition systems, including orphan receptors. These receptors are usually structurally similar to known receptors, however they have no known endogenous ligand, such as acetylcholine to AChE. Thus, their natural function remains unknown. For example, G-protein coupled receptors (GPCRs) are a large and diverse class of proteins that participate in a wide array of natural functions, including many types of signal transductions. They are also some of the most successful targets of pharmaceuticals, but over 100 human GPCRs still have no identified natural ligand.[36] Combining computational library screening with screening experiments via BSI would allow for an efficient method to identify potential receptors and targets, and from there, potential medicinal uses. Similar screening studies could be performed with known receptors, as well, for expanded SAR studies of potential ligands or inhibitors.

2.5. References

1.   Dale, H. H. The action of certain Esters and Ethers of Choline, and their relation to Muscarine. *J. Pharmacol. Exp. Ther.* **6,** 147–190 (1914).

2.   Sussman, J. L. *et al.* atomic structure of acetylcholinesterase from Torpedo californica: a prototypic acetylcholine-binding protein. *Science (80-.).* **253,** 872–879 (1991).

3.   Johnson, G. & Moore, S. W. The peripheral anionic site of acetylcholinesterase: structure, functions and potential role in rational drug design. *Curr. Pharm. Des.* **12,** 217–225 (2006).

4.   Soreq, H. & Seidman, S. Acetylcholinesterase |[mdash]| new roles for an oldactor. *Nat. Rev. Neurosci.* **2,** 294–302 (2001).

5.   Drachman, D. A. Human Memory and the Cholinergic System. *Arch. Neurol.* **30,** 113 (1974).

6.   Inestrosa, N. C. *et al.* Acetylcholinesterase accelerates assembly of amyloid-β-peptides into Alzheimer's fibrils: Possible role of the peripheral site of the enzyme. *Neuron* **16,** 881–891 (1996).

7.   Francis, P. T., Palmer, A. M., Snape, M. & Wilcock, G. K. The cholinergic hypothesis of Alzheimer's disease: a review of progress. *J. Neurol. Neurosurg. Psychiatry* **66,** 137–147 (1999).

8.   Martorana, A., Esposito, Z. & Koch, G. Beyond the Cholinergic Hypothesis: Do Current Drugs Work in Alzheimer's Disease? *CNS Neurosci. Ther.* **16,** no–no (2010).

9.   Triggle, D. J., Mitchell, J. M. & Filler, R. The Pharmacology of Physostigmine. *CNS Drug Rev.* **4,** 87–136 (1998).

10.   Tumiatti, V. *et al.* Structure-activity relationships of acetylcholinesterase noncovalent inhibitors based on a polyamine backbone. 3. Effect of replacing the inner polymethylene chain with cyclic moieties. *J. Med. Chem.* **47,** 6490–6498 (2004).

11.   Drug treatments for Alzheimer's disease. Available at: https://www.alzheimers.org.uk/site/scripts/documents_info.php?documentID=147. (Accessed: 20th February 2016)

12.   Ellman, G. L. Tissue sulfhydryl groups. *Arch. Biochem. Biophys.* **82,** 70–77 (1959).

13.   Sakurada, K., Ikegaya, H., Ohta, H., Akutsu, T. & Takatori, T. Hydrolysis of an acetylthiocholine by pralidoxime iodide (2-PAM). *Toxicol. Lett.* **166,** 255–260 (2006).

14.   Maeda, H. *et al.* 2,4-Dinitrobenzenesulfonyl fluoresceins as fluorescent alternatives to Ellman's reagent in thiol-quantification enzyme assays. *Angew. Chemie - Int. Ed.* **44,** 2922–2925 (2005).

15.   Peng, L. *et al.* A fluorescence 'turn-on' ensemble for acetylcholinesterase activity assay and inhibitor screening. *Org. Lett.* **11,** 4014–4017 (2009).

16.   Pastorin, G. *et al.* Design and activity of cationic fullerene derivatives as inhibitors of acetylcholinesterase. *Org. Biomol. Chem.* **4,** 2556–62 (2006).

17.   Sabelle, S. *et al.* Design and synthesis of chemiluminescent probes for the detection of cholinesterase activity. *J. Am. Chem. Soc.* **124,** 4874–4880 (2002).

18.   Young, S. *et al.* Peripheral site acetylcholinesterase inhibitors targeting both inflammation and cholinergic dysfunction. *Bioorg. Med. Chem. Lett.* **20,** 2987–2990 (2010).

19.   Shafferman, A. *et al.* Substrate inhibition of acetylcholinesterase: residues affecting signal transduction from the surface to the catalytic center. *EMBO J.* **11,** 3561–8 (1992).

20.   Schalk, I. *et al.* 6-Coumarin diazonium salt: A specific affinity label of the Torpedo acetylcholinesterase peripheral site. *Mol. Pharmacol.* **48,** 1063–1067 (1995).

21.   Bartolini, M., Cavrini, V. & Andrisano, V. Characterization of reversible and pseudo-irreversible acetylcholinesterase inhibitors by means of an immobilized enzyme reactor. *J. Chromatogr. A* **1144,** 102–110 (2007).

22.   Jennings, N. A., Pezzementi, L., Lawrence, A. L. & Watts, S. A. Acetylcholinesterase in the sea urchin Lytechinus variegatus: Characterization and developmental expression in larvae. *Comp. Biochem. Physiol. Part B Biochem. Mol. Biol.* **149,** 401–409 (2008).

23.   Loizzo, M. R., Tundis, R., Menichini, F. & Menichini, F. Natural products and their derivatives as cholinesterase inhibitors in the treatment of neurodegenerative disorders: an update. *Curr. Med. Chem.* **15,** 1209–28 (2008).

24.   Camps, P. *et al.* Huprine X is a novel high-affinity inhibitor of acetylcholinesterase that is of interest for treatment of Alzheimer's disease. *Mol. Pharmacol.* **57,** 409–417 (2000).

25.   Velan, B. *et al.* N-glycosylation of human acetylcholinesterase: effects on activity, stability and biosynthesis. *Biochem. J.* **296,** 649–656 (1993).

26.   Marchot, P., Khélif, A., Ji, Y. H., Mansuelle, P. & Bougis, P. E. Binding of 125I-fasciculin to rat brain acetylcholinesterase. The complex still binds diisopropyl fluorophosphate. *J. Biol. Chem.* **268,** 12458–67 (1993).

27.   Velan, B. *et al.* N-glycosylation of human acetylcholinesterase : effects and biosynthesis activity , stability. *Analysis* **656,** 649–656 (1993).

28.   Cer, R. Z., Mudunuri, U., Stephens, R. & Lebeda, F. J. IC50-to-Ki: A web-based tool for converting IC50 to Ki values for inhibitors of enzyme activity and ligand binding. *Nucleic Acids Res.* **37,** 441–445 (2009).

29.   Cheng, Y. & Prusoff, W. H. Relationship between the inhibition constant (KI) and the concentration of inhibitor which causes 50 per cent inhibition (I50) of an enzymatic reaction. *Biochem. Pharmacol.* **22,** 3099–3108 (1973).

30.   Koellner, G. *et al.* Active-site gorge and buried water molecules in crystal structures of acetylcholinesterase from Torpedo californica. *J. Mol. Biol.* **296,** 713–735 (2000).

31.   Bourne, Y. *et al.* Structural insights into ligand interactions at the acetylcholinesterase peripheral anionic site. *EMBO J.* **22,** 1–12 (2003).

32.   Bourne, Y. *et al.* Substrate and Product Trafficking through the Active Center Gorge of Acetylcholinesterase Analyzed by Crystallography and Equilibrium Binding. *J. Biol. Chem.* **281,** 29256–29267 (2006).

33.   Bartolini, M., Bertucci, C., Cavrini, V. & Andrisano, V. β-Amyloid aggregation induced by human acetylcholinesterase: inhibition studies. *Biochem. Pharmacol.* **65,** 407–416 (2003).

34.   Wang, M., Gu, X., Zhang, G., Zhang, D. & Zhu, D. Convenient and continuous fluorometric assay method for acetylcholinesterase and inhibitor screening based on the aggregation-induced emission. *Anal. Chem.* **81,** 4444–4449 (2009).

35.   Zhang, W., Zhu, L., Qin, J. & Yang, C. Novel Water-Soluble Red-Emitting Poly (p -phenylenevinylene) Derivative : Synthesis , Characterization , and Fluorescent Acetylcholinesterase Assays. 12059–12064 (2011).

36.   Tang, X., Wang, Y., Li, D., Luo, J. & Liu, M. Orphan G protein-coupled receptors (GPCRs): biological functions and potential drug targets. *Acta Pharmacol. Sin.* **33,** 363–371 (2012).

Chapter 3

Detection of various single nucleotide polymorphisms in short dsDNA sequences

3.1. Introduction to single nucleotide polymorphisms (SNPs)

The human genome is comprised of approximately 3 billion DNA bases in the chromosomes, Adenine (A), Thymine (T), Cytosine (C), and Guanine (G). Typical base-pair hydrogen bonding, the Watson-Crick base pairs that form the helical DNA duplex, is shown in Figure 3.1. The study and characterization of nucleic acid hybridization, or duplex formation, (both DNA and RNA) is an important area of biochemical research even after the sequencing of the entire human genome. The sequence of a series of nucleotides determines function in a gene, so if an alteration of an expected sequence occurs, the desired function can be significantly altered.   Single nucleotide polymorphisms (SNPs) in DNA, where a given nucleotide base is missing, replaced by a different base, or added to the sequence, account for the majority of genetic sequence variation in humans and other species. They occur at a rate of approximately 0.1% in the human genome, which accounts for less than 3 million bases out of the 3 billion that comprise the entire genome.[1] Most are harmless, can be used to determine ancestry, or explain differences in appearances, such as hair or eye colors.
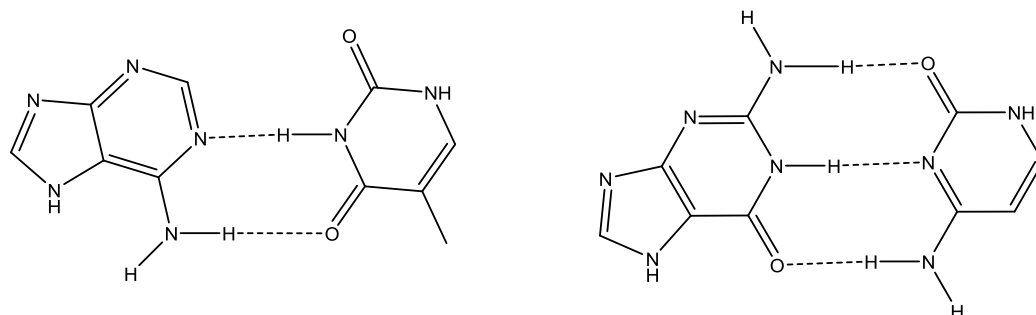
Figure 3.1. Watson-Crick base pairing of adenine and thymine (left), and guanine and cytosine (right).

3.1.1. Stabilities of SNPs in a DNA sequence

Different SNP mismatched pairings have different destabilizing effects. Their stabilities are affected by a variety of factors, including the number of hydrogen bonds between two bases, backbone shape, and π-stacking effects; thus, the stability of a particular base pair is also affected by their flanking bases (nearest neighbor, NN, effects). These effects were studied computationally by SantaLucia and coworkers.[2]
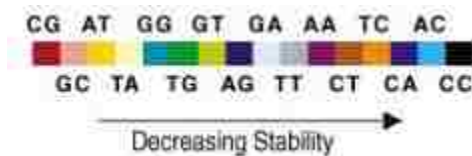
Figure 3.2. Order of thermodynamic stabilities of all possible base pairs determined by NN calculations.[2]

The Watson-Crick GC base pair is stronger than AT due to the additional hydrogen bond, and similarly, bases flanked by GC pairs are slightly more stabilized compared to the same pair flanked by AT pairs. Helical constraints make purine-purine base pairings unfavorable due to being too large, while pyrimidine-pyrimidine base pairings are too small.

With an insertion or deletion of one base, a single base bulge is formed in the duplex, which typically disrupt the helical axis by looping out and away from the axis.[3,4]

74

In folded RNA, bulges serve as highly recognizable and selective features for protein binding, but in helical DNA they are very destabilizing.[4,5] Nearest neighbor effects play a role in bulged duplex stability as well, with an effect known as positional degeneracy that makes bulged bases more stable if they are flanked by the same base.[5,6]

3.1.2. The role of SNPs in genetic diseases

The ClinVar database is a large compilation of SNPs that have been found and associated with a particular disease or condition. Certain SNPs in the regulatory or coding region of genes (exons) increase an individual's susceptibility to certain diseases or health conditions by introducing premature stop codons, or coding for alternative amino acids to disrupt a protein's function. Examples include hypertension, osteoporosis, Celiac's, cystic fibrosis, and certain cancers.[7,8] This is in contrast to diseases or conditions caused by microdeletions, in which small portions of a gene are missing (no greater than 5 million base pairs).

The presence or absence of a SNP does not guarantee an individual will be afflicted with a given condition or disease, and sometimes a combination of several SNPs on different genes must all be present to cause the disease. For example, several insertions have been identified on chromosome 17 that are associated with Hereditary Breast and Ovarian Cancer (HBOC), including two A insertions. These polymorphisms have been found to predispose individuals to early onset breast, ovarian, or fallopian tube cancers, with a lifetime risk of breast cancer over 50%.[9,10]

Another example of a disease caused by more than one SNP is X-linked myopathy with excessive autophagy (XMEA), a disorder that is marked by weakening and degeneration of skeletal muscle tissue. Six mismatch SNPs were identified on the

VMA21 gene on the X chromosome, each contributing to disruptions in RNA splicing that ultimately led to decreased V-ATPase activity, which led to increased lysosomal pH.[11,12] Conversely, an example of a disease that is caused by only a single SNP on a single gene, known as a Mendelian or single-gene disorder, is Factor V Leiden, which causes excessive clotting in the bloodstream. The most common SNP variant in this disease is a mismatch that replaces a G with an A.[13]

Identifying new SNPs may help pinpoint potential causes or targets of a disease. Additionally, understanding particular SNPs or mapping known SNPs in important genetic regions may assist in advancing fields of personalized medicines. A better understanding of a SNP's location would allow for a more thorough understanding of its specific role in the disruption of a gene's desired function, and a better understanding of the binding affinities of SNP-containing duplexes could aid in the development of methods to restore normal function. Thus, a simple, straightforward, and rapid approach to detecting SNPs in DNA is important for disease detection and diagnostics.

3.1.3. Common methods to detect SNPs

Many experiments designed to detect SNPs in short (typically <30 base pairs) oligonucleotide sequences use fluorophores tethered to a duplex to measure binding interactions,[14] gold nanoparticles, where a probe strand is functionalized to the surface of the NPs, and produces a measurable absorbance change in the visible light region upon introduction of a complementary sequence,[15,16] surface plasmon resonance (SPR), where a probe strand interacts with a strand containing a SNP which can then target a probe tethered to the surface,[17] or molecular beacons (MBs).[18–21] MBs were developed in the past 20 years to detect specific oligonucleotide sequences and have been used

76

successfully to separate and score SNPs during PCR.[19] One drawback of MBs is their limited sensitivity due to background signal and inefficient fluorophore quenching.[18] Methods to overcome these drawbacks and increase sensitivity have been developed, such as using graphene oxides as nanoquenchers,[20] conjugating new fluorescent dyes,[21] and other amplification techniques.[18] However, generation or conjugation of MBs and any additional components can be tedious and costly.   Similarly, syntheses of fluorophores and tethering components to a surface can involve laborious procedures.

Perhaps more importantly, an earlier study using BSI to detect DNA hybridization, as discussed previously in section 1.3.2, demonstrated the significant effect actions such as fluorophore labeling or tethering an analyte have on the binding affinity of the two binding partners, with perturbations causing up to a 50% difference in binding affinity.[22] Obtaining a true measure of affinity at relevant conditions is desired, and BSI provides a suitable platform for such measurements in free-solution, and label free.

3.1.4. Previous BSI hybridization experiments

Prior experiments probing DNA duplexes and SNPs with BSI demonstrated the ability to identify a two base-pair mismatch centrally located in the sequence with this technique based on a significant destabilization effect, and a higher dissociation constant for the duplex. Conversely, the same two base-pair mismatch located at the 5' terminal position showed a stabilizing effect (lower dissociation constant).[22] These experiments were performed with 30-base pair oligonucleotides.   We thus sought to determine whether BSI would be able to distinguish a single SNP, rather than two adjacent ones, based on differences in K_D values.   Additionally, would BSI be able to distinguish between different types of SNPs? This previous study probed an A/G mismatch, where

the G replaced the complementary T. We planned to use the same A/G mismatch, but also study two sequences containing a T deletion, as well. Finally, we also sought to observe the difference in stabilities when the same SNP is located in different locations in the sequence. Since terminal mismatches have shown to have negligible or even slightly stabilizing effects, and centrally-located mismatches have a destabilizing effect, we expected a SNP located between the middle and end of the sequence, about a quarter of the way from the end, would still destabilize the sequence, but to a lesser degree than a centrally located SNP.

The BSI experiments designed for this expanded SNP research used shorter, 20-base pair sequences to be more consistent with other techniques.[15–18] We hypothesized that BSI would have the ability to distinguish between a single mismatch or deletion at different locations in the sequence, in the middle or nearer to the end, and a perfect complement, with each strand interacting with the same actin probe strand. A non-binding nonsense strand was used as a negative control to demonstrate the generation of negligible binding signal upon mixing and equilibration of the two oligonucleotides, highlighting that the signal arises from the DNA hybridization, rather than simply increasing concentrations of analytes present.

Results obtained with BSI were benchmarked with hyperchromicity studies and melting temperatures obtained using a CD spectrometer. Hyperchromicity is a property of duplexed DNA that describes the increase in UV absorbance (measured at 260 nm) as the duplex is slowly heated and denatured, causing the single strands to separate. More heat is required to denature sequences with a higher affinity, thus higher melting transition temperatures (T_m) are indicative of tighter binding in a similar way that lower

78

K_D values indicate tighter binding, and so a lower K_D value obtained from a BSI experiment would correlate with a higher T_m value obtained from the CD.

The ability of BSI to distinguish between a perfect complement duplex and a variety of SNPs label-free and in free solution allows for a true measure of duplex affinity without any additional components or perturbations, and would make BSI a powerful tool for future research regarding SNP detection and diagnostics. With a probe volume of just 7.52 nL and an oligonucleotide concentration ranging from 25-250 nM, BSI uses substantially fewer materials than more common free-solution techniques such as isothermal titration calorimetry (ITC) or melting transition studies, which require higher volumes and concentrations. It also requires no PCR amplification. The small sample sizes and straightforward procedure make BSI an ideal candidate for an analytical instrument that can be used to detect SNPs in a duplex, or eventually, for diagnostics in seeking a particular SNP versus a complement sequence of a target region.

3.2. Materials and Methods

3.2.1. Functionalization of chip channels

The channels in the glass microfluidic chip were silanized to prevent nonspecific binding of the oligonucleotides to the channel walls upon introduction of sample. After a one hour sulfuric acid soak to clear the channels, they were rinsed with water and methanol, followed by a half hour soak of a 10% solution of KOH in MeOH. The wells of the channels were refilled every eight to ten minutes to prevent drying. Next, the channels were rinsed with water, methanol, and toluene. They were then filled with a 2% solution of 3-mercaptopropyltriethoxysilane (MEPTES, Sigma Aldrich) in toluene for

one hour, with refills every fifteen minutes to prevent drying. Finally, the channels were rinsed with toluene, methanol, and water, and the chip secured in the stage.

3.2.2. Oligonucleotide sample preparation

Oligonucleotides were obtained from Biosynthesis (Lewisville, TX) at 250 nmol HPLC purity. Seven 20-base pair oligonucleotides were used for these experiments. Oligonucleotides were reconstituted by first adding a volume of phosphate-buffered saline (PBS) equal to ten times the nmole amount. 5 µL of this solution was added to 995 µL of PBS, and the absorbance of this new solution was measured at 260 nm using a UV Spectrometer. The concentrations of the original reconstituted solutions were determined with Beer's Law. BSI stock solutions were set to 200 nM for the probe actin strand, whose sequence was derived from the mouse actin gene, and 500 nM for each binding strand. BSI sample solutions were then made via serial dilutions, with the actin oligonucleotide (probe strand) serving as the receptor, with a concentration held constant at 100 nM and the binding oligonucleotide concentration varying from 0-250 nM. These solutions were left to equilibrate overnight in a refrigerator before running experiments the next day.

3.2.3. BSI experiments

Prior to starting experiments, the laser and temperature controller were allowed to warm up and equilibrate for approximately one hour. The temperature of the BSI stage was held at 25 °C. Experiments were conducted by pipetting 1 µL of buffer into the channel to check signal stability and repeatability, then each subsequent sample was injected, starting with the zero point (buffer and probe strand only) and data was collected for 1 min. This helps to minimize noise from the initial baseline disruption

80

immediately following injection. After each injection, the channels were cleared by vacuuming through the opposite well. Blank, or reference, samples displayed no additional signal change from the buffer reference.

One oligonucleotide with a complementary sequence of the actin probe strand and four strands containing one SNP were studied to obtain binding data: 1) an A/G mismatch located at the center of the sequence (Center Mismatch), 2) an A/G mismatch located halfway between the center and the end of the sequence (Quarter Mismatch), 3) a T deletion located at the center of the sequence (Center Deletion), and 4) a T deletion located halfway between the center and end of the sequence (Quarter Deletion). One nonsense strand, in which no bases would match with the probe sequence, was used as a negative control. The oligonucleotide sequences are listed in Table 1.

Table 3.1. DNA oligonucleotides studied. Mismatched base pairs are bolded and underlined. Deleted base pairs are indicated by their neighboring base pairs (bold and underlined).

Strand	Sequence
Actin	5'-ACTCATCGTACTCCTGCTTG-3'
Complement	5'-CAAGCAGGAGTACGATGAGT-3'
Center Mismatch	5'-CAAGCAGGAG***G***ACGATGAGT-3'
Quarter Mismatch	5'-CAAGCAGGAGTACGA***G***GAGT-3'
Center Deletion	5'-CAAGCAGGA***GA***CGATGAGT-3'
Quarter Deletion	5'-CAAGCAGGAGTACG***AG***AGT-3'
Nonsense	5'-ATGAGTACGATGGAGACGAC-3'

3.2.4. BSI data analysis

The data were analyzed and plotted with graphical software, and K_D values were calculated from a one-site binding hyperbola equation (Eq 3 in Chapter 1). Error in the K_D was determined from the standard deviation of each data point as well as differences between the predicted values from the equation and the observed values, using an Excel Solver macro. Each data point was subtracted from the zero point, that is, the sample with probe strand of actin present in buffer but no binding oligomer present. Blanks containing only the binding oligomer featured no discernible signal above the noise level, and so were not used for zeroing the data.

3.2.5. Hyperchromicity studies

To correlate the BSI results with those from a more well-known and widely-available method, melting transition temperatures for each duplex were determined using Circular Dichroism (CD) Spectroscopy. The concentration of each duplex was 5 μM, and the samples were allowed to equilibrate at room temperature for at least one hour prior to experiments. In these experiments, repeated thrice to determine standard error, the absorbance was measured at 260 nm while the temperature increased gradually (1 °C/min) from 30 °C to 75 °C. A higher melting transition temperature, indicative of stronger binding and duplex stability, was expected to correlate with a lower BSI K_D value.

3.3. Results and Discussion

3.3.1. BSI binding results and K_D values

The previous BSI experiments studying DNA hybridization featured 30-base pair sequences with the actin probe strand held constant at 150 nM. A calibration of a duplex of the probe strand and its complement, shown in Figure 3.3, exhibited the expected

linear response of the signal (phase shift) with increasing concentration of duplex, and it was determined that for these experiments, the concentration of the probe strand could be lowered to 100 nM. Greater error and deviation from the expected linear trend is seen at higher concentrations, where the expected linear signal response to concentration tends to break down likely due to aggregation, so experiments are designed to avoid product (duplex) concentration in those regions.
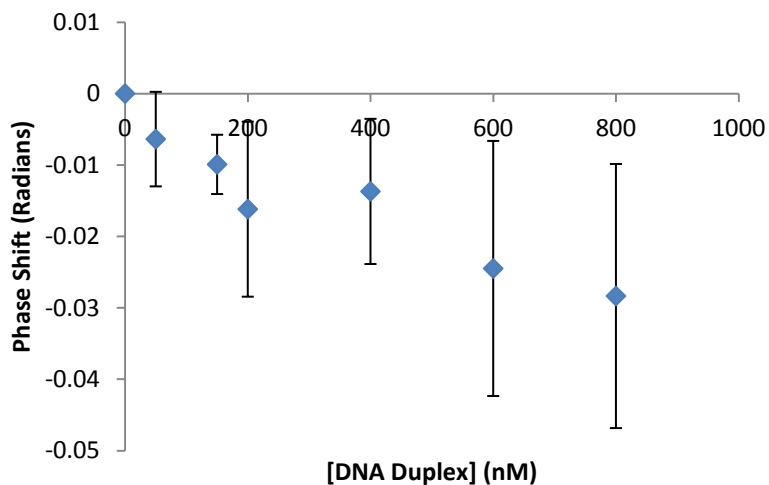
Figure 3.3. Calibration of duplexed probe strand and complement.

For all of these experiments, the signal returned to its approximate initial starting position (accounting for minor changes in environmental factors affecting signal) for the first sample after the final sample, containing the highest concentration of DNA, which indicated that the silanization was effective and no DNA was interacting with the surface to cause erroneous signals. Upon completion of experiments in all three channels of the microfluidic chip, they were rinsed, sonicated, and resilanized for a fresh coating each time. Individual binding curves for each duplex are shown in Figures 3.4-3.9. Each data point represents the average of at least five trials over three or more days, with error bars representing the standard error of the mean (SEM).
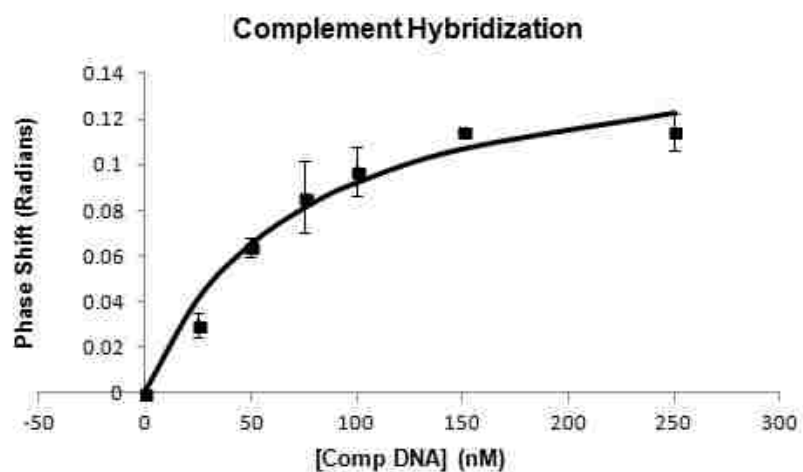
Figure 3.4. BSI binding curve of signal vs. concentration of binding strand, which has a complementary sequence to the probe strand.
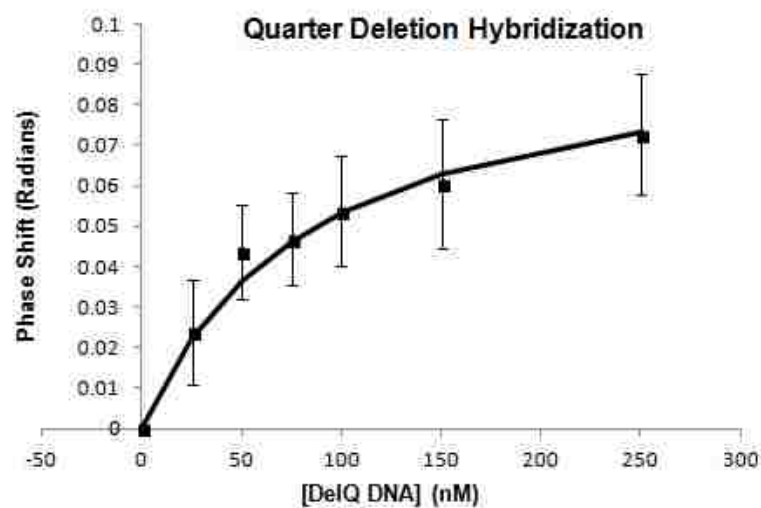
Figure 3.5. BSI binding curve of signal vs. concentration of binding strand, which contains a T deletion located four base pairs from the 3'-end of the oligomer.
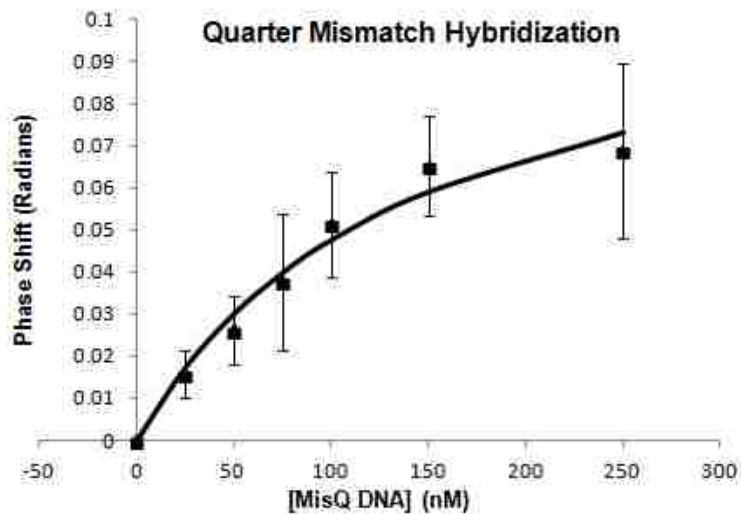
Figure 3.6. BSI binding curve of signal vs. concentration of binding strand, which contains an A/G mismatch located four base pairs from the 3'-end of the oligomer.
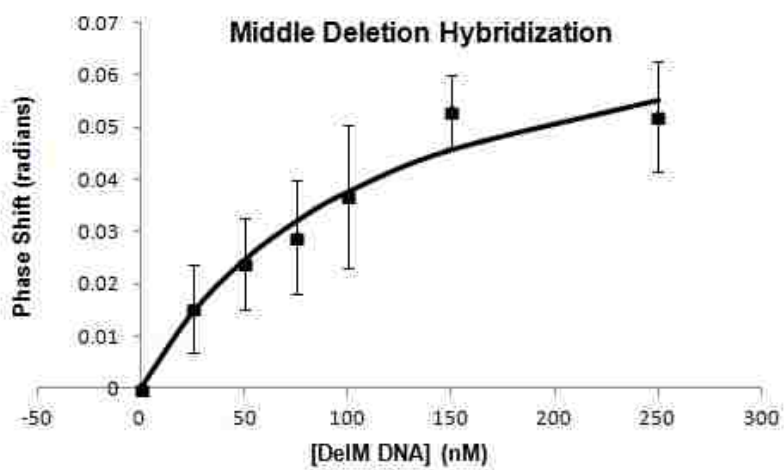
Figure 3.7. BSI binding curve of signal vs. concentration of binding strand, which contains a T deletion located in the center of the oligomer's sequence.
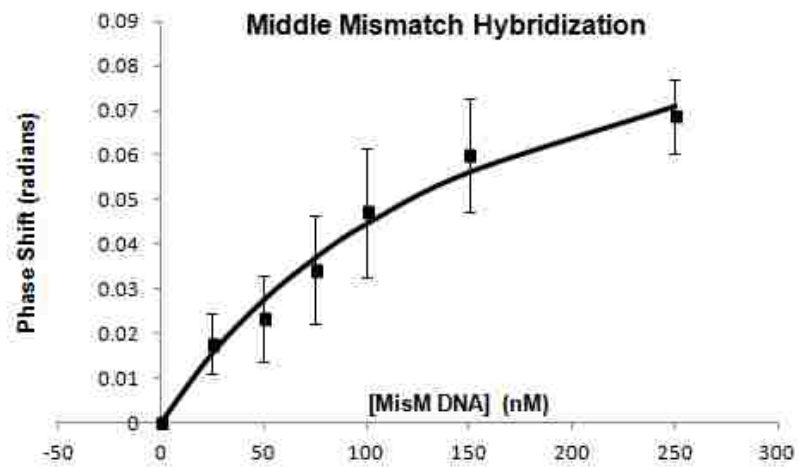
Figure 3.8. BSI binding curve of signal vs. concentration of binding strand, which contains an A/G mismatch located in the center of the oligomer's sequence.
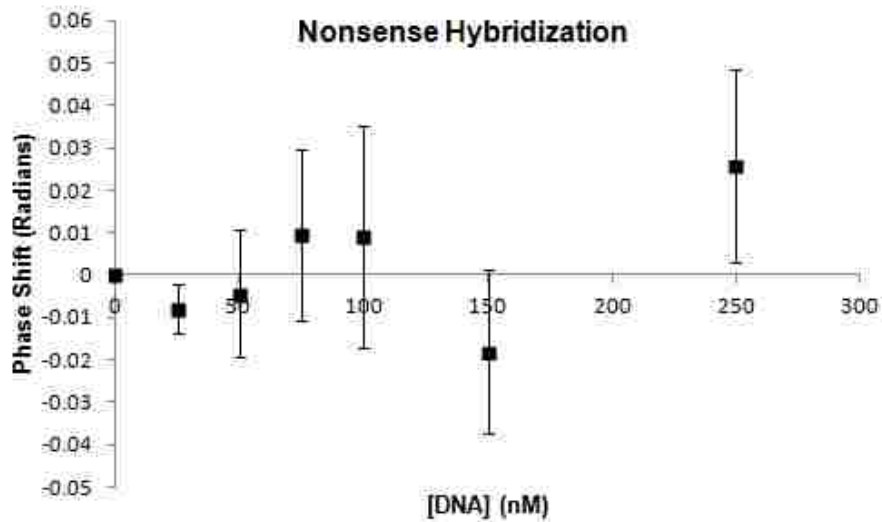
Figure 3.9. BSI plot of signal vs. concentration of samples containing a nonsense strand, a random sequence, in which little to no hybridization is expected.

Table 3.2. BSI K_D values of oligomer duplexes.

Duplex Binding Strand	K_D (nM)
Complement	71.4 ± 18
Quarter Deletion	84.8 ± 15
Quarter Mismatch	139 ± 38
Middle Deletion	113 ± 34
Middle Mismatch	163 ± 37

The K_D values of each duplex are listed in Table 3.2. As expected, the complementary duplex had the lowest K_D value, indicative of the strongest binding. In addition to expecting the complementary duplex to exhibit the strongest binding, we anticipated the duplexes containing a SNP closer to the end of the sequence would be more stable than those containing a SNP in the middle of the sequence, as a centrally-located SNP had the potential to disrupt a larger portion of the duplex compared to one nearer the end, and terminal mismatches have even been shown to stabilize binding, resulting in a lower K_D value compared to the complementary duplex.[22,23]

When comparing the K_D values (Table 3.2) of both sets of similar SNPs, that is, the quarter and center deletions (K_D's of 84.8 and 113 nM), and the quarter and center mismatches (139 and 163 nM), this hypothesis is correct. However, the center deletion still exhibited a lower K_D value than the quarter mismatch (113 and 139 nM), indicating that the A/G mismatch had a greater destabilizing effect on the hybridized DNA than the T deletion regardless of location within the sequence.

3.3.2. CD melting temperature results and comparison to BSI

The melting transition profiles of absorbance at 260 nm versus temperature for each duplex are shown in Figure 3.10, and the T_m for each duplex is listed in Table 3.3 along with its corresponding BSI K_D.
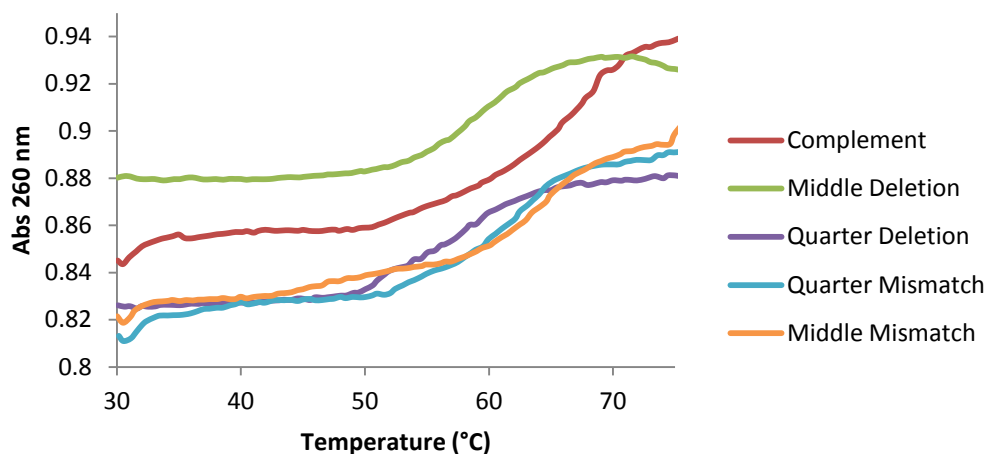
Figure 3.10. Melting transition profiles for DNA duplexes.

Table 3.3. T_m of duplexes compared to BSI K_D values.

Duplex Binding Strand	T_m (°C)	K_D (nM)
Complement	68.7 $\pm$ 0.3	71.4 $\pm$ 18
Quarter Deletion	59.0 $\pm$ 0.5	84.8 $\pm$ 15
Quarter Mismatch	60.9 $\pm$ 0.6	139 $\pm$ 38
Middle Deletion	56.5 $\pm$ 1.4	113 $\pm$ 34
Middle Mismatch	52.0, 64.2 $\pm$ 1.5	163 $\pm$ 37

The melting temperatures of the duplexes correlated with the BSI results, most notably with the complement duplex exhibiting the lowest K_D value and the highest T_m, again indicating it is the most stable duplex tested in this study. Likewise the quarter SNPs had a lower T_m than the complementary duplex but a higher T_m compared to the middle SNPs, indicating that more centrally-located SNPs have a greater destabilizing effect on the duplex affinity. This is graphically represented in Figures 3.11 and 3.12,

which examine at the comparison of K_D and T_m values between the same SNP (deletion or mismatch) in different locations and the complement.
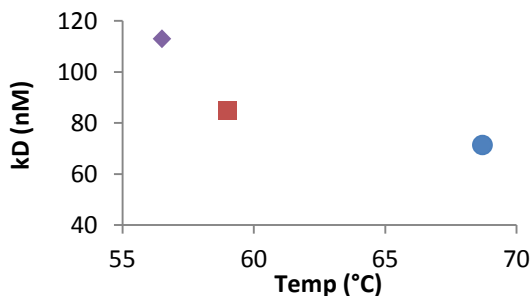
Figure 3.11. Graphical representation of comparison of BSI K_D values to CD T_m values of complementary duplex (●) with centrally located T deletion (♦) and quarter T deletion (■). The more to the lower right the data point is, the stronger the binding affinity of the duplex.
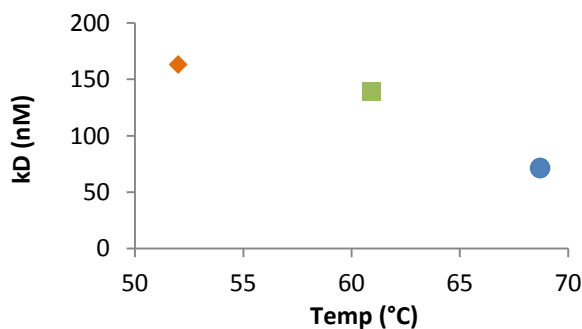
Figure 3.12. Graphical representation of comparison of BSI K_D values to CD T_m values of complementary duplex (●) with centrally located A/G mismatch (lower T_m) (♦) and quarter A/G mismatch (■). The more to the lower right the data point is, the stronger the binding affinity of the duplex.

One notable exception was the center A/G mismatch duplex, which had the highest K_D value of the duplexes studied (163 nM), indicating it was the least stable, however its main T_m was unexpectedly high (64.2 °C). Upon closer examination, the CD melting profile seems to indicate that not just one complete melting transition was present, but instead two small melting transitions were present with a more gradual absorbance increase before the major melting transition (Figure 3.13).

89
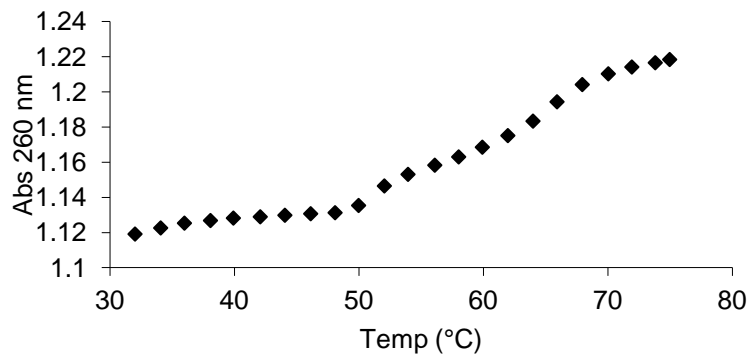
Figure 3.13. T_m profile of the middle mismatch duplex showing two melting transitions.

When graphically observing this lower melting transition temperature (52.0 °C) in Figure 3.13, the expected trend is much clearer. This suggests that the oligonucleotides containing the central A/G mismatch may not form one duplex in equilibrium, but due to the ability of this mismatch to form up to four different hydrogen bonding patterns, plus the fact that this purine-purine pairing is too large for the typical helical backbone size,[24,25] there may have been a more complex equilibrium of two or more duplex conformations present, for example one in which both bases are in the anti position, and one in which one is syn and one is anti; the structures of these possible conformations are shown in Figure 3.14.
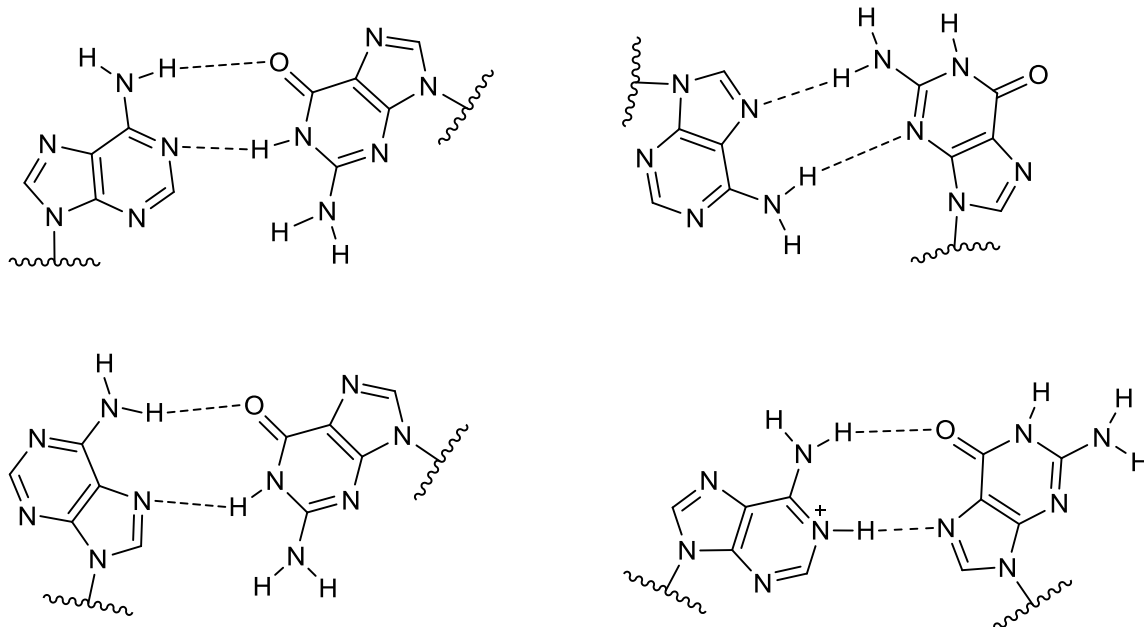
Figure 3.14. Possible structures of an A/G mismatch pair.

These conformations would result in duplexes that have different melting transition temperatures due to varying stabilities of the A-G hydrogen bonds and disruption to the overall shape of the duplex. The instability of the duplex and variations in base-pair binding would also explain the larger K_D values observed in the BSI experiments, and the potential for a more complex equilibrium between structures would also explain the larger error bars seen in the SNP binding curves compared to the complement. These effects would also be less pronounced for the quarter mismatch duplex since they would not be occurring in the center of the duplex and thus disrupting a larger portion of the duplex. And while the deletion of a T creates an A bulge upon hybridization, which is farther destabilized due to not being flanked by other A bases,[5] the bulge overall causes less disruption to the overall stability than the A/G mismatch.

3.3.3. Signal magnitude and FreeSRF of duplexes

All DNA binding curves featured a positive binding curve for our specific detector's orientation. Calibration curves, both of glycerol and double-stranded DNA (dsDNA), show a phase shift that increases in the negative direction with increasing concentration, which correlates to an increase in optical density. The hybridization of DNA duplexes causes an overall decrease in optical density and refractive index of the solution. This is seen in the positive signal direction as binding occurs. A decrease in RI has been shown to result from decreases in hydrodynamic radius,[26] which would be expected as single-stranded DNA (ssDNA) hybridizes to dsDNA, decreasing the overall length with 'accordion-like' shrinking.[27]
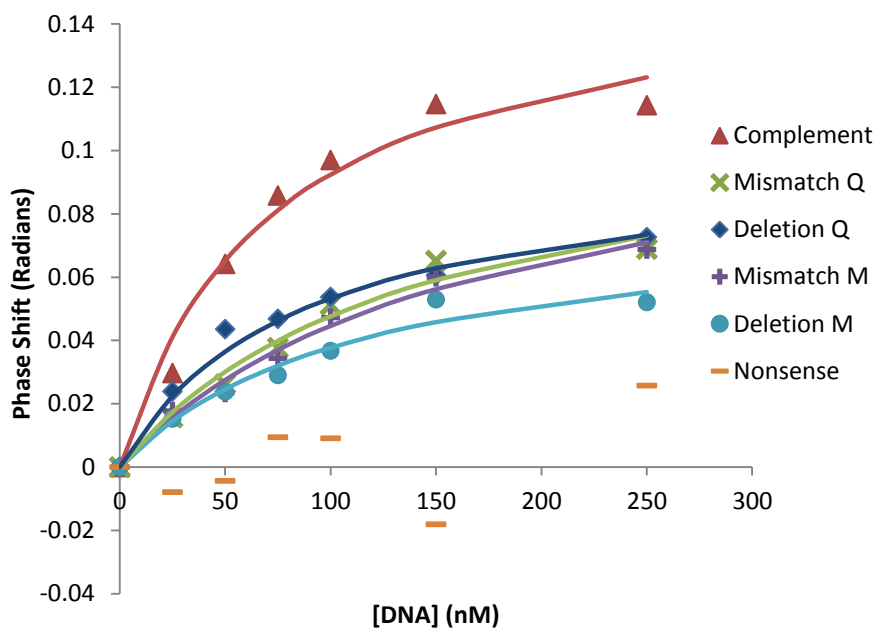
Figure 3.15. Binding curves obtained with BSI for each DNA duplex.

Additionally, the complementary duplex also exhibited the largest positive phase shift, or signal change, compared to the duplexes containing a SNP, as shown in Figure

3.15. The signal of BSI is believed to derive from a variety of factors, including solvent displacement (solvent-accessible surface area, SASA) and structural changes (measured by radius of gyration, R_{gyr}),[26,28] which alter the bulk optical density and refractive index of the solution.   This indicates that the complementary duplex has the largest bulk refractive index changes compared to the duplexes containing a SNP.   The Bornhop group has also correlated number of binding base pairs with signal magnitude,[29] so this trend also fits our observations that the complementary duplex exhibits the strongest binding compared to the SNP duplexes that have greater disruptions to binding due to the unfavorable mismatch or base bulge. Using the FreeSRF expression described in Chapter 1.4, it is possible to calculate the molar refractometry, χ_{exp}, for each duplex.

Table 3.4. K_D, B_{max}, and χ_{exp} values of DNA duplexes.

Duplex Binding Strand	K_D (nM)	B_{max} (radians)	χ_{exp} (RIU/M)
Complement	71.4	0.158	-1663.08
Quarter Deletion	84.8	0.098	-1033.01
Quarter Mismatch	139	0.114	-1195.37
Middle Deletion	113	0.080	-845.40
Middle Mismatch	163	0.117	-1232.42

The K_D, B_{max}, and χ_{exp} values of each DNA duplex are listed in Table 3.4. B_{max} from the one-site binding hyperbola equation is equal to the maximum possible signal from the maximum concentration of dsDNA. Since the receptor probe strand is held at 100 nM, C_{Bmax} of the dsDNA would be 100 nM. The complement duplex has at least a 35% higher signal compared to the other duplexes containing a SNP.   The signal magnitude, and thus χ_{exp}, does not follow the same trend as the K_Ds for each duplex, however. Despite being the most destabilized, the mismatched duplexes have a higher signal and χ_{exp} than the deletion duplexes, at 0.114 and 0.117 radians compared to 0.098

and 0.080 for the deletions. This indicates that despite forming a weaker duplex, the dsDNA containing an A/G mismatch exhibit greater changes in RI upon hybridization.

Molar refractometry, χ_{exp}, is a term that encompasses the changes in an analyte's intrinsic properties. When testing the validity of the FreeSRF expression, Bornhop and coworkers modeled χ values based on R_{gyr} and SASA, and developed fitting coefficients with training sets to compare modeled and experimental χ's.[26] This training set was divided into two arbitrary subsets: large and small, based on the χ_{exp} of the training set systems. The χ_{exp} values for the duplexes in this study fall into a range that were included in the large training set (|782-1379| RIU/M), but saw significant (>200%) error with the fitting coefficients, suggesting that an intermediate set of coefficients might be preferable for χ_{exp} values in this range (the authors also acknowledged that the training model could be fit into more subsets, and most likely will be as more training set systems are added). An added challenge for determining ΔR_{gyr} of going from ssDNA to dsDNA could also involve the overall shape of the molecules; where proteins tend to be mostly globular, DNA strands are more flexible and cylindrical or chain-like in shape.

Additionally, one intrinsic property that could likely play an important role in DNA hybridization that is presently unaccounted for in the FreeSRF model is polarizability. Fumagalli and coworkers examined this property of dsDNA and discovered the dielectric constant of dsDNA, ε_r, is significantly higher than originally assumed, with a value of ~8 as opposed to the low polarizability of proteins to which it was usually compared ($\varepsilon_r \sim 2$-4).[30] This high polarizability is attributed to the high charge on the backbone and the π-stacking along the inside of the helix. A base bulge looped-out of the helix could have a more significant impact on a duplex's polarizability

compared to a mismatch since the mismatch still retains all of the bases within the backbone of the helix.

Taking the K_D results and the signal magnitude, or χ_{exp}, together, we have shown that stronger DNA duplex binding generates a greater change in RI compared to weaker binding in duplexes containing a SNP. This is reasonable because mismatched base pairs disrupt hybridization and can have different configurations that are not as strong due to helical constraints or unfavorable hydrogen bonds; in particular, the A/G mismatched bases used in this experiment have been shown to have up to four different hydrogen bond configurations.[24,25]

Similarly, a sequence containing a deletion would create a small bulge in the oligonucleotide so the remaining bases may bind, which would disrupt the overall hybridization.[31] These factors negatively affect the stabilities and structures of the duplexes, and decrease the number of binding events in the duplex.[29] With less stability, lowered polarizability, and fewer binding base pairs within the structure of the helix, a smaller signal shift would be observed. Conversely, the complementary duplex would have the largest amount of bound bases, a greater degree of change in conformation to accommodate the binding of those bases, and higher polarizability due to undisrupted π-stacking of the complementary bases. These factors lead to stronger binding and a larger phase shift.

3.4. Conclusion

BSI has the ability to distinguish a 20-base pair DNA duplex formed with a complementary oligonucleotide from various oligonucleotides containing one SNP, either a deleted base (G) or an A/G mismatch. Additionally, BSI was able to distinguish

between duplexes containing a mismatched or deleted base pair, as well as between duplexes with a given SNP in different locations in the sequence, based on the binding affinity of each duplex measured as a K_D value. Specifically, these results showed that (1) a centrally located SNP was more destabilizing than that same SNP located closer to the end of the sequence, (2) an A/G mismatch had a greater impact on destabilization than a T deletion regardless of their location in the sequence, and finally (3) the complementary duplex featured a larger signal magnitude (in the positive direction) compared to duplexes containing SNPs, which was attributed to the greater number of favorably-interacting base pairs. These results correlated with a more commonly employed method, measuring melting transition temperatures using CD, and highlight BSI's excellent sensitivity in its ability to detect seemingly small differences between the type of SNP present and different locations separated by just four bases out of twenty.

Previous experiments have shown that BSI is capable of distinguishing a complementary, 30-base pair duplex from a duplex containing two centrally-located mismatches with a probe strand concentration of 150 nM.[22] The present experiment used shorter sequences to be more consistent with other types of research employing short DNA sequences to examine hybridization (typically 18-24 bp oligonucleotides),[15–19] and a probe strand held at 100 nM, while the binding strands varied in concentration from 25 nM up to 250 nM. Considering the probe volume of the instrument (7.52 nL), this equates to measuring 113,000,000 binding strand molecules. This probe volume is orders of magnitude lower than other techniques; SNP detection studies with Molecular Beacons used 25 μL with concentrations of 200 nM,[19] and techniques with SPR required flow rates of 20-30 μL/min at similar concentration ranges (10-100 nM).[17] Using gold

nanoparticles, SNPs have been detected at concentrations of oligonucleotides as low as 2.5 nM, but this required several hours of sample preparation, and used tags on the oligonucleotides.[16] BSI's main advantages lie in its ability to detect a variety of SNPs at similar, low concentrations in their natural (free solution and label-free) state at physiological conditions, relying solely on the hybridization of a duplex to generate a signal.

The source of the BSI signal is attributed to bulk changes in solution which alter the refractive index, or optical density of the solution, including conformation changes, such as the formation of the helical duplex, and solvation, as the solvent molecules surrounding the oligonucleotides are expelled as they interact and form the base pair hydrogen bonds. We observed a much higher signal in the complementary duplex (>35%) compared to the four SNP duplexes, which we attributed to the stronger binding and higher number of base pairs able to interact with their complement. Similarly, Bornhop and coworkers have observed that the magnitude of the BSI signal increases as a duplex is converted from its native B-form to A-form or with DNA:RNA hybrids.[29] We also discuss potential additional considerations to the FreeSRF model to accurately account for DNA hybridization as it has with protein systems, including accounting for the unexpectedly high polarizability of dsDNA.

The low concentrations and small amount of sample required for a BSI experiment (1 μL injections), and the ability to perform these experiments label-free and in free solution make BSI a viable instrument for detecting SNPs. BSI has also been shown to work with full serum samples,[32] so our hope is that in the future, commercialized instruments will be widely available for use in both rapidly detecting

SNPs in a target region, and for diagnoses for conditions and diseases impacted by certain SNPs.

3.5. References

1.   What are single nucleotide polymorphisms? (2016). Available at: https://ghr.nlm.nih.gov/primer/genomicresearch/snp. (Accessed: 15th June 2016)

2.   Santalucia, J. & Hicks, D. THE THERMODYNAMICS OF DNA STRUCTURAL MOTIFS. *Annu. Rev. Biophys. Biomol. Struct* **33,** 415–40 (2004).

3.   Von Ahsen, N., Oellerich, M. & Schutz, E. DNA base bulge vs unmatched end formation in probe-based diagnostic insertion/deletion genotyping: Genotyping the UGT1A1 (TA)(n) polymorphism by real-time fluorescence PCR. *Clin. Chem.* **46,** 1939–1945 (2000).

4.   Lilley, D. M. J. Review Kinking of DNA and RNA by base bulges. **92,** 7140–7142 (1995).

5.   Ke, S.-H. & Wartell, R. M. Influence of Neighboring Base Pairs on the Stability of Single Base Bulges and Base Pairs in a DNA Fragmentt. *Biochemistry* **34,** 4593–4600 (1995).

6.   Zhu, J. & Wartell, R. M. The Effect of Base Sequence on the Stability of RNA and DNA Single Base Bulges. doi:10.1021/bi9916372

7.   ClinVar Variation Type: Single Nucleotide. (2016). Available at: http://www.ncbi.nlm.nih.gov/clinvar. (Accessed: 1st September 2015)

8.   de Bakker, P. I. W. *et al.* A high-resolution HLA and SNP haplotype map for disease association studies in the extended human MHC. *Nat. Genet.* **38,** 1166–72 (2006).

9.   GeneDX. ClinVar NM_007294.3:c.3627insA. (2014). Available at: http://www.ncbi.nlm.nih.gov/clinvar/variation/182112/#summary-evidence. (Accessed: 20th June 2016)

10.   GeneDX. ClinVar NM_007294.3:c.3648insA. (2014). Available at: http://www.ncbi.nlm.nih.gov/clinvar/variation/182113/#summary-evidence. (Accessed: 20th June 2016)

11.   Dowling, J. J., Moore, S. A., Kalimo, H. & Minassian, B. A. X-linked myopathy with excessive autophagy: a failure of self-eating. *Acta Neuropathol.* **129,** 383–90 (2015).

12.   Ramachandran, N. *et al.* VMA21 deficiency prevents vacuolar ATPase assembly and causes autophagic vacuolar myopathy. *Acta Neuropathol* **125,** 439–457 (2013).

13.   Bertina, R. M. *et al.* Mutation in blood coagulation factor V associated with resistance to activated protein C. *Nature* **369,** 64–7 (1994).

14.   Sun, Y. *et al.* Real-time fluorescence ligase chain reaction for sensitive detection of single nucleotide polymorphism based on fluorescence resonance energy transfer. *Biosens. Bioelectron.* **74,** 705–10 (2015).

15.   Cho, K. *et al.* Selective Aggregation Mechanism of Unmodified Gold Nanoparticles in Detection of Single Nucleotide Polymorphism. (2008).

16.   He, Y. *et al.* Visual Detection of Single-Nucleotide Polymorphism with Hairpin Oligonucleotide-Functionalized Gold Nanoparticles. (2010).

17.   Miura, S. *et al.* DNA-Binding Small-Ligand-Immobilized Surface Plasmon Resonance Biosensor for Detecting Thymine-Related Single-Nucleotide Polymorphisms. *Chem. - A Eur. J.* **17,** 14104–14110 (2011).

18.   Wang, K. *et al.* Molecular engineering of DNA: molecular beacons. *Angew. Chem. Int. Ed. Engl.* **48,** 856–70 (2009).

19.   Mhlanga, M. M. & Malmberg, L. Using molecular beacons to detect single-nucleotide polymorphisms with real-time PCR. *Methods* **25,** 463–71 (2001).

20.   Lu, C.-H. *et al.* Increasing the Sensitivity and Single-Base Mismatch Selectivity of the Molecular Beacon Using Graphene Oxide as the 'Nanoquencher'. *Chem. - A Eur. J.* **16,** 4889–4894 (2010).

21.   James Yang, C., Pinto, M., Schanze, K. & Tan, W. Amplifying Fluorescent Polymers Direct Synthesis of an Oligonucleotide–Poly- (phenylene ethynylene) Conjugate with a Precise One-to-One Molecular Ratio**. doi:10.1002/anie.200462431

22.   Pesciotta, E. N., Bornhop, D. J. & Flowers, R. A. Back-scattering interferometry: A versatile platform for the study of free-solution versus surface-immobilized hybridization. *Chem. - An Asian J.* **6,** 70–73 (2011).

23.   Fish, D. J. *et al.* DNA multiplex hybridization on microarrays and thermodynamic stability in solution: a direct comparison. *Nucleic Acids Res.* **35,** 7197–208 (2007).

24.   Li, Y., Zon, G. & Wilson, W. D. Thermodynamics of DNA duplexes with adjacent G.A mismatches. *Biochemistry* **30,** 7566–7572 (1991).

25.   Brown, T., Hunter, W. N., Kneale, G. & Kennard, O. Molecular structure of the G.A base pair in DNA and its implications for the mechanism of transversion mutations. *Proc. Natl. Acad. Sci. U. S. A.* **83,** 2402–6 (1986).

26.   Bornhop, D. J., Kammer, M. N., Kussrow, A., Flowers, R. A. & Meiler, J. Origin and prediction of free-solution interaction studies performed label-free. *Proc. Natl. Acad. Sci. U. S. A.* **113,** E1595–604 (2016).

27.   Elhadj, S., Singh, G. & Saraf, R. F. Optical Properties of an Immobilized DNA Monolayer from 255 to 700 nm. *Langmuir* **20,** 5539–5543 (2004).

28.   Swinney, K. & Bornhop, D. J. A chip-scale universal detector for electrophoresis based on backscattering interferometry. *Analyst* **125,** 1713–1717 (2000).

29.   Adams, N. M., Olmsted, I. R., Haselton, F. R., Bornhop, D. J. & Wright, D. W. The effect of hybridization-induced secondary structure alterations on RNA detection using backscattering interferometry. *Nucleic Acids Res.* **41,** e103 (2013).

30.   Cuervo, A. *et al.* Direct measurement of the dielectric polarization properties of DNA. doi:10.1073/pnas.1405702111

31.   von Ahsen, N., Oellerich, M. & Schütz, E. Use of two reporter dyes without interference in a single-tube rapid-cycle PCR: alpha(1)-antitrypsin genotyping by multiplex real-time fluorescence PCR with the LightCycler. *Clin. Chem.* **46,** 156–61 (2000).

32.   Kussrow, A. *et al.* The potential of backscattering interferometry as an in vitro clinical diagnostic tool for the serological diagnosis of infectious disease. *Analyst* **135,** 1535–7 (2010).

Chapter 4

Potassium Ionophore studies with BSI and evaluation of FreeSRF in nonaqeuous, small molecule, ion-recognition systems

4.1. Introduction

Most BSI experiments measure large molecule interactions, such as proteins or DNA with a ligand, but these interactions are driven by many smaller interactions, such as hydrogen bonds or ion interactions. Such interactions have been measured in a myriad of systems using several techniques, including NMR,[1] fluorescence,[2] and calorimetry.[3] As previously discussed, BSI offers several advantages to these techniques, including its small sample size and ability to perform binding assays in free solution. Additionally, with the development of the FreeSRF expression, the source of the BSI signal has been described in terms of conformational and solvation changes of the product or complex of the binding interaction.[4] This has only been done, however, with large biomolecular systems. Smaller binding systems with organic molecules would have a much smaller conformational change, but have been shown to still produce a measurable signal.[5] Therefore the experiments in this chapter were designed to measure the BSI signal in small ion-recognition systems in nonaqaueous media in order to compare the signal in systems with large conformational and solvation changes (ΔR_{gyr} and $\Delta SASA$) to those in small, organic molecule systems. The first experiment involved a very well-characterized system, a crown ether with potassium ion, and subsequent systems featured three different potassium ionophores.

4.1.2. Metal Complexes with Crown Ethers

Crown ethers are a class of cyclic polyethers whose abilities to form stable complexes with various cations, depending on the size of the crown and the cation, were first discovered by C. J. Pedersen in 1967.[6] He first noticed a small amount of white, crystalline byproduct in a preparation of bis[2-(*o*-hydroxyphenoxy)ethyl]ether contaminated with a small amount of catechol. The cyclic polyether was coined dibenzo-18-Crown-6 and was found to form stable 1:1 complexes with several alkali and alkali-earth metal salts. Pedersen continued this research with both known and novel cyclic polyethers to demonstrate a wide variety of crown ethers and compare their complexing properties. Selectivity is based on the size of the cation and the size of the cavity in the crown ether; affinity is based on the coplanarity of the crown, the number of oxygen atoms in the ring, and the distance between each of those oxygen.
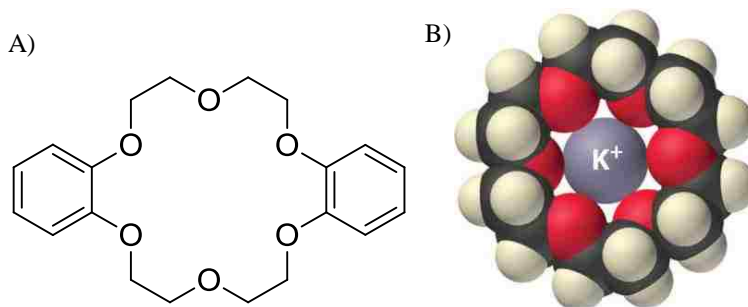
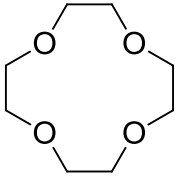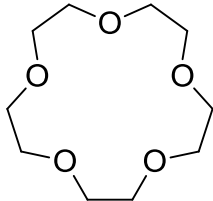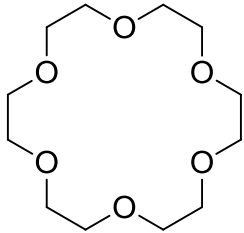**Figure 4.1.** A) Dibenzo-18-Crown-6, B) Complex of 18-Crown-6 and K$^+$.[7]

Pedersen coined the shortened "crown" names based on their ability to "crown" the cation with the oxygen in the ring in an ion-dipole interaction as shown in Figure 4.1, with the first number indicating the total atoms in the polyether ring, and the second indicating the number of oxygen atoms in the ring. For example, the compound with the

standard IUPAC name 1,4,7,10,13,16-hexaoxacyclooctadecane is referred to as 18-Crown-6 (18C6). Table 4.1 lists the three simplest crown ethers and the cation for which they have the highest affinity.

Table 4.1. Crown ether structures and coordinating cation.

Structure			
Name	12-Crown-4	15-Crown-5	18-Crown-6
Selecive Cation	Li^+	Na^+	K^+

Since Pedersen's discovery of their unique binding properties, crown ethers' chemistry and applications have become an important area of research. Saturated crown ethers are able to solubilize inorganic salts in aromatic hydrocarbon solvents such as benzene and toluene, making them useful phase transfer catalysts and ion-selective electrodes (ISEs).[8–10] The fields of molecular design and host-guest chemistry developed out of crown ether research, and other molecular families such as calixarenes and cryptands were introduced as a result.[11] Crown ethers, as well as other host-guest receptors, can also serve as synthetic ionophores for membrane transport, mimicking the function of natural ionophores in cells.

4.1.3. Valinomycin as a Potassium-selective Ionophore

An ionophore is a compound that selectively and reversibly binds a cation for transport through hydrophobic media; for naturally-occurring ionophores this includes cell transport through membranes or liposomes. Valinomycin (Vm) is one such ionophore that is highly selective for potassium over sodium in Streptomyces bacteria. It is a dodecadepsipeptide that contains three oligomers of L-valine (L-Val), D-α-hydroxyisovaleric acid (D-Hv), D-valine (D-Val), and L-lactic acid (L-Lac), shown in Figure 4.2.
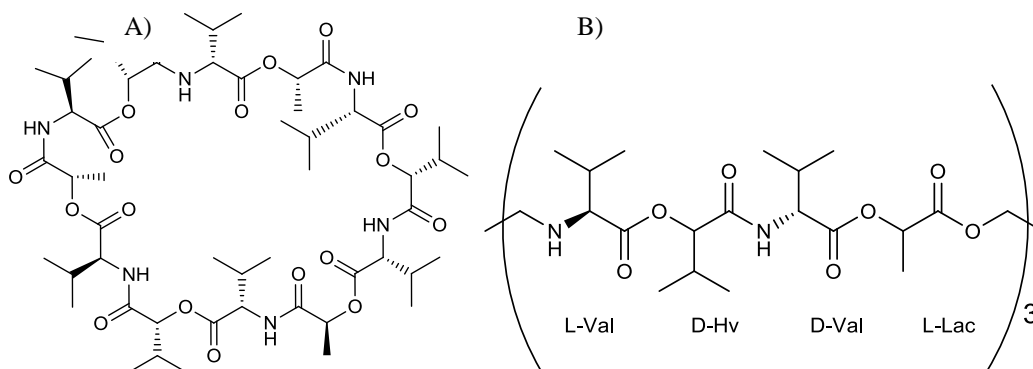
Figure 4.2. A) Valinomycin structure. B) Repeating depsipeptide component that produces the cyclic Valinomycin structure.

Many studies have been performed to study the structure of free and complexed Valinomycin since its discovery in the 1960s, using NMR, Raman spectroscopy, computer simulations, and more.[12–15] Like the crown ethers, the cavity is one of the main factors in its ion selectivity for potassium, which has a radius of ca. 1.33 Å, however, complexes with other cations have been observed, occasionally with stoichiometries of 1:2 or 2:1 and different conformations.[16,17] Additionally, the structure of free valinomycin has shown a large degree of solvent dependence, based on solvent polarity and hydrogen bonding.[14,18] Upon binding, the valinomycin-potassium complex takes on

a "tennis ball seam" conformation as shown in Figure 4.3 regardless of solvent effects. The six ester carbonyls point into the cavity to bind the potassium ion, and the amide hetero atoms of the amides stabilize the conformation through intramolecular hydrogen bonds.
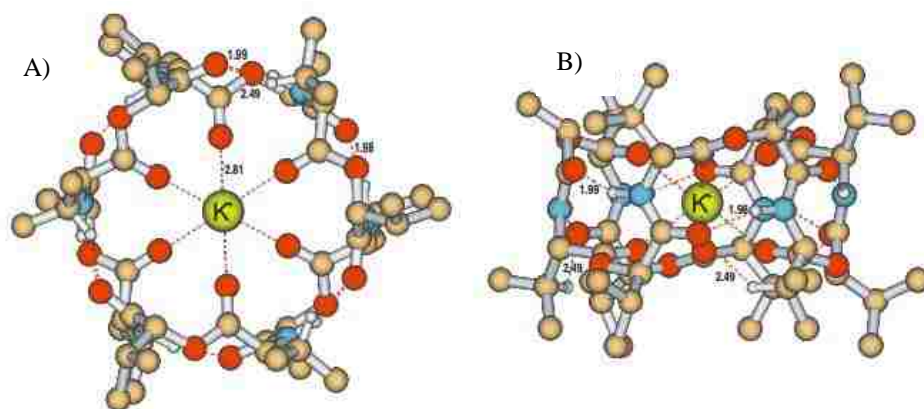
Figure 4.3. Structure of valinomycin-K$^+$ complex from DFT simulations viewed from A) above and B) side. Hydrogen atoms are omitted except those taking part in internal hydrogen bonds (distances labeled in Å).[19]

Valinomycin acts as a potassium ionophore based on its ability to form a lipid-soluble complex due to the hydrophobic methyl and isopropyl groups facing outwards from the cavity (as seen in Figure 4.3). The complex is unstable in hydrophilic or aqueous environments, so the ion is released once the complex crosses the membrane.[14,20] This function gave rise to several synthetic ionophores which behave similarly, most often for use in ISEs, and valinomycin is also known as Potassium Ionophore I.

4.1.4. Bis(crown ether) ionophores

Pedersen's discovery of the crown ethers' complexation abilities and Valinomycin's conformational changes upon complexation motivated scientists to develop other types of selective ionophores, of which one group of compounds was

developed known as bis(crown ether)s.[21,22] Bis(crown ether)s feature two crown ether

moieties connected by an alkyl chain. They form an intramolecular complex with a

cation by sandwiching it between the two crown ether faces; this complex has been

likened to a clamshell. An example is shown in Figure 4.4A.
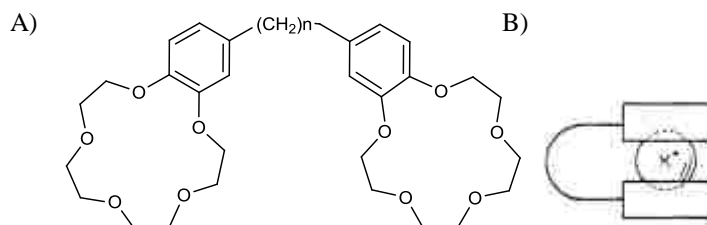
Figure 4.4. (A) Representative bis(benzo-15C5), and (B) diagram of the "closed clamshell" complex with potassium.[21]

Inoue and coworkers developed a series of bis(benzocrown ether)s to examine

this complexation and noted that in many cases the internal "1:2" complexation of the

cation to both crown ether ends was more stable than the mono crown ether.[21,23] The ion

complexing with two crown ethers also meant that different sized crown ethers fit a

cation compared to the mono crown ether; in the case of potassium ion, the 1:2 complex

that fits best is made of two 15-crown-5 moieties. They also noted that the linker length

affected complex stability. Too short a chain resulted in an "open clam" complex that

had incomplete desolvation of the potassium ion, and too long a chain resulted in greater

degrees of freedom in the chain and complex conformation.[21]

Other researchers such as Tóth and coworkers modified bis(benzo crown ether)s

for improved ISEs by adding alkyl chains to the linker and electron withdrawing groups

to the benzyl groups. These modifications produced improved stabilities with the

electrode membranes and increased selectivity for potassium over sodium.[22] While the

complexation between cation and crown ether oxygen for these types of bis(benzo crown

ether)s is analogous to the mono crown ethers that Pedersen studied, thermodynamic studies showed that these ionophores undergo a more significant conformational change upon complexation similar to valinomycin.[23]

4.1.5. Previous nonaqueous, small molecule experiments with BSI

To determine if BSI free-solution measurements could be extended to nonaqueous, small molecule interactions, experiments were designed to measure hydrogen bonding affinities between tetramethylammonium benzoate (TMAB) and 1,3-diphenyl urea (DPU), 1,3-diphenylthiourea (DPTU), 1,3-bis(p-nitrophenyl)urea (DNPU) and 1,3-bis(p-nitrophenyl)thiourea (DNPTU).[5] These compounds were chosen based on their well-characterized ability to form strong hydrogen bonds, an example of which is shown in Scheme 4.1, as well as their utilization in organic reactions.[24,25]
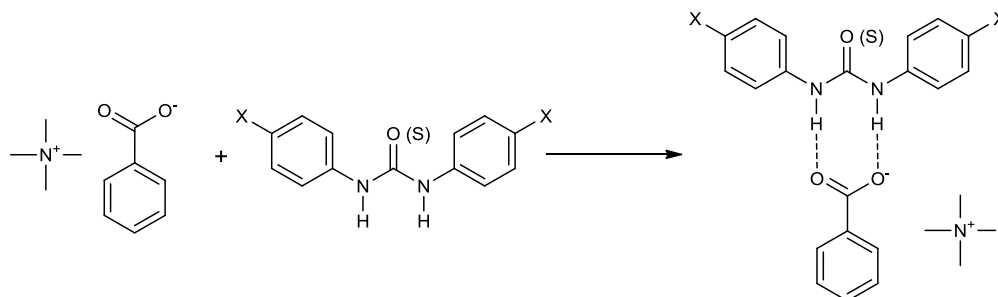
Scheme 4.1. Hydrogen bonding between DPU/DPTU (X = H) or DNPU/DNPTU (X = NO$_2$) and TMAB.

The *para*-substituted nitro groups on the phenyl rings in DNPU and DNPTU serve to draw electron density away from hydrogen, increasing their acidity and resulting in a stronger hydrogen bond.

Acetonitrile (MeCN) was chosen as the solvent for two main reasons: 1) it can readily dissolve the chosen compounds at concentrations necessary for benchmarking with ITC (mM range), and 2) its RI is close to H$_2$O (η = 1.342 and 1.332, respectively).

The RI of the solvent must not be too close to that of the glass used in the microfluidic chip ($\eta = 1.517$) in order to generate a high-contrast fringe pattern, for example, DMSO's RI of 1.476 is too close to generate an acceptable fringe pattern.

BSI results are summarized in Table 4.2.[5] Results correlated well with ITC experiments. Additionally, they indicated little difference between ureas and thioureas, and a stronger binding affinity between the *para*-nitro-substituted compounds than the unsubstituted as expected (K_D's of 0.54 and 0.42 μM vs 18.56 and 23.20 μM).

Table 4.2. BSI and ITC results of TMAB complexes with ureas and thioureas.[5]

TMAB Complex	BSI K_D (μM)	ITC K_D (μM)
DPU	18.56 ± 4.46	21.75 ± 6.04
DPTU	23.20 ± 4.55	27.43 ± 3.72
DNPU	0.54 ± 0.08	1.26 ± 0.06
DNPTU	0.42 ± 0.08	1.18 ± 0.17

The ability to perform nonaqueous experiments meant that entire new groups of systems could be studied with BSI. No conformational change occurs between TMAB and DPU (and others) when the two hydrogen bonds are formed; solvation effects, specifically the displacement of solvent molecules during hydrogen bond formation, are the main contributors to the BSI signal. Unsurprisingly, the magnitude of the signal is much smaller compared to those from larger, biomolecular systems such as protein-ligand or DNA duplexes.

4.1.6. Designing BSI experiments for metal ion recognition

Host-guest recognition systems such as the crown ethers and other ionophores represent another type of binding with small molecules that we hypothesized could be observed via BSI. 18C6 complexing with potassium would not be expected to undergo a

significant conformational change, but ionophores like the bis(benzocrown ether)s undergoe a conformational change to form the "closed-clam" complex in a way that mimics some larger systems, such as calcium-CaM binding to a ligand (recall Figure 1.14C). Comparing the resulting signals from BSI experiments with 18C6 and other ionophores could provide more insight into the source of the BSI signal, particularly for small molecule systems where conformational changes might not have as large an impact as they do in large biochemical systems.

4.1.7. Expanding the FreeSRF expression into nonaqueous, small molecule systems

Thus far the systems evaluated with the FreeSRF expression featured large biomolecules and their ligands, which undergo significant conformational changes upon binding.[4] The hydrogen-bonding systems examined previously with BSI demonstrated that a measurable binding signal can be obtained even for small molecule systems that lack the molecular weight and large conformational changes seen in the biochemical systems. The signal from the TMAB-DPU systems was hypothesized to arise from solvation changes as the hydrogen bonds form. Signals arising from the ion-recognition systems would also be expected to have a larger impact from solvation compared to biomolecular systems. Signal changes in these smaller systems could be analyzed to refine the FreeSRF expression for small organic molecules.


4.2 Materials and Methods

4.2.1. Instrument and chip preparation

The instrument was equilibrated for at least one hour prior to experiments. The temperature-controlled stage was held at 25 °C. The microfluidic chip (210 μm diameter

channels) was used with no silanization or other surface treatment. Channels were rinsed

with MeCN after each experiment, and after all three channels were used (typically 5-7

trials per channel), they were filled with H_2O and sonicated for 30-40 min, then rinsed

with H_2O and MeCN, vacuumed dry, and secured in the stage.

4.2.2. Preparation of samples

Four ionophore receptors were used in this study: 18-Crown-6 (18C6), Potassium

Ionophore I (or Vm), Potassium Ionophore II (Figure 4.5A), and Potassium Ionophore III

(Figure 4.5B), all obtained from Sigma-Aldrich. The salt used for each ionophore was

potassium iodide (KI) due to its higher solubility in MeCN than other potassium salts

such as KBr or KCl. Sodium iodide (NaI) was also used with 18C6 to observe the

difference between a high-affinity ion and a low-affinity ion.
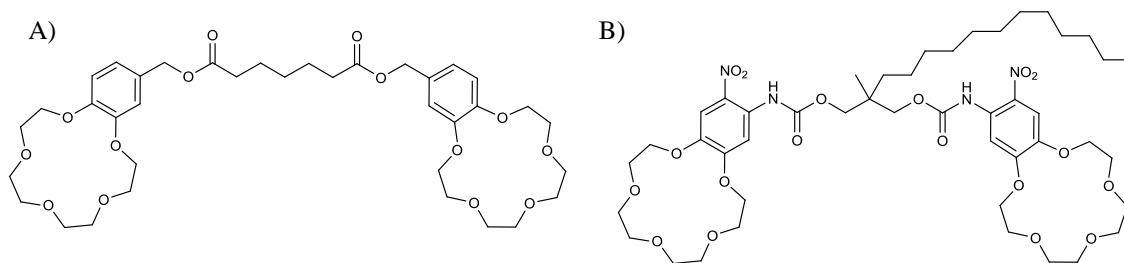
Figure 4.5. A) Potassium Ionophore II and B) Potassium Ionophore III

Ionophores II and III, 18C6, and KI were dried under vacuum overnight before

dissolving in MeCN. The initial KI solution and Ionophore III solution were each

sonicated for ca. 5 min to ensure complete dissolution. Stock Vm solutions were stored

in a refrigerator at 4 °C. KI and NaI stock solutions and BSI samples were kept covered

with foil to prevent light-induced decay of iodide.

In each BSI experiment, the ionophore acted as the receptor and was held at a constant concentration while KI was the ligand with varied concentrations. Concentration ranges were determined based on ITC K_a results.

4.2.3. ITC Experiments

For the ionophore experiments, both the reference and sample cells were rinsed three times then filled with degassed MeCN. The syringe was rinsed with degassed MeCN by drawing liquid through the mixing needle. Blank trials were performed to subtract any significant heats of dilution from the binding heats.

For all ITC experiments, the reference power was set to 20 µCal/sec and the cell temperature to 25 °C. 25-30 injections of 10.0 µL each were performed with a spacing of 360 sec (later reduced to 180 sec). 10.00 mM 18-Crown-6 was titrated into 1.00 mM KI. Potassium Ionophore II experiments were conducted at the same concentrations as 18C6. Potassium Ionophore III is less soluble in MeCN compared to 18C6 and Ionophore II, so 2.0 mM KI was titrated into 0.2 mM Ionophore III. Potassium Ionophore I also used 2.0 mM KI titrated into 0.2 mM Ionophore due to a more exothermic interaction compared to the other ionophores. Binding isotherms were fit using Origin software to obtain the stoichiometry, K_a, ΔH, and ΔS.

4.2.4. BSI Data Collection

For each BSI experiment, the ionophore was held at a constant concentration while the concentration of KI was varied, and KI reference samples were subtracted to obtain the binding curve. Samples were prepared in glass vials and allowed to equilibrate for ca. 30 minutes, and were kept covered with foil when not running experiments. Concentration ranges were determined based on the ITC K_D values. 18C6 and Ionophore

II were set to 7.5 µM with KI (or NaI) going up to 10 µM. Ionophore III was held at 1.5 µM with KI going up to 2.5 µM. Ionophore I was held at 100 nM with KI going up to 300 nM. The channels of the glass chip were not silanized. The injection volume for each experiment was increased to 2.00 µL. Data were collected for ca. 15-20 sec; the shorter collection time and larger volumes were due to MeCN's much faster evaporation rate compared to aqueous systems that would cause greater signal drift.

4.2.5. BSI Data Analysis

As described in previous sections (2.2.4 and 3.2.4), binding curves were plotted as a function of phase shift versus ligand (ion) concentration in Excel, and a K_D was calculated from the one-site rise to max binding hyperbola equation using Solver. Error in K_D was determined using a solver macro. FreeSRF χ_{exp} values were calculated as previously determined (3.3.3). χ_{model} values were calculated as described by Bornhop and coworkers using the following equation:[4]

$$\chi_{model} = A(\Delta SASA) + B(aveSASA) + C(\Delta R_{gyr}) + D(aveR_{gyr}) + E \qquad (1)$$

Where *A, B, C, D*, and *E* are the small training set fitting coefficients, $\Delta SASA$ is the change in solvent accessible surface area between bound and free receptor, *ave*SASA is the average SASA of bound receptor (in the case of some larger systems with minor changes between structures; for the ionophores only one structure was used), ΔR_{gyr} is the change in radius of gyration between bound and free ionophore and $aveR_{gyr}$ is the average radius of gyration of bound receptor. R_{gyr} was determined for all structures with a Chimera script, and SASA was found for all structures using MGLtools. Structures for the free ionophores were put into Chimera using their SMILES code, structures for bound 18C6 and ionophore I were obtained from the Cambridge Crystallographic Database, and

the structure of bound ionophore II was built using Gaussian and previously calculated strontium ionophores.

4.3. Results and Discussion

4.3.1. ITC Results

The binding data for each ionophore with KI are shown in Figures 4.6-4.9. The K_D values were calculated as $K_D = 1/K_a$.
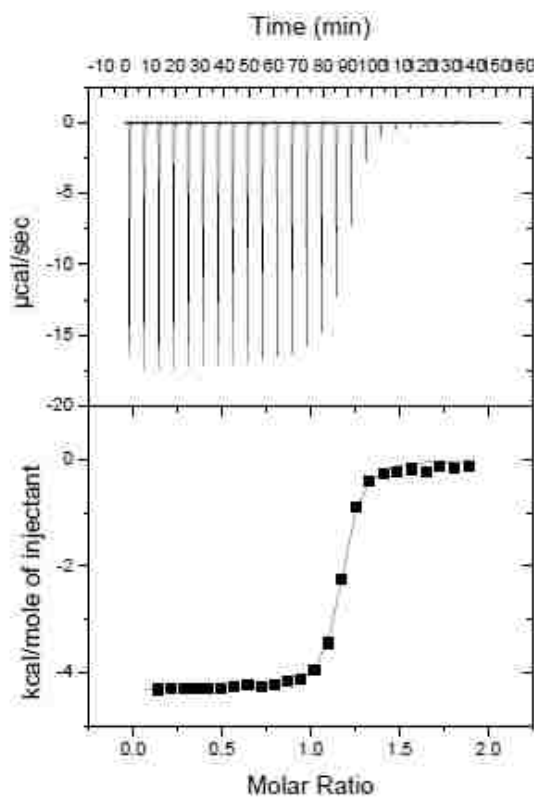
Figure 4.6. ITC curve of 10.00 mM 18C6 into 1.00 mM KI. The average K_D from three replicate experiments was 2.35 $\pm$ 0.11 μM, and ΔH = -4389 $\pm$ 56 kcal/mol, ΔS = 11.0 $\pm$ 0.2 cal/molK.
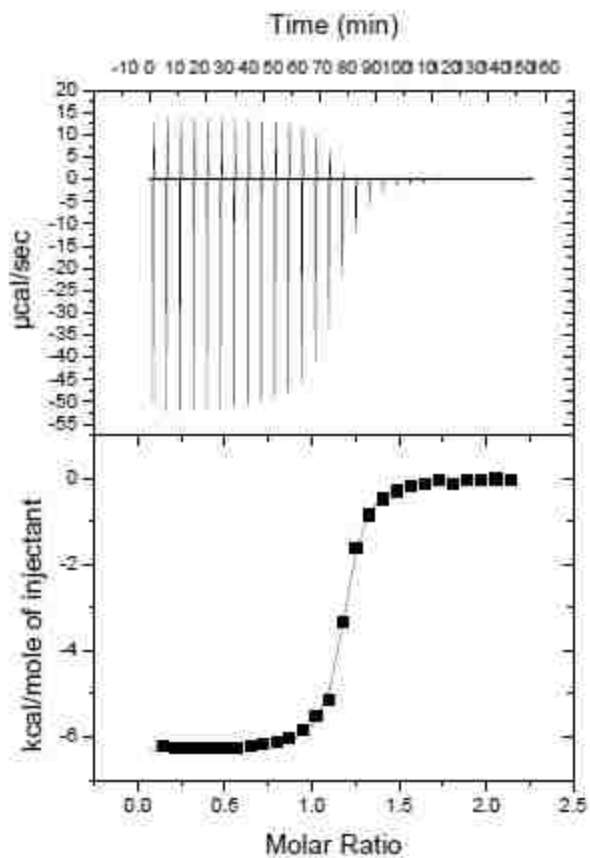
Figure 4.7. ITC curve of 10.0 mM Potassium Ionophore II into 1.00 mM KI. The average K_D from three replicate experiments was 2.81 ± 0.29 µM, and $\Delta H = -6183 \pm 88$ kcal/mol, $\Delta S = 4.65 \pm 0.41$ cal/molK.
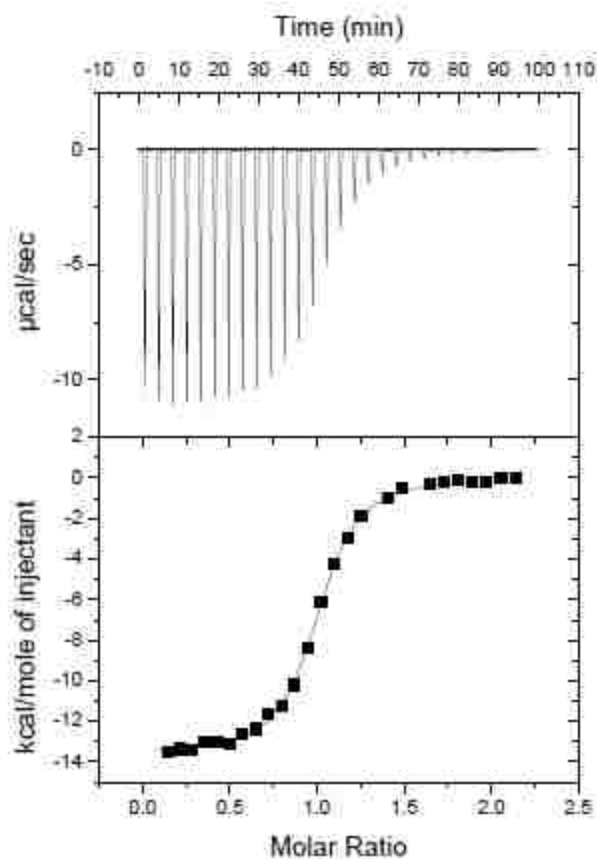
Figure 4.8. ITC curve of 2.0 mM KI into 0.2 mM Potassium Ionophore III. The average K_D from three replicate experiments was 2.42 $\pm$ 0.21 μM, and ΔH = -13893 $\pm$ 615 kcal/mol, ΔS = -20.9 $\pm$ 2.1 cal/molK.
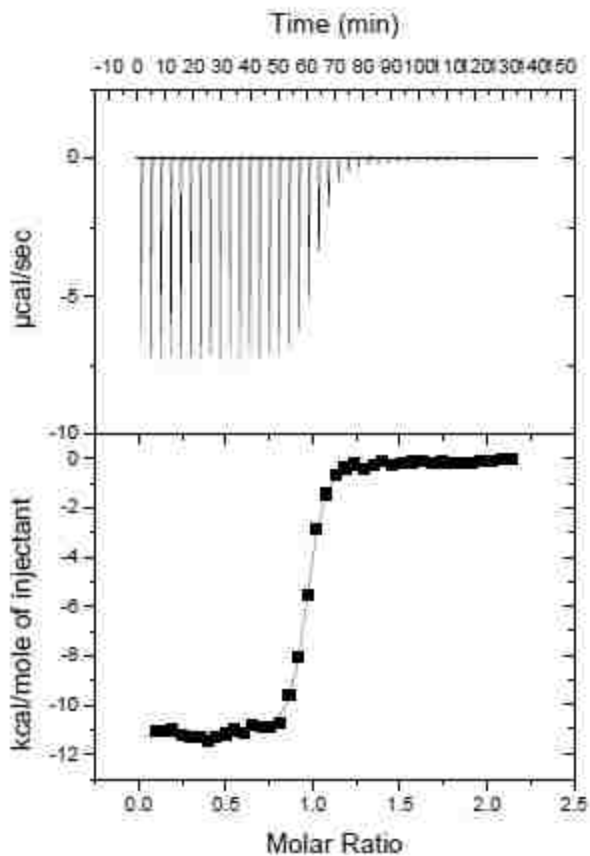
Figure 4.9. ITC curve of 2.0 mM KI into 0.20 mM Potassium Ionophore I. The average K_D from three replicate experiments was 0.374 ± 0.074 µM, and $\Delta H = -11057 \pm 378$ kcal/mol, $\Delta S = -7.64 \pm 1.2$ cal/molK.

4.3.2 BSI Binding Results

The binding curves for the ionophores with KI are shown in Figures 4.10-4.13. All except Potassium Ionophore III had a single rise-to-max curve in the negative direction. The binding curve for 18C6 with NaI is shown in Figure 4.14. 18C6 has a much weaker affinity for Na^+ compared to K^+ due to its smaller ionic radius.

117
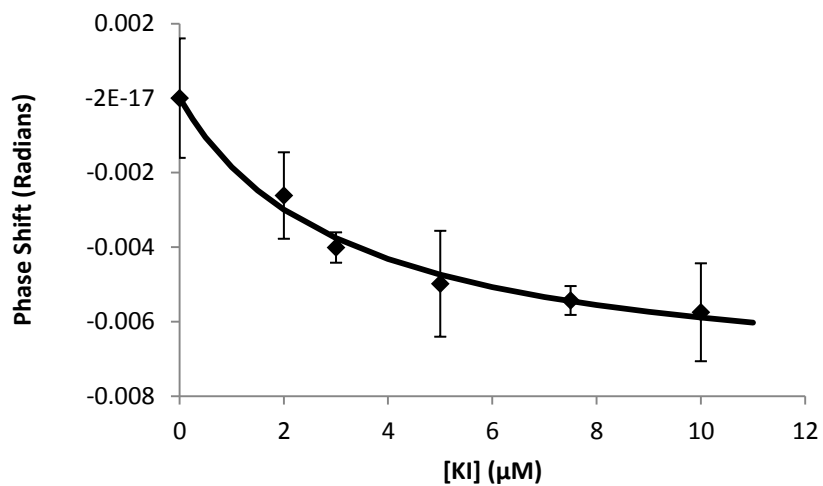
Figure 4.10. BSI binding curve of 18C6 with KI. [18C6] = 7.5 μM, and [KI] ranged from 0 – 10 μM. K_D = 3.20 $\pm$ 0. 69 μM, B_{max} = 7.78 mRad.
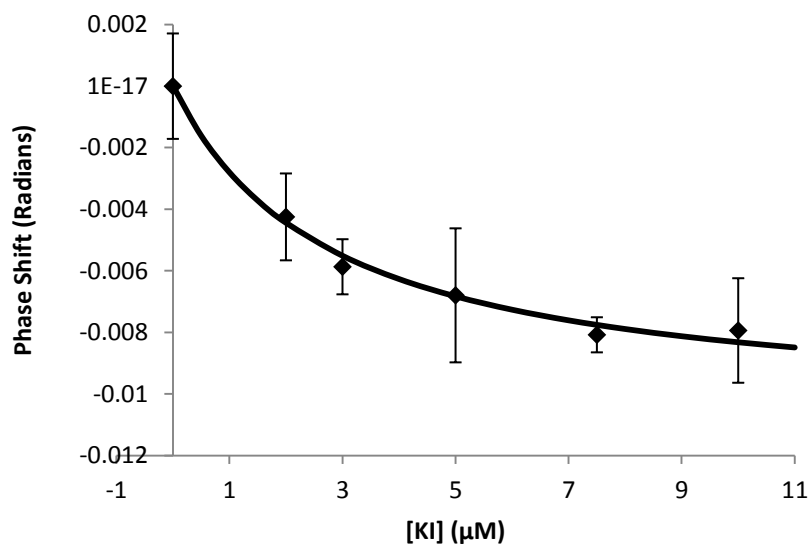
Figure 4.11. BSI binding curve of Potassium Ionophore II with KI. [Ionophore] = 7.5 μM, and [KI] ranged from 0 – 10 μM. K_D = 2.79 $\pm$ 0. 51 μM, B_{max} = 10.7 mRad.
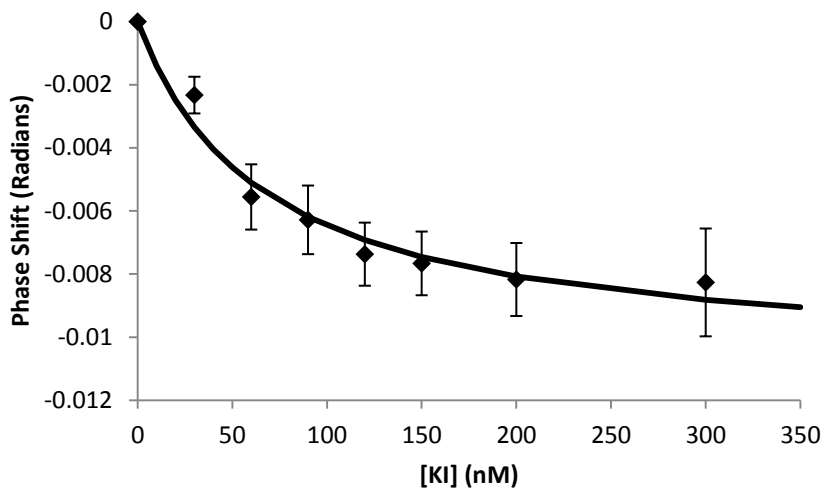
Figure 4.12. BSI binding curve of Potassium Ionophore I (Vm) with KI. [Ionophore] = 150 nM, and [KI] ranged from $0 - 300$ nM. $K_D = 66.7 \pm 16.4$ nM, $B_{max} = 10.8$ mRad.
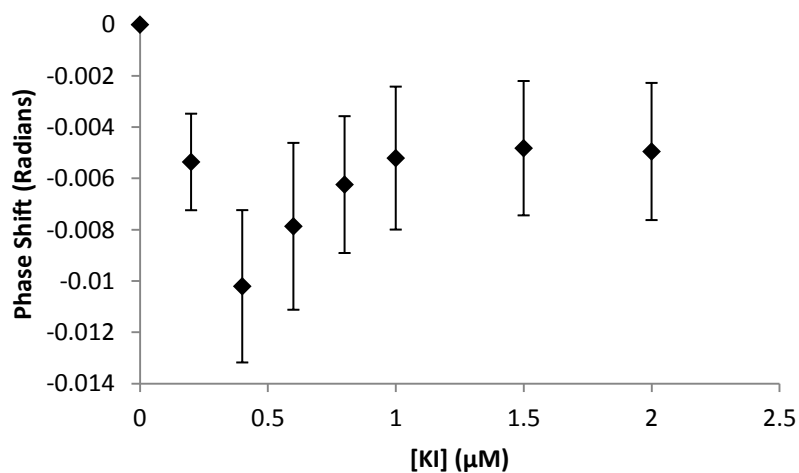
Figure 4.13. BSI binding curve of Potassium Ionophore III with KI. [Ionophore] = 1.5 µM, and [KI] ranged from 0 - 2.5 µM. Treating the positive binding curve portion as an isolated curve gives a $K_D = 0.279$ µM and a B_{max} of 6.60 mRad.
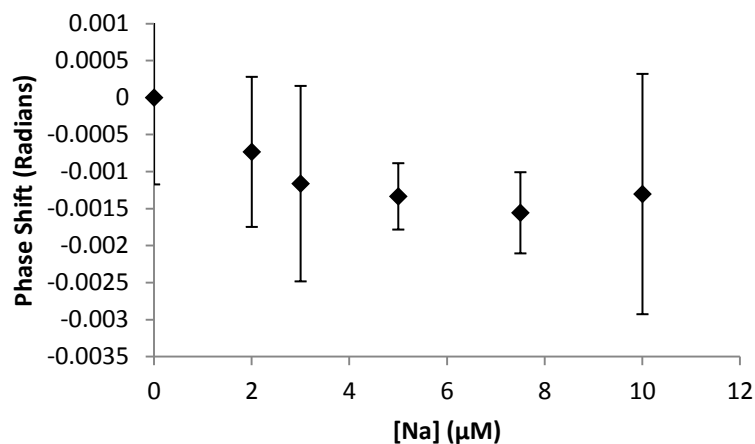
Figure 4.14. BSI binding curve of 18C6 with NaI. Very little signal above the noise level is observed, too little to calculate a possible K_D.

4.3.3. Comparison of Signal Magnitude

The signal generated from these small molecule interactions is significantly smaller than those generated from binding of larger, biomolecular systems. The signal of the Valinomycin-potassium binding curve was more than an order of magnitude smaller than the complementary dsDNA binding featured in Chapter 3, and both experiments were run at similar concentration ranges of both receptors and ligands (< 300 nM). Figure 4.15 features both of these curves to highlight the powerful sensitivity of BSI to detect these small-molecule interactions.
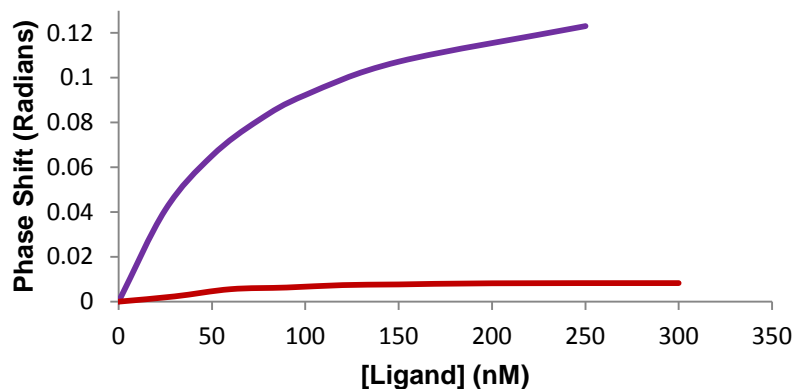
Figure 4.15. BSI binding curves of complementary dsDNA (violet) and VmK$^+$ (red) (phase shifts are absolute value since these systems featured signals in opposite directions.)

When comparing the binding curves of 18C6 with potassium and sodium at the same concentrations in Figure 4.16, a significant difference in the signal magnitude is observed, specifically, the signal from sodium-18C6 complex is barely above the noise limit of the instrument. A sodium ion's radius is ca. 0.4 Å smaller than potassium's, making it too small to fit in the crown cavity (it is a much better fit for 15C5), so only a very weak interaction can be detected.
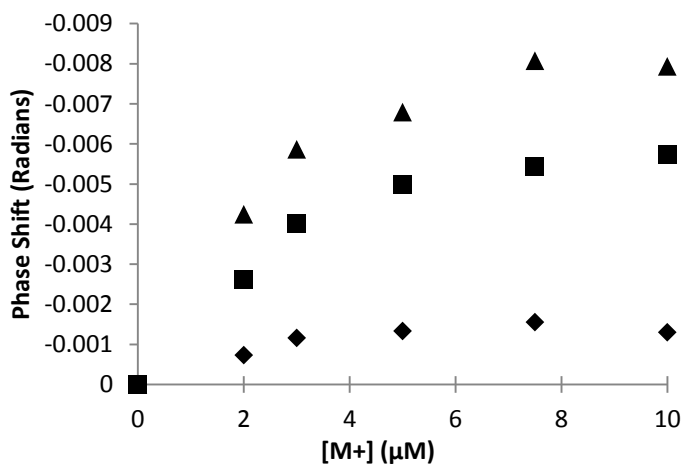
Figure 4.16. BSI binding data of Na$^+$ with 18C6 (♦), K$^+$ with 18C6 (■), and K$^+$ with ionophore II (▲). [18C6] and [ionophore II] = 7.5 μM.

121

Both 18C6 and Potassium Ionophore II had very similar affinities for K^+ (3.20 and 2.79 μM respectively) and ITC data correlated well with these values. Their signal magnitudes, however, were very different, as highlighted in Figure 4.15. From the rise-to-max equations, the B_{max}, or maximum signal generated, is 10.7 mRad for Ionophore II and 7.78 mRad for 18C6. This is a percent difference of 31.6%. The FreeSRF expression describes the source of the BSI signal as deriving from conformational changes and changes in solvation. Based on this, the differences in the signal magnitude of potassium binding to 18C6 or to Ionophore II can be explained.

Unbound 18C6 has been shown to take on slightly different conformations depending on potential interactions with solvent.[26] In polar protic solvents, including water, its conformation is more constrained due to hydrogen bonds with the ether oxygen, and it tends to take on the D_{3d} conformation. Conversely, in aprotic solvents like MeCN, it is more flexible and can adopt other conformations, with C_i or S_6 being computationally the lowest energy conformations.[26] Some of the lowest calculated energy conformations of free 18C6 are shown in Figure 4.17.
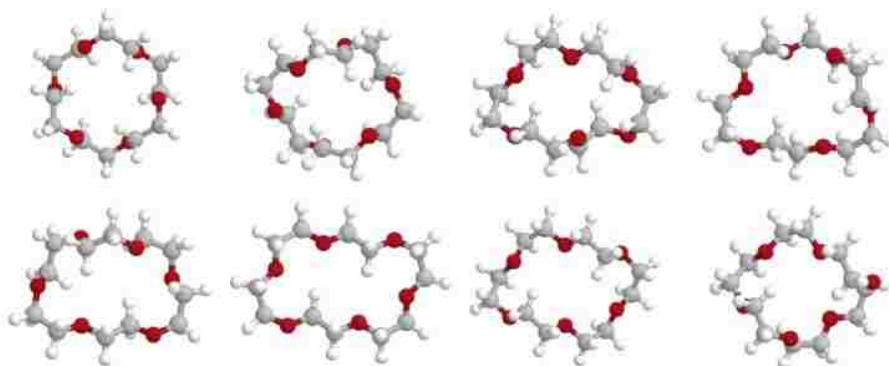
Figure 4.17. Structures of calculated lowest-energy conformations of free 18C6.[26]

When bound to the potassium ion, 18C6 tends to take on a D_{3d} conformation.[27] Comparing this structure to the S_6 and C_i conformations, as shown in Figure 4.18, allows one to visualize the relatively minor conformational changes that occur upon binding to the metal ion.
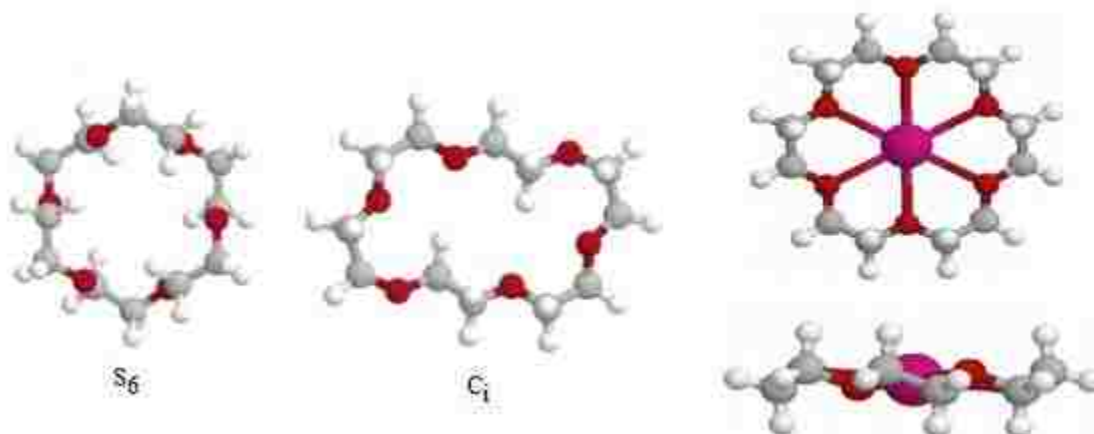
Figure 4.18. Free 18C6 in the S_6 and C_i conformation compared to a top and side view of 18C6-K^+ complex (D_{3d} conformation).[28]

Regardless of the conformation of the free crown, only a modest conformational change occurs upon binding, and the BSI signal is smaller as a result. The conformational change that occurs when ionophore II binds to potassium to form the closed-clam structure produces a larger BSI signal, even when both receptors have very similar affinity for potassium ion.

Figure 4.19 compares the signals of ionophore II and ionophore I (Vm). Ionophore I had a significantly stronger affinity for potassium ion (66.7 nM vs. 2790 nM), but when plotting the signal phase shift as a function of molar ratio of potassium to ionophore, their resulting signals were very similar in magnitude, with a B_{max} of 10.7 and 10.8 mRad and a percent difference of less than 1%. Both undergo significant conformational changes upon binding, with ionophore II forming the closed clam shell

around the ion, and ionophore I forming the tennis-ball seam around the ion. This comparison highlights how BSI signal is affected by intrinsic structural changes (χ) and not simply strength of the interaction.
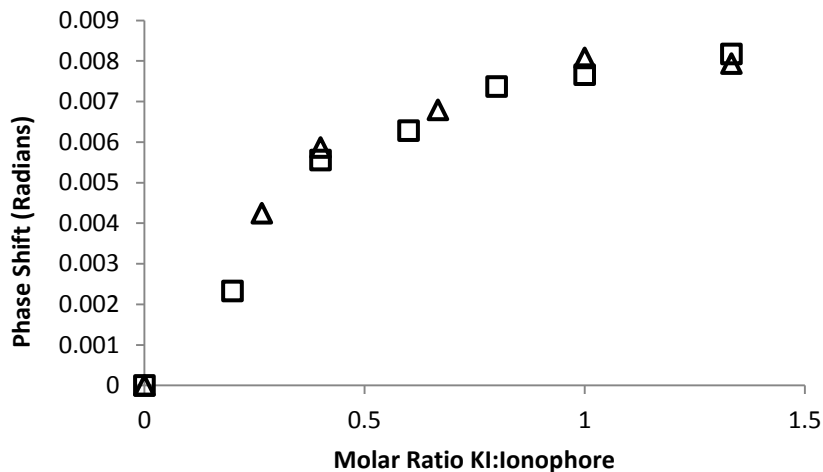
Figure 4.19. BSI binding curves of phase shift vs molar ratio of K^+ for ionophore II (Δ) and ionophore I ($\square$).

18C6, ionophore I, and ionophore II binding to potassium all featured a negative phase shift relative to the instrument's alignment (rotating the camera $180°$ will reverse the signal direction). The direction of the BSI signal is related to a decrease or increase in optical density, and thus RI. In the present set-up used in this thesis, a negative signal correlates to an increase in optical density and RI, while a positive signal is due to a decrease in RI, thus each of these ionophores have an overall positive ΔRI upon binding with potassium ion.

4.3.4. Evaluation of FreeSRF in small molecule, nonaqueous systems

As with the DNA systems, χ_{exp} was calculated for the potassium complexes of 18C6, ionophore II, and ionophore I from the maximum signal, B_{max}, the concentration of

the complex, and β, the instrument response function of our instrument, according to the FreeSRF expression discussed in Chapter 1.4.2. and shown below.

$$\rho = \chi\beta C \qquad (1)$$

Next, χ_{model} was calculated for each potassium complex using the smaller training set coefficients determined by Bornhop and coworkers.[4] The results are summarized in Table 4.3.

Table 4.3. χ values and FreeSRF parameters for potassium complexes of 18C6 and ionophores I and II.

	Potassium Complex		
	18C6	**Ionophore I**	**Ionophore II**
ΔRgyr (Å)	-0.302	-0.416	-0.349
ΔSASA (Å^2)	1.17	27.06	-61.931
χmodel (RIU/M)	-616.67	-541.10	-560.13
χexp (RIU/M)	1.09	75.48	1.49
[Complex]	7.5 µM	150 nM	7.5 µM

There was very poor agreement between χ_{exp} and χ_{model}, however, the difference between χ_{exp} of ionophore I and 18C6 is 74.4 RIU/M and the difference between χ_{model} of ionophore I and 18C6 is 75.6 RIU/M, remarkably good agreement. This initial observation encouraged us to calculate a pseudo-structure for bound ionophore II, as a crystal structure was unavailable in the literature. The structure is shown in Figure 4.20.
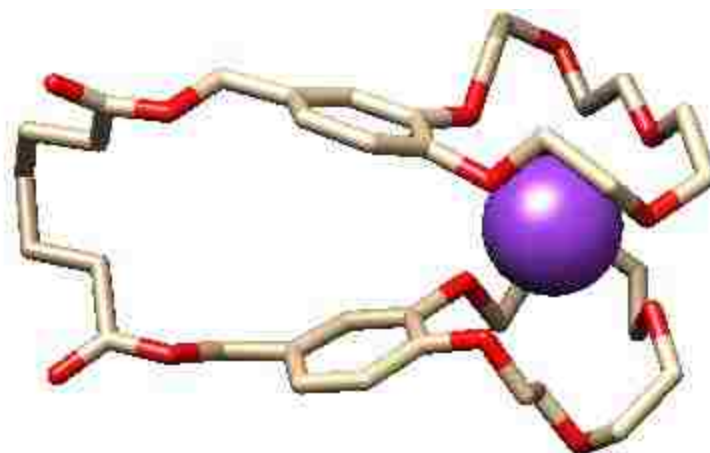
Figure 4.20. Modeled structure of bound potassium ionophore II (oxygen in red, hydrogen not shown).

This structure provided the calculations for R_{gyr} and SASA, and while its χ_{model} did not match up in the way that the difference between ionophore I and 18C6 complexes did, it was still between the two values. The differences are highlighted in the number line in Figure 4.21.

Figure 4.21. Depiction of differences between experimental and modeled χ values when both 18C6 experimental and modeled are zeroed.

The differences can likely be explained by the model coefficients A-E, which were all determined using large biochemical systems in aqueous media. With more training set systems similar to the non-aqueous small molecule ones, a new set of "extra small" coefficients could be determined via a regression analysis. Model structures of small organic molecules can be more easily analyzed and calculated compared to large biomolecules such as proteins or nucleic acids, which will allow for more thorough refinement of the FreeSRF expression.

4.3.5. Ionophore III signal changes

ITC data of potassium binding to ionophore III revealed that the binding affinity of ionophore III was similar to that of ionophore II, indicating that the hydrocarbon tail or the presence of the nitro groups had little effect on the strength of the potassium interaction with the crown moieties. The alkyl tail was included in this ionophore to help improve its stability in the electrode membranes in which they were designed to be used.[22] In contrast, however, the BSI binding data of potassium to ionophore III produced very different results compared to the other ionophores that generated a basic, hyperbolic binding curve, so it appears the inclusion of the hydrocarbon tail has a significant impact on the BSI signal.

Figure 4.13 shows the BSI binding data of ionophore III with potassium. An initial decrease in phase shift is observed of ca. 10 mRad. The signal then changes direction and saturates as a typical binding curve in the positive direction with a maximum signal of ca. 6.6 mRad above the minimum. The initial decrease thus has the largest signal change of the system, and occurs when $[K^+] = 0.400$ μM.

Gestwicki and coworkers used SPR experiments to correlate changes in RI to changes in hydrodynamic radius, specifically, an increase in hydrodynamic radius (R_h) resulted in an increase in RI, and a decrease in R_h resulted in a decrease in RI.[29] Based on this information, it appears the ionophore undergoes conformational changes upon binding to potassium ion that first increase its R_h but ultimately results in an overall decrease of R_h. Since this effect isn't observed in the other clamshell-binding ionophore II, the hydrocarbon tail of III is likely the source of the observed inconsistency.
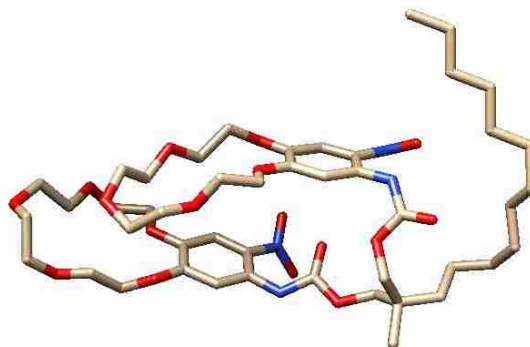
Figure 4.20. 3D Stick model of free potassium ionophore III, with carbons in tan, oxygens in red, and nitrogen in blue (hydrogen not shown).

The structure of unbound ionophore III is shown in Figure 4.20. Since the binding signal initially goes in the negative direction like the other ionophores, the conformational changes occurring begin with an increase in R_h, perhaps with the dodecyl tail being more extended from the crown ends. The difference with ionophore III, then, is that upon complexation and saturation with potassium, the bound form's conformational change results in a decreased R_h and RI, perhaps due to the dodecyl tail folding closer to the closed-clamshell crown ends. The signal does not saturate above the starting point of unbound ionophore III, so while binding seems to cause an initial increase (positive ΔRI) followed by a decrease in RI (negative ΔRI), the overall ΔRI is positive.

4.4. Conclusions

In its present design, BSI is capable of measuring binding of a metal ion to an organic ionophore molecule with signal changes that are more than an order of magnitude smaller than those observed for biochemical systems, less than 10 milliradians. Additionally, BSI was shown to detect selective ion-recognition, as 18C6 complex with sodium produced a signal barely above the noise of the data. BSI K_D values displayed excellent agreement with values determined via ITC for 18C6 and ionophore II. Despite having very similar affinities for potassium, ionophore II generated a 31.6% larger signal

128

than 18C6. Ionophore II forms a "closed clamshell" upon complexation with potassium, a conformational change that mimics some larger proteins' as they bind to a ligand, while 18C6's conformational change upon binding with potassium is smaller.

BSI K_D values for ionophore I were not in agreement with ITC, but this is likely due to the fact that the ITC experiments were run at 2.0 mM ionophore while BSI experiments were run at only 150 nM; this was the lowest concentration of ionophore used in this study, as ionophore I had a significantly higher affinity for potassium compared to the other ionophores. Ionophore I, also known as Valinomycin, contracts into a "tennis ball seam" conformation to accommodate binding to potassium, so that the six ester oxygen atoms are bound to the potassium ion inside the ionophore, while the outer surface remains hydrophobic. Considering the probe volume of the instrument (7.52 nL), at the lowest concentration of potassium added to the highest-affinity system, 30 nM with ionophore I, BSI's limit of detection was 136 million molecules.

This study paves the way for future small molecule or ion-recognition system studies, including potential environmental studies, for example targeting a specific metal ion in water samples. Small-molecule systems such as the ionophores discussed in this chapter also serve as an important starting point to continue to refine the FreeSRF expression, particularly for organic, nonaqueous systems.

These systems have the advantage of being simpler to model and calculate computationally for determining model χ values compared to large proteins or other biomolecules. An "extra small" training set can be developed from these studies to allow fitting coefficients A-E to be determined. Their small size and the potential to run identical experiments in various solvents allow for a more thorough understanding of the

role of solvation in the BSI signal to be acquired. Some systems, such as ionophore III, were shown to generate a more complicated binding curve rather than the typical one-site binding hyperbola. This could help give insight into the direction of the signal.

The signal direction has been related to increases or decreases in RI, specifically for the alignment of this instrument, a negative signal change corresponds to an increase in RI. Gestwicki and coworkers related this to an increase in R_h upon complexation.[29] Using bound and unbound structures of 18C6 and ionophores I and II, it was determined that all three featured a decrease in R_{gyr} upon complexing with potassium. R_h and R_{gyr}, while sounding similar, measure different aspects of a molecule or complex, with R_h taking into account the solvation sphere of the molecule in question, and R_{gyr} being a mass-weighted calculation. Differences in these values may provide additional insight into the source and direction of the BSI signal.

4.5. References

1.   Tárkányi, G., Király, P., Varga, S., Vakulya, B. & Soós, T. Edge-to-Face CH/π Aromatic Interaction and Molecular Self-Recognition in *epi* -Cinchona-Based Bifunctional Thiourea Organocatalysis. *Chem. - A Eur. J.* **14,** 6078–6086 (2008).

2.   Hoang, L., Bahmanyar, S., Houk, K. N. & List, B. Kinetic and stereochemical evidence for the involvement of only one proline molecule in the transition states of proline-catalyzed intra- and intermolecular aldol reactions. *J. Am. Chem. Soc.* **125,** 16–7 (2003).

3.   V. D. J. & Schmidtchen, F. P. A Novel Synthesis of Chiral Guanidinium Receptors and Their Use in Unfolding the Energetics of Enantiorecognition of Chiral Carboxylates. (2007).

4.   Bornhop, D. J., Kammer, M. N., Kussrow, A., Flowers, R. A. & Meiler, J. Origin and prediction of free-solution interaction studies performed label-free. *Proc. Natl. Acad. Sci. U. S. A.* **113,** E1595–604 (2016).

5.   Pesciotta, E. N., Bornhop, D. J. & Flowers, R. A. Backscattering interferometry: an alternative approach for the study of hydrogen bonding interactions in organic solvents. *Org Lett* **13,** 2654–2657 (2011).

6.   Pedersen, C. J. Cyclic Polyethers and Their Complexes with Metal Slats. *J. Am. Chem. Soc.* **89,** 7017–7036 (1967).

7.   Interesting Alcohols, Ethers, and Epoxides. *UC Davis ChemWiki* (2016). Available at: http://chemwiki.ucdavis.edu/Textbook_Maps/Organic_Chemistry_Textbook_Maps/Map%3A_Organic_Chemistry_(Smith)/Chapter_09%3A_Alcohols,_Ethers,_and_Epoxides/09.5_Interesting_Alcohols,_Ethers,_and_Epoxides. (Accessed: 1st July 2016)

8.   Sheen, S.-R. & Shih, J.-S. Lead(II) ion-selective electrodes based on crown ethers. *Analyst* **117,** 1691 (1992).

9.   Javanbakht, M., Ganjali, M. R., Eshghi, H., Sharghi, H. & Shamsipur, M. Mercury(II) Ion-Selective Electrode Based on Dibenzo-diazathia-18-crown-6-dione. *Electroanalysis* **11,** 81–84 (1999).

10.   Kimura, K., Oishi, H., Miura, T. & Shono, T. Lithium ion selective electrodes based on crown ethers for serum lithium assay. (2002).

11.   Gokel, G. W., Leevy, W. M. & Weber, M. E. Crown Ethers: Sensors for Ions and Molecular Scaffolds for Materials and Biological Models. doi:10.1021/cr020080k

12.   Neupert-Laves, K. & Dobler, M. The Crystal Structure of a K+ Complex of Valinomycin. *Helv. Chim. Acta* **58,** 432–442 (1975).

13.   Huang, H. W. & Williams, C. R. Structure of valinomycin-K+ complex in solution by extended x-ray absorption fine structure. *Biophys. J.* **33,** 269–273 (1981).

14.   Forester, T. R., Smith, W. & Clarke, J. H. Molecular dynamics simulations of valinomycin and its potassium complex in homogeneous solvents. *Biophys. J.* **71,** 544–53 (1996).

15.   Ehala, S., Kašička, V. & Makrlík, E. Determination of stability constants of valinomycin complexes with ammonium and alkali metal ions by capillary affinity electrophoresis. *Electrophoresis* **29,** 652–657 (2008).

16.   Devarajan, S., Nair, C. M. K., Easwaran, K. R. K. & Vijayan, M. A novel conformation of valinomycin in its barium complex. *Nature* **286,** 640–641 (1980).

17.   Sankaram, M. B. & Easwaran, K. R. Solution conformations of valinomycin-divalent cation complexes. *Int. J. Pept. Protein Res.* **25,** 585–93 (1985).

18.   Krishna, N. R., Agresti, D. G., Glickson, J. D. & Walter, R. Solution conformation of peptides by the intramolecular nuclear Overhauser effect experiment. Study of valinomycin-K+. *Biophys. J.* **24,** 791–814 (1978).

19.   Makrlík, E., Dybal, J. & Vaňura, P. A combined extraction and DFT study on the complexation of K+ with valinomycin. *Monatshefte für Chemie - Chem. Mon.* **140,** 1289–1292 (2009).

20.   Haynes, D. H., Kowalsky, A. & Pressman, B. C. Application of Nuclear Magnetic Resonance to the Conformational Changes in Valinomycin during Complexation. *J. Biol. Chem.* **244,** 502–505 (1969).

21.   Inoue, Y., Hakushi, T., Tong, L.-H., Zhao, G.-D. & Tians, B.-Z. Complexation Thermodynamics of Bls(crown ether)s. 2.' Calorimetric Titration of Complexation of Potassium Ion with Bis(benzocrown ether)s: Enthalpy-Entropy Compensation. *J. Phys. Chem* **92,** 2371–2374 (1988).

22.   Tóth, K. *et al.* Novel Bis-Crown-Ether Derivatives For Potassium Sensors. *Anal. Lett.* **22,** 1185–1207 (1989).

23.   Liu, Y. *et al.* Complexation thermodynamics of bis(crown ether)s. 4. Calorimetric titration of intramolecular sandwich complexation of thallium and sodium ions with bis(15-crown-5)s and bis(12-crown-4)s: enthalpy-entropy compensation. *J. Phys. Chem.* **94,** 2666–2670 (1990).

24.   Kelly ', T. R. & Kim, M. H. Relative Binding Affinity of Carboxylate and Its Isosteres: Nitro, Phosphate, Phosphonate, Sulfonate, and &Lactone. *J. Am. Chem. SOC* **116,** 7072–7080 (1994).

25.   Etter, M. C. Encoding and decoding hydrogen-bond patterns of organic compounds. *Acc. Chem. Res.* **23,** 120–126 (1990).

26.   Al-Jallal, N. A., Al-Kahtani, A. A. & El-Azhary, A. A. Conformational Study of the Structure of Free 18-Crown-6. *J. Phys. Chem. A* **109,** 3694–3703 (2005).

27.   Seiler, P., Dobler, M. & Dunitz, J. D. Potassium thiocyanate complex of 1,4,7,10,13,16-hexaoxacyclooctadecane. *Acta Crystallogr. Sect. B Struct. Crystallogr. Cryst. Chem.* **30,** 2744–2745 (1974).

28.   Al-Kahtani, A. A., Al-Jallal, N. A. & El-Azhary, A. A. Conformational and vibrational analysis of 18-crown-6–alkali metal cation complexes. *Spectrochim. Acta Part A Mol. Biomol. Spectrosc.* **132,** 70–83 (2014).

29.   Jason E. Gestwicki, Helen V. Hsieh, and & Pitner, J. B. Using Receptor Conformational Change To Detect Low Molecular Weight Analytes by Surface Plasmon Resonance. (2001).

Chapter 5

Conclusions and Future Work

As a unique analytical technique, BSI offers several advantages over other analytical techniques in its ability to perform binding assays at physiological conditions, with low sample amounts, label-free and in free-solution. These advantages provide straightforward experiments with a wide variety of binding partners in their native states; the experiments discussed in this thesis alone involved three very different types of interactions: 1) enzyme-inhibitor, 2) dsDNA hybridization, and 3) small molecule-ion recognition. Each of these demonstrates BSI's versatility as a RI detector, and show that additional information can be gleaned from the data. Additionally, they demonstrate a few of the experiments that will aid in refining the FreeSRF model that describes the origin of the BSI signal.

The results discussed in Chapter 2 demonstrated that BSI data can be used in conjunction with other techniques to gain insight into a potential enzyme inhibitor's inhibition mechanism. BSI experiments performed with AChE and inhibitors yielded K_D values that could be compared to IC_{50} values obtained in an assay that uses a high concentration of substrate via the Cheng-Prusoff relationship.[1] If the K_D is equal to the IC_{50}, the inhibitor's affinity to the enzyme-substrate complex is the same as its affinity to the enzyme alone, meaning that it has affinity solely for the peripheral site. This is especially useful when screening for noncompetitive inhibitors of AChE, which have been shown to be most effective for treating Alzheimer's symptoms, as the peripheral site

aids in the aggregation of plaque precursors. The instrument was also able to detect dual-binding inhibitors that have affinity for both the active site and peripheral site, and bind in non-equivalent manners to generate two separate, rise-to-max binding curves. This study highlighted BSI's potential as a useful screening tool for potential inhibitors or ligands of a target enzyme or protein.

Previous BSI experiments examined the differences in affinities between DNA oligonucleotides with complementary sequences and those containing two adjacent mismatched base pairs.[2] The experiments described in Chapter 3 expanded on this study to determine BSI's ability to distinguish between a single mismatch or deletion, and also the location of the SNP in the sequence compared to the complementary DNA duplex. These experiments revealed that the binding strand containing a T deletion formed a more stable duplex than the strand containing an A/G mismatch in the same location, and a centrally-located SNP was more destabilizing than the same SNP in a location closer to the end of the sequence. Results also correlated with melting transition studies.

These results highlight the potential of the instrument to be used in a diagnostic setting, especially as fields of personalized medicine become more common and a better understanding of the role of genetics in human health is obtained. Additionally, insight into the origin of the BSI signal resulted from the simple observation that the complementary duplex had a significantly higher signal compared to the SNP-containing duplexes. Evaluation of the signal origin with nucleic acid experiments such as these will help further develop the FreeSRF model for BSI.

The impressive sensitivity of BSI is demonstrated in the nonaqueous, small-molecule ion-recognition systems described in Chapter 4, including 18-Crown-6,

potassium ionophore I (also known as valinomycin), potassium ionophore II, and potassium ionophore III. Signals more than an order of magnitude smaller than those obtained in the DNA hybridization experiments are obtained, and result in binding curves that yield K_D's that are in excellent agreement with those determined via ITC. The FreeSRF expression attributes the RI change upon binding to changes in the bulk intrinsic properties of the newly-formed product or complex, specifically the radius of gyration and solvent-accessible surface area. These small molecule systems have ΔR_{gyr} less than 0.5 Å, but some of the conformational changes studied, including the "clamshell" ionophore II and valinomycin, mimic those seen in larger proteins but on a smaller scale. Ionophore III produced a unique result, a binding signal that changed direction before saturation; this was attributed to the presence of the dodecyl tail in the center of the carbon linker that alters the overall hydrodynamic radius of the complex, first increasing, then decreasing as the clamshell complex is formed.

These studies allow insight into how FreeSRF is affected with small changes, and how differences between aqueous and nonaqueous systems can continue to be studied with other similar systems. They also provide a starting point to a new training set of nonaqueous, small molecule binding systems in order to model and refine FreeSRF. These studies also highlight BSI's ability to selectively detect a target metal ion, providing a potential application in metal sensing for environmental concerns. Taken together, the experiments discussed in these chapters highlight BSI's versatility and sensitivity with a variety of binding partners, and the additional information that BSI binding data can provide.

5.1. Determining Stoichiometry from BSI binding experiments

Data from typical BSI experiments are used to plot a binding curve in order to determine binding affinity via k_D values. Plots are generated as a function of phase shift in radians versus concentration of analyte, and fitted to a rise-to-max one-site binding hyperbola:

$$y = \frac{B_{max} * x}{k_D + x}$$

(1)

In this one-site binding hyperbola equation, y is the phase shift of the signal in radians, x is the concentration of analyte, B_{max} is the maximum binding capacity, and k_D is the dissociation constant. This method has been used to determine binding affinities for a variety of systems, from hydrogen-bonded compounds to proteins and ligands. By instead plotting phase shift versus molar ratio of analyte and fitting the curve to a similar equation, it is possible to obtain an approximation of the stoichiometry of the interaction.[3,4]

$$y = \frac{B_{max} * x}{k + x}$$

(2)

In this equation, x is now the molar ratio of the analyte, and the stoichiometry of the solution is the point at which the sloped portion of this curve intersects the tangent of the saturated portion. To determine the stoichiometry using this method, the equation of the tangent can be obtained by the following equation:[5]

$$(y - Y) = \frac{dy}{dx}(X) * (x - X)$$ (3)

The slope of the tangent at point (X,Y) is *dy/dx*, which is shown below:

$$\frac{dy}{dx} = \frac{B_{max} * k}{(k + x)^2}$$

(4)

The slope of the initial, steep portion of the binding curve is determined by linear regression, and extended to determine the intersection with the tangent. The value of the *x*-axis where this intersection occurs is the approximated stoichiometry of the binding interaction. This method is most straightforward with 1:1 stoichiometry, but also works for higher stoichiometry as long as the signal changes are equivalent. Below are several examples of previous BSI experiments and the stoichiometry determined using the described method.

5.1.2. Stoichiometries of BSI binding systems
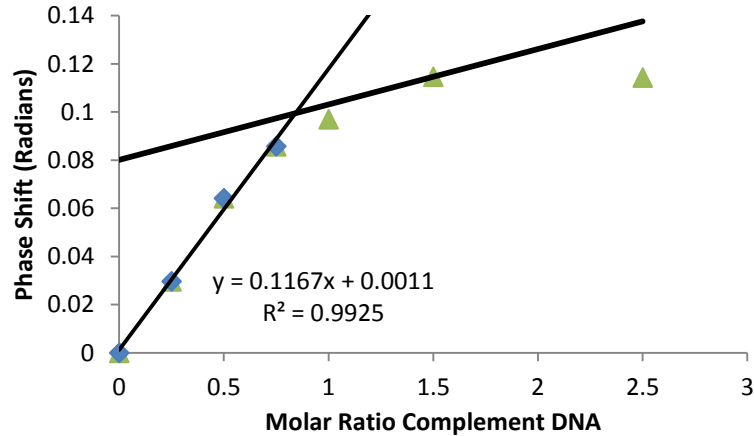
Figure 5.1. Phase shift vs. Molar Ratio of Complement DNA strand plot of dsDNA binding data with initial linear portion and tangent at *x* = 1.5, which results in an intersection at *x* = 0.85.
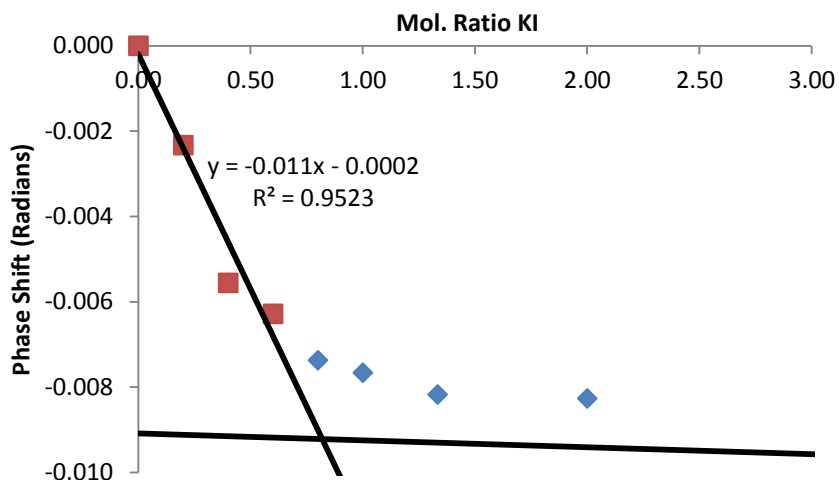
Figure 5.2. Phase shift vs. Molar Ratio of potassium ion to ionophore I binding data with initial linear portion and tangent at $x = 5$, which results in an intersection at $x = 0.82$.
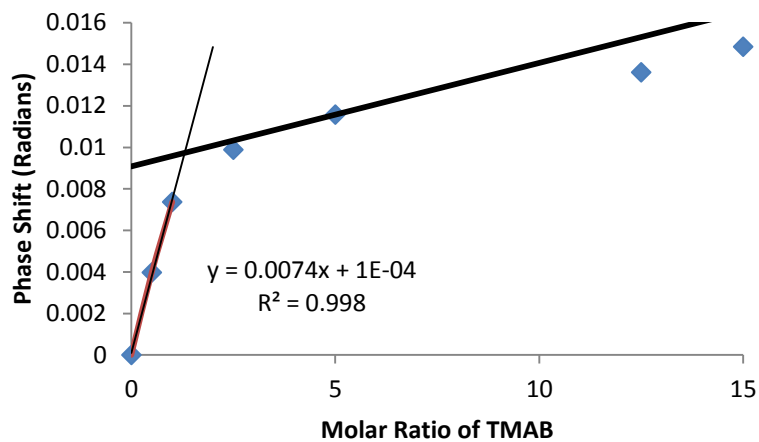
Figure 5.3. Phase shift vs. Molar Ratio of TMAB to DNPU BSI binding data with initial linear portion and tangent at $x = 5$, which results in an intersection at $x = 1.3$.
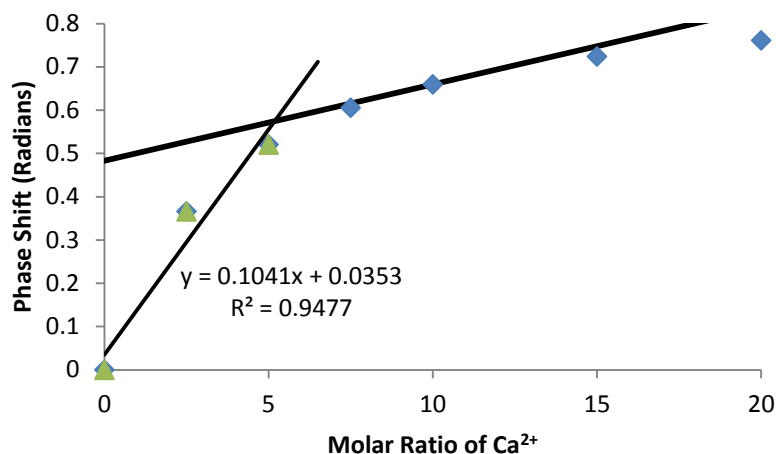
Figure 5.4. Phase shift vs. Molar Ratio of Ca^{2+} to CaM BSI binding data with initial linear portion and tangent at $x = 10$, which results in an intersection at $x = 5.1$.

Figures 5.1-5.4 show the binding curves of four BSI systems: 1) Complementary DNA duplex (Chapter 3), 2) potassium ion with ionophore I (Vm, Chapter 4), 3) TMAB-DNPU hydrogen bonds (Pesciotta)[6], and 4) calcium ion with calmodulin (Bornhop)[7]. The first three systems all showed the expected 1:1 stoichiometry, and the Ca^{2+}-CaM system data resulted in a stoichiometry of about 5:1. The expected stoichiometry is 4:1, but nonspecific binding of calcium would increase the apparent stoichiometry from the data. This method of approximating the stoichiometry of the binding partners does not work for systems with nonequivalent signals from additional binding, such as the dual-binding inhibitors of AChE discussed in Chapter 2, but for many binding systems it provides additional information with no additional experiments.

5.2. Observing decomplexation with BSI

Valinomycin's effectiveness as an ionophore across bacterial membranes lies in its ability to sequester a potassium ion in the center of its ring with the polar ester carbonyls while the outside of its ring remains hydrophobic. The complex is unstable in aqueous media, and Forester and coworkers used computational studies to observe the decomplexation of the potassium complex as it enters an aqueous environment, as shown in Figure 5.5.[8]
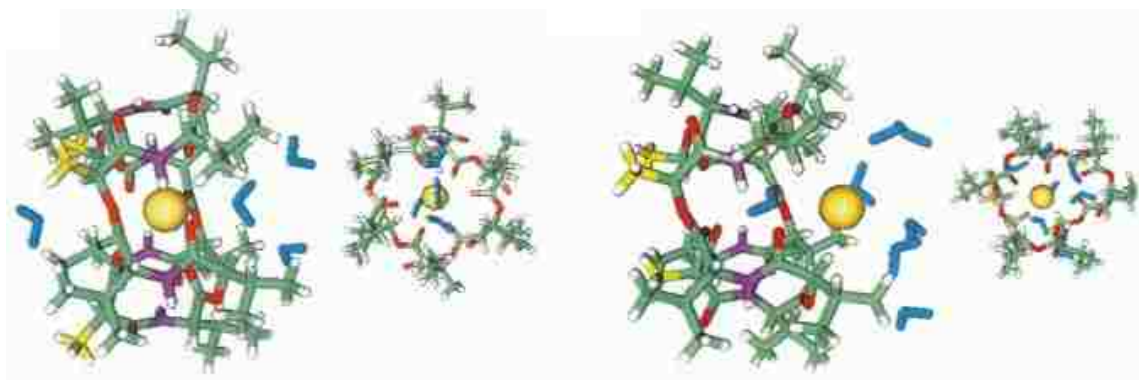
Figure 5.5. Simulation of the decomplexation of the VmK$^+$ complex as increasing amounts of water (shown in blue) are added.[8]

This type of interaction should also generate a significant ΔRI, as addition of water molecules to hydrate the potassium ion induces a conformational changes to the valinomycin molecule. BSI experiments were designed with a constant concentration of VmK$^+$ complex (150 nM) and increasing amounts of water, to observe if any signal changes occur with additional equivalents of water. The BSI data are shown in Figure 5.6.
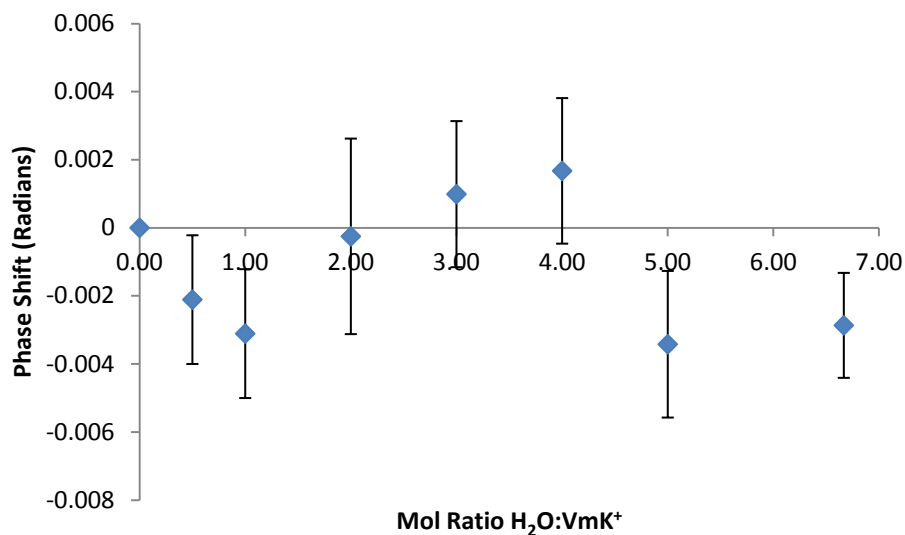
Figure 5.6. Phase Shift vs. Molar Ratio of water to VmK$^+$ BSI data.

The most significant change is seen when going from four to five equivalents of water, but changes in signal direction are observed at as low as one or two equivalents. Experiments could be set up similarly and monitored using techniques such as NMR to correlate these changes with structural changes to continue to improve our understanding of the origin of the BSI signal and the FreeSRF expression. In these ways, experiments beyond the typical binding experiments could be designed to obtain more information on a desired system.

5.3. Future Work with BSI

Future research with BSI could continue in several different directions, owing to its excellent sensitivity and an ever-improving understanding of the instrument. Alterations to the instrument itself could help mitigate noise due to environmental factors, such as air currents, temperature, or pressure changes, including allowing for reference and sample to be measured simultaneously. BSI remains a desirable platform for many biochemical systems due to its small sample sizes and ability to measure native,

unperturbed binding affinities. It can be used as an effective screening tool for potential drug compounds.

Small molecule, metal-ion sensing is a largely unexplored field with BSI that shows great promise, as demonstrated with the potassium ionophores in Chapter 4. Similar metal-ion recognition studies could be designed for metal catalyst studies, environmental studies, or medicinal purposes. Mercury has been shown to insert selectively into T-T DNA base pairs.[9] Experiments with BSI could be designed for Hg-ion detection based on poly-thymine sequences that self-hybridize upon addition of Hg.

Other ionophores could be studied for their potential as medicinal compounds, including potential antibiotic agents. Recently, a report by Arnoux and coworkers introduced a new natural-product based metallophore named staphylopine, shown in Figure 5.7.[10]
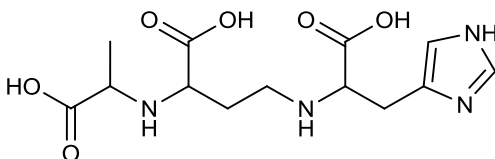
Figure 5.7. Structure of staphylopine

Staphylopine was shown to be similar in structure to nicotianamine, a metal chelator found in plants, which enables them to obtain necessary metals. This compound is found in some bacteria, and was shown to have affinity for a variety of divalent metal cations. Bacteria require metal cations from their host, so this presents a potential target for fighting bacterial infection, either by 1) targeting parts of the biosynthetic cycle that produces staphylopine, or 2) by using analogs to introduce toxic metals into the bacteria cells. Analytical techniques such as BSI could be useful in screening potential

compounds for the former case, and ion-recognition experiments could be designed to evaluate ions' affinities for the latter case.

Small molecule studies with BSI also act as ideal model systems to continue to evaluate the FreeSRF expression. Solvent effects can be analyzed by performing identical experiments in different solvents, or solvent mixtures. For example, hydrogen bonding studies performed in pure MeCN versus a 9:1 MeCN:water mixture could result in different signal magnitudes that yield insight into solvation effects on RI changes. Similarly, protic solvents like methanol would be expected to have an impact on the complexation of 18C6 with potassium, both in terms of binding affinity (ITC experiments showed a slightly larger K_D of ca. 20 μM compared to ca. 3 μM in MeCN), and signal magnitude, due to the possibility of hydrogen bonds to solvent.[11] Solvent choice is limited by its RI; there must be a large enough difference in the RI of the chip and the solvent in order for a high-contrast fringe pattern to be generated, and some solvents, including methanol, adsorb to borosilicate glass. These factors can be avoided with chips made out of different materials, or by surface modification. Another advantage of using small molecule systems to evaluate the FreeSRF expression is the relative ease of computer modeling these systems compared to large, biochemical systems including proteins or nucleic acids.

5.4. Concluding Remarks

The versatility and sensitivity of BSI make it a powerful analytical technique for a wide variety of chemical interactions. The studies discussed in this thesis covered three very different types of interactions, including enzyme-inhibitor, DNA hybridization, and

small-molecule ion-recognition. It has the potential to serve as a screening tool for potential drugs, a diagnostic tool for detecting biomarkers such as SNPs, and a selective ion sensor. Using these studies and future experiments to expand on, and continually refine, the FreeSRF expression will help researchers develop a more thorough understanding of BSI data, and RI detection as a whole. With potential detection limits of less than 100,000 molecules for biochemical systems in free-solution and label free, BSI helps decrease sample amounts and preparation time. These factors, plus its straightforward experimental procedure, make it an ideal candidate for application to many laboratory environments, and we hope that this research assists in making BSI or other universal RI detectors more widely available for chemists.

5.5. References

1.   Cheng, Y. & Prusoff, W. H. Relationship between the inhibition constant (KI) and the concentration of inhibitor which causes 50 per cent inhibition (I50) of an enzymatic reaction. *Biochem. Pharmacol.* **22,** 3099–3108 (1973).

2.   Pesciotta, E. N., Bornhop, D. J. & Flowers, R. A. Back-Scattering Interferometry: A Versatile Platform for the Study of Free-Solution versus Surface-Immobilized Hybridization. *Chem. - An Asian J.* **6,** 70–73 (2011).

3.   Didier, P. *et al.* in 156–199 (2011). doi:10.1039/9781849732666-00156

4.   Favicchio, R., Dragan, A. I., Kneale, G. G. & Read, C. M. Fluorescence spectroscopy and anisotropy in the analysis of DNA-protein interactions. *Methods Mol. Biol.* **543,** 589–611 (2009).

5.   Edwards, J. *An Elementary Treatise on the Differential Calculus with Applications and Numerous Examples*. (Macmillan, 1896).

6.   Pesciotta, E. N., Bornhop, D. J. & Flowers, R. A. Backscattering interferometry: an alternative approach for the study of hydrogen bonding interactions in organic solvents. *Org Lett* **13,** 2654–2657 (2011).

7.   Bornhop, D. J. *et al.* Free-solution, label-free molecular interactions studied by back-scattering interferometry. *Science* **317,** 1732–6 (2007).

8.   Forester, T. R., Smith, W. & Clarke, J. H. Molecular dynamics simulations of valinomycin and its potassium complex in homogeneous solvents. *Biophys. J.* **71,** 544–53 (1996).

9.   Ono, A. & Togashi, H. Highly Selective Oligonucleotide-Based Sensor for Mercury(II) in Aqueous Solutions. *Angew. Chemie Int. Ed.* **43,** 4300–4302 (2004).

10.   Ghssein, G. *et al.* Biosynthesis of a broad-spectrum nicotianamine-like metallophore in Staphylococcus aureus. *Science (80-.).* **352,** 1105–1109 (2016).

11.   Al-Jallal, N. A., Al-Kahtani, A. A. & El-Azhary, A. A. Conformational Study of the Structure of Free 18-Crown-6. *J. Phys. Chem. A* **109,** 3694–3703 (2005).

Gabrielle L. Haddad-Weiser
Curriculum Vitae

Education

Ph.D., Lehigh University, Bethlehem PA August 2016
Dissertation: "Detection and Analysis of Molecular Interactions with Backscattering Interferometry"
Adviser: Dr. Robert A Flowers II

M.S., Lehigh University, Bethlehem PA May 2012
Master of Science, College of Arts and Sciences, Chemistry, May 2012.

B.S., Moravian College, Bethlehem PA May 2010
Bachelor of Science, Chemistry, Magna Cum Laude, May 2010.

Research

Lehigh University Department of Chemistry 2010-2016
Adviser: Dr. Robert A. Flowers II

Used backscattering interferometry (BSI) to measure binding interactions between two species based on changes in refractive index at detection limits comparable to fluorescent techniques, in free solution and label-free. Systems studied include 20-base pair DNA oligonucleotides to detect single nucleotide polymorphisms (SNPs), known and novel inhibitors of acetocholinesterase (AChE), and potassium ion with 18-crown-6 and ionophores in acetonitrile.

Moravian College Department of Chemistry 2009-2010
Adviser: Dr. R. Daniel Libby

Studied reactions of substrates with substituted dihydropyridines as mimics of NADH using NMR and GC-MS.

Teaching Experience

Lehigh University Department of Chemistry

- Studio Instructor for Intro to Chemical Principles, Spring 2015 and Spring 2016

- Laboratory TA for Organic Chemistry I, Fall 2011 and Fall 2015

- Laboratory TA for Intro to Chemical Principles, Spring 2012 and Fall 2014

- Laboratory TA for Equilibrium in Aqueous Systems, Summer 2014 and Fall 2014

- Intro to Chemical Principles, Private Tutor, Fall 2011

Moravian College Department of Chemistry

- Organic Chemistry, Teaching Assistant, Spring 2010

- General Chemistry, Teaching Assistant, Spring 2009

- General Chemistry, Tutor, Fall 2009-Spring 2010

Outreach Experiences- High School Level

STARS Academy Program, interactive chemistry lab for high school students, July 2014

Liberty High School/Girl Scouts of Easter Pennsylvania Outreach Program for STEM fields, interactive chemistry lab, March 2015

Publications

Haddad, G. L.; Young, S. C.; Heindel, N. D.; Flowers, R. A.; Bornhop, D.J.; "Back-Scattering Interferometry: An Ultrasensitive Method for the Rapid and Unperturbed Detection of Acetylcholinesterase." 2012, *51*, 11126-11130.

Haddad-Weiser, G. L.; Flowers, R. A.; Bornhop, D.J.; "Detecting Single Nucleotide Polymorphisms in short DNA duplexes using Backscattering Interferometry" *in preparation.*

Presentations

"Characterization of Intermediates in the reactions of N-pentyldihydropyridine and N-benzyldihydropyridine as model NADH compounds." Haddad, G.; Chando, K.; Libby, R.D. Undergraduate Research Poster Conference, Harrisburg, PA, March 2010.

"Back-Scattering Interferometry: An Ultrasensitive Method for the Rapid and Unperturbed Detection of Acetylcholinesterase." Haddad, G. L.; Young, S. C.; Heindel, N. D.; Flowers, R. A.; Bornhop, D.J. Biophysical Society Pennsylvania Network Meeting Poster Presentation, Bethlehem, PA, September 2012.

"Back-Scattering Interferometry: An Ultrasensitive Method for the Rapid and Unperturbed Detection of Acetylcholinesterase." Haddad, G. L.; Young, S. C.; Heindel, N. D.; Flowers, R. A.; Bornhop, D.J. Oral Presentation, Fall 2012 National Meeting and Exposition of the American Chemical Society, Philadelphia, PA, August 2012.

"Back-Scattering Interferometry: An Ultrasensitive Method for the Rapid and Unperturbed Detection of Acetylcholinesterase." Haddad, G. L.; Young, S. C.; Heindel, N. D.; Flowers, R. A.; Bornhop, D.J. National Organic Chemistry Symposium, Seattle, WA, June 2013.

"Detection of Single Nucleotide Polymorphisms using Backscattering Interferometry." Haddad-Weiser, G. L.; Flowers, R.A.; Bornhop, D.J. Oral Presentation, Spring 2015 National Meeting and Exposition of the American Chemical Society, Denver, CO, March 2015

Experimental and Computer Skills

Laboratory Instruments: Backscattering Interferometry (BSI), Isothermal Titration Calorimetry (ITC), Circular Dichroism (CD), Gas Chomatography-Mass Spectrometry (GC-MS), Infrared Spectroscopy (IR), UV/vis Spectroscopy, Nuclear Magnetic Resonance Spectroscopy (NMR).

Computer Programs: Microsoft Excel/Word/Powerpoint, GraphPad Prism, LoggerPro

Awards and Activities

Lehigh University Dean's Fellowship, Summer 2015
C. Scott Althouse Fellowship, Summer 2013-Spring 2014
Lehigh University Fellowship, Fall 2010-Spring 2011
Graduate Student Senate Department Representative, 2014-2016
Member, American Chemical Society, 2010-2012